Multi-Degree-of-Freedom Micropositioning Using Stepping Principles

Dissertation submitted to the
SWISS FEDERAL INSTITUTE OF TECHNOLOGY
ZURICH

for the degree of
Doctor of Technical Sciences

presented by
Wolfgang Zesch
Dipl. Masch.-Ing. ETH
born November 3, 1968
citizen of Austria

accepted on recommendation of
Prof. Dr. G. Schweitzer, examiner
Prof. Dr. R.Y. Siegwart, co-examiner

Zurich, 1997

Acknowledgments

Table of Contents

6 Conclusions 103

References 109

Appendix 119

Curriculum Vitae 129

Abstract

Micro- and nanotechnology is a key issue in today's and tomorrow's development of advanced products. New tools are – and will be – needed to automatically handle and assemble micro-sized structures with sub-micrometer precision, or to give human beings the capability of operating in these tiny dimensions.

This work focuses on the mechanics of micromanipulation. After some basic considerations, the specifications for a high precision robot structure are defined. Among them, one of the most challenging problems is to position a robot extremely accurately (10 nm) within a large workspace (1 cm^3), i.e., with a spatial dynamics of 10^{-6}. The only way to achieve this accuracy is to use direct measurement of the relation between the target object and the microtool used to treat this object. For the mechanical setup, this strategy reduces the problem of accuracy to a problem of resolution. Special attention has to be paid to friction, more precisely, to the stick-slip phenomenon, as it is the main limiting factor for the positioning resolution.

Stepping actuation principles are able to cover the above dynamic range, since they combine both a high resolution and a theoretically infinite workspace. Driven by piezoelectric actuators, these mechanisms are very simple in design and easy to control. Therefore, they are well suited for micropositioning tasks. Two kinds of stepping principles are investigated: The *crawling principle* and the *inertial principle*. Mathematical models are developed which explain the mechanisms behavior. Experiments are performed to verify these models.

In a second part, we discuss in detail the combination of single actuators to **multi-degree-of-freedom mechanisms**. The aim is to provide high resolution motion within a large 3D working range. To avoid compliant, friction-limited designs, we propose parallel manipulators with flexible joints and links. Two different structures with three degrees of freedom each will be investigated: A planar inertial drive for motions on a horizontal tread and an Inchworm driven spatial structure to attain the complementary three degrees of freedom.

In contrast to macro-robotics, the main restrictions to the kinematic configuration of micromanipulators originate from the sensor, i.e., the microscope used to supervise and control handling and assembly processes. Our approach is a **multi-arm robot** able to operate in the limited space under the microscope.

All these developments were implemented and tested within the **ETHZ-Nanorobot System**. Moreover, benchmark tests proved the feasibility. With simple microassembly tasks performed with teleoperation we demonstrated the ability for micromanipulation and future applications. The accuracy of the closed-loop system is evidenced by high precision motions guided by a feedback controller based on computer vision.

Kurzfassung

In der aktuellen und der zukünftigen Entwicklung von Spitzentechnologie spielt die Nano-Technik eine immer bedeutendere Rolle. Hierfür werden geeignete Werkzeuge benötigt, sei es zum Hantieren und Zusammenbauen von mikroskopischen Baugruppen oder, um dem Bediener einen Einblick in die Nanowelt zu geben und ihn zu befähigen, in diesen Grössenordnungen Operationen durchzuführen.

Diese Arbeit beschäftigt sich mit der Mechanik der Mikromanipulation. Nach einigen grundlegenden Erläuterungen werden die Kriterien für die Entwicklung von hochgenauen Mechanismen behandelt. Zentrale Bedeutung kommt dabei dem Problem der Dynamik zu. Konkret soll der Roboter in einem Arbeitsraum von 1 cm^3 Manipulationen mit einer Genauigkeit von 10 nm ausführen, was einer räumlichen Dynamik von 10^{-6} entspricht. Die einzige Möglichkeit, eine solche Präzision zu erreichen, ist, die Beziehung zwischen Werkstück und Werkzeug direkt zu messen. Diese Strategie führt das Problem einer extremen Positioniergenauigkeit über in die einfachere Frage einer hohen Auflösung. Spezielles Augenmerk ist hierbei auf die Reibung, genauer gesagt, auf den Losreisseffekt, zu legen, da dieser zu einem grossen Teil die Positionierauflösung eines Antriebes bestimmt.

Eine elegante Methode, die oben genannte Dynamik zu erreichen, ist das sogenannte **Schrittprinzip**. Werden piezoelektrische Aktoren verwendet, so bestechen solche Schrittmotoren durch ihre Einfachheit, sowohl im Aufbau als auch in

der Ansteuerung. Dies ist auch der Grund, warum sie für Aufgaben in der Mikro-
positionierung so geeignet erscheinen. In einem ersten Teil der Arbeit werden
zwei derartige Prinzipien untersucht: Der *Kriech-* und der *Trägheitsantrieb.*
Zuerst werden mathematische Modelle, die auf starren Körpern und elastischen
Aktoren beruhen, hergeleitet und danach im Experiment auf ihre Tauglichkeit hin
überprüft.

Ein zweiter Teil behandelt die Kombination von Einzelaktoren zu **Mechanismen
mit mehreren Freiheitsgraden**. Das Ziel ist dabei, die hervorragenden Eigen-
schaften der Schrittantriebe in präzise räumliche Bewegungen umzusetzen. Um
die Limitierungen herkömmlicher Roboter aufgrund von Reibung, Spiel und Ela-
stizität zu umgehen, werden parallele Strukturen mit flexiblen Gelenken und
Armen verwendet. Dieser Ansatz wird anhand zweier Mechanismen mit jeweils
drei Freiheitsgraden demonstriert: Ein ebener Trägheitsantrieb und eine komple-
mentäre räumliche Struktur, die mit Inchworms angetrieben wird.

Im Gegensatz zur Makrowelt spielt bei Mikromanipulationen die Geometrie des
Sensors, d.h. des Mikroskops, das zur Prozessüberwachung benötigt wird, eine
zentrale Rolle. Wegen der beschränkten Platzverhältnisse unter dem Objektiv
wurde in dieser Arbeit darum die Struktur eines **mehrarmigen Roboters**
gewählt.

Zusammen mit den Resultaten anderer Gruppen führten die untersuchten
Ansätze und Lösungen schliesslich zum Bau des **ETHZ-Nanoroboters**. Als
Testaufgaben für die Telemanipulation dienten einfache Handling- und Fügeope-
rationen. Desweiteren wird die Genauigkeit des Gesamtsystems mit Hilfe von
bildgeregelten Präzisionsbewegungen aufgezeigt. Es werden dabei Werte
erreicht, welche die physikalische Auflösungsgrenze des benutzten Mikroskops
um mehr als eine Grössenordnung übertrifft.

1 *Introduction*

Miniaturization is an ongoing development in the last decades' engineering activities. It has the advantage of reducing both the consumption of resources and energy. Additionally, reduced component dimensions allow for integration of an increasing number of functionalities in a given volume or weight. Excellent examples are modern cameras containing a high level of "intelligence" and mechanical features that help the user to take high quality pictures. Miniaturization has also opened completely new fields of application, e.g. within today's tele-communication industry or the area of cell-biology.

1.1 Fabrication of Microparts

Originating from microelectronics, silicon technology[1] has had a great impact on miniaturization of mechanical structures. It renders possible to combine mechanical and electronic functions on the same part and is therefore ideally qualified for micro-electromechanical systems (MEMS) [KOTA94]. The fabrication in a batch process provides stable parameters and low production costs, which makes them appropriate for mass production. This fact has already led to a wide acceptance of MEMS in automobile and consumer equipment industry.

---

1. Currently in the VLSI (Very Large Scale Integration) technology 0.35 µm structure width is state of the art.

In recent years, further micro-machining technologies such as LIGA (Lithographie-Galvanik-Abformung) technology [BRUECK94] or FAB (Fast Atom Beam) etching [HATAKEYA95] have emerged with the major directive of miniaturization and, at the same time, overcoming the restriction to only a limited palette of materials. Nevertheless, classical cutting technology is not at its end. Using ultra precision cutting technique 10 µm-diameter micro-shafts or screws could be manufactured effectively [YAMAGATA95].

All the above technologies obtain individual parts by machining a bulk substrate, i.e., by using a *top-down-methodology*. A different strategy, is to operate in the atomic scale, employing a *bottom-up approach*. Using *ensemble* processes as in synthetic chemistry, future nano structures could selectively be built up out of single atoms and molecules [DREXLER92], similar to cells and macromolecules in biology.

In this work, we will strictly pursue the engineering, i.e., the top-down, approach.

1.2 Assembly Processes

Microparts obtained with the previously mentioned technologies are highly restricted in shape and material. Building real 3D components as well as combining different materials and technologies requires a *microassembly* phase. A robot is needed to perform 3D pick-and-place operations and to apply spatial forces during the attachment process. Furthermore, compounds, as with single microparts, have to be packaged, i.e., mounted on carriers, connected both electrically and mechanically and protected with housings, in order to provide an appropriate interaction with the environment. These operations require both long distant transport phases of the order of several object diameters and ultra precise local manipulations.

The basic grasping and transport problems are already solved in the "human sized" world, while there is still a lack of tools for handling and assembly of microparts. Due to the drastically reduced particle size, different effects play a dominant role in the microworld. Most importantly, problems arising with adhesion forces during grasping and releasing have to be solved in order to render microassembly possible [FEARING95B].

In contrast to our macroscopic environment, the micro- and nano-scale is not directly accessible to the human operator. To supply the user with information

from the microworld *monitoring devices* such as light microscopes (LM) or scanning electron microscopes (SEM) must be used. Additional sensors are also beneficial to deliver local information such as contact forces or other process data. Starting with the development of the Scanning Tunneling Microscope (STM) by Binnig and Rohrer [BINNIG82], various different probe microscopes have opened completely new insights at the nanometer level, and in special cases, even enabled the visualization and manipulation of single atoms [CROMMIE93]. Using these scanning tips as sensors in a robot system could help to explore the nanoworld [GARDNER91].

Future micro-assembled compounds such as quantum devices or biological-chemical structures have the potential for completely new applications in the field of engineering, micro biology, medicine and many other disciplines dealing with microscopic structures.

1.3 Problem Statement

In this section we elaborate the principal problems arising with micromanipulation based on general considerations, but also on the drawbacks of existing systems. An overview on these systems and the corresponding problems is given in section 2.

Definitions

To establish a background of notation and nomenclature, the following "precision" related terms commonly used in robotics [CRAIG89] and precision engineering [SMITH92] are outlined briefly.

- **Resolution** is the smallest change in the parameter of interest, i.e., the position and orientation, that can be affected by a control signal.
- **Repeatability** is a measure of the scatter of accessed positions if an attempt is made to repeat a given operation exactly. For quantification we use the standard deviation σ_x of the goal positions. The repeatability may approach, but can never be better than, the resolution.
- **Accuracy** is the deviation of the real, actually attained position from the desired, calculated position.
- **Neighborhood accuracy** is the accuracy of relative motions within a limited neighborhood Δx.

- **Spatial Dynamics** is the ratio between working range and resolution. Often, if it is clear from the context, the short form 'dynamics' is used.

Positioning Systems

The goal of each positioning system is to place the manipulator's tool center point (TCP) as accurate as possible at a desired position and orientation – both together termed pose. Such a mechanism has to connect multiple actuators to a structure with multiple degrees of freedom (DOF). The mechanism must cover the demanded working range with an accuracy and resolution sufficient for the desired task. In table 1.1 these constraints and the resulting spatial dynamics are outlined for some biological and technical manipulators.

positioning system	number of task DOFs	work. range	resolution	spatial dynamics	
		mm	μm	-	dB
human arm	6	500	500	10^3	60
classical robot	4-6	1000	100	10^4	80
wire bonder	2+1	50	1	$5 \cdot 10^4$	94
NC-tool machine	3-(5)	500	5	10^5	100
STM / AFM	3	0.1	10^{-4}	10^6	60 (120)
micropositioning	5-6	10	10^{-2}	10^6	120

Tab. 1.1: *Comparison of positioning systems*

A technical applications with a large dynamic range is high quality NC machining. Temperature control, high stiffness design, hydrostatic bearings, etc. are needed to provide a high precision [SLOCUM92][MIKROTURN95]. In general these instruments are very large in size and highly complicated in design and support. Conversely, in the atomic domain, piezo-driven probe microscopes perform Angstrøm-displacements in a working range of about 100 μm. Nevertheless, while scanning an object's surface an image resolution slightly above 10^3 (1024 x 1024 pixel). Many technical applications such as wire bonding machines ensure high

accuracy in a few directions only, which is not sufficient for general purpose micromanipulation.

Apparently, the dynamics required for micropositioning is some orders of magnitude higher compared to most conventional applications. An overview on the state of the art in micromanipulation and micropositioning is given in section 2.

Micropositioning

To control a manipulator, its pose has to be measured. Conventional robots or machines normally use sensors located at the joint level. Assuming highly rigid links, we can derive a geometric model to transform the sensor information into the TCP's pose, expressed in a fixed (world) coordinate system 0 (fig. 1.1, a). Expensive designs and extremely small fabricational tolerances have to be used to obtain precise mechanism which correspond to the model. Nevertheless, this technique is insufficient for accurate positioning in the sub-micrometer range.
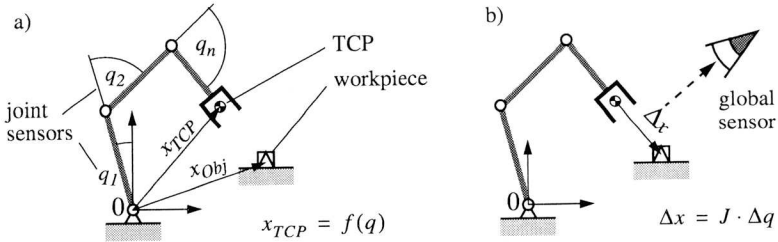
Fig. 1.1: *Strategies to measure the manipulator-workpiece relation: (a) Joint angle measurement: The TCP position x_{TCP} is calculated using the joint angles – or vice versa – with the robot's **absolute** kinematics. (b) Direct (global) measurement: **Relative** displacements are calculated by utilizing the system's Jacobian J.*

Various errors contribute to the absolute positional error. They can be divided into two categories: systematic errors due to a inaccurate model parameters and errors due to unmodeled or chaotic effects. An overview of typical error sources and possible remedies to their minimization is given in table 1.2. A calibration process is often proposed to compensate for systematic errors. However, when working in the microscopic scale, it is difficult to derive a sufficiently precise model and find the corresponding set of parameters [GHAZVINI96]. More impor-

tantly, random errors, which cannot be eliminated by calibration, must no longer be neglected at the microscopic scale. They can only be reduced by *directly measuring* x_{TCP} in relation to x_{Obj}, i.e., the relative pose Δx between the TCP and the workpiece with a global sensor. A joint step Δq is then calculated utilizing the robot's Jacobian J (fig. 1.1, b). This can either be done in a *tele-operative* mode by a human operator, who observes the scenery via a man-machine interface, or *automatically* by a feedback control system.

	phenomenon	influencing parameters	improvements by
systematic	fabric. tolerances, misalignments	mechanical tolerances	calibration, model identification
	sensor errors, miscalibration	linearity, offset, quantization	calibration, filtering
	electronic's and driver resolution	D/A converter resolution	higher resolution
unmodeled and random	mech. deform. due to unknown forces	stiffness, maximum load force	stiff design, elastic robot model
	thermal drift	temperature, thermal expansion coefficient	material selection, temperature control
	friction	materials, lubrication, velocity	avoiding static friction, compensation
	mechanical play	bearing tolerances	preloaded bearings, monolithic structures
	vibration, noise	resonance frequency,	stiff structure, eliminat. of noise sources

Tab. 1.2: *Systematic and random errors, without claim of completeness.*

Although control based on a global sensor still leads to an insufficient accuracy for large displacements – as with the indirect measurement (fig. 1.1, a) – the neighborhood accuracy is improved significantly. Consequently, this setup allows

for performing precise local motions, which is crucial for handling and assembly operations in the microworld.

To conclude, the combination of both a micromanipulator and a global sensor, i.e., a microscope to observe the scenery, is the key to *micromanipulation*. With the direct sensing approach, the system's overall accuracy is determined by the accuracy of the global sensor only. Thus, for the mechanism it is no longer necessary to deal with high accuracy. The only performance required from the manipulator consists in a 3D-resolution adequate for the specific manipulation task.

1.4 Objectives

Based on the aforementioned direct sensing approach, simple and powerful manipulators have to be developed. These mechanisms must possess a high 3D-resolution and should be cheap, relatively small and easy to deal with. Additionally, they have to satisfy the particular constraints given by the sensor system, i.e., the microscope.

It is the aim of this thesis to explore the following issues connected to micropositioning and micromanipulation

- *Actuation*
  Principles of actuation able to cover the large spatial dynamics required for micropositioning have to be developed. Actually, we will employ *stepping principles*, i.e., crawling and inertial motion, since they avoid the drawbacks of conventional actuation (cf. section 2.1) and bearings (cf. section 2.2) for micropositioning. A model of the crawling drive and a generalization of Büchi's impact drive model [BUECHI96] will show the principal relations. Basic positioners relying on stepping principles will be designed. They are intended to serve as experimental platforms to verify our models, but also to work in a prototype microhandling system.

- *3D-Mechanisms*
  To render accurate positioning of micro-sized objects in space possible, single actuators have to be connected to a multi-DOF mechanism using adequate *kinematic structures, bearings and joints*. Two designs, both with three principal DOF, will be presented. Firstly, a planar micropositioning table relying on the inertial principle is developed. The other one is a spatial flexi-

ble platform. Both together will be able to position themselves in 6 DOFs relatively to each other.

- *Manipulator System*
  The above mechanisms are then integrated into the ETHZ-nanorobot system (cf. section 2.4). We will derive design rules for micromanipulators and apply them to our prototype. As discussed above, the direct sensing approach is chosen, to circumvent the accuracy problems arising with existing micromanipulation system (cf. section 2.3).

The relation of the aforementioned topics to other aspects of micromanipulation is shown in fig. 1.2.
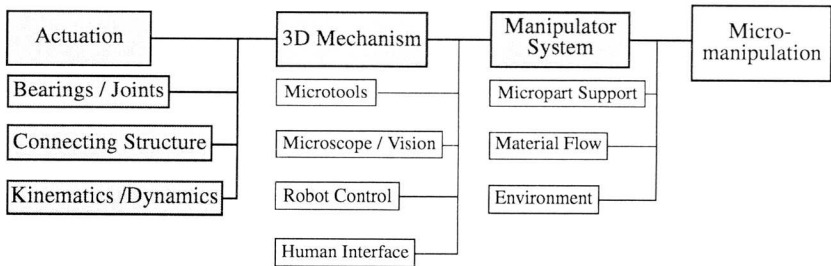
Fig. 1.2: *Micro manipulation's hierarchy. Each of the shaded levels corresponds to one problem to be solved in this thesis.*

The present work is closely related to that of Büchi [BUECHI96]. Büchi has investigated the control of the rough-fine motion concept relying on stepping actuation, whereas this discourse mainly focuses on the mechanical design and layout of the robot.

1.5 Outline of the Thesis

Before the three main topics, i.e. actuation, multi-DOF micropositioning mechanisms, and system integration, are elaborated in chapters 3 to 5, section 2 presents a *review* of existing motion principles and micropositioning devices as well as a discussion of their applicability to micromanipulation.

In section 3, basic principles of *stepping motion* for high resolution positioning, i.e., crawling and inertial motion, are investigated. They are studied in order to deduce rules for an optimum performance in a whole system. Special emphasize is given to the dynamic behavior, but also a model for the load capacity of such mechanisms is derived.

Chapter 4 starts with an introduction to micro-kinematics before possible solutions for *multi-DOF mechanisms* are treated. Two different mechanisms are then discussed. A comparison based on analytical models, computer simulations and practical experiments is included.

After having elaborated basic mechanisms we present their *integration* into a micromanipulation system in section 5. The robot's mechanical structure and the setup of the microscope are discussed in order to understand the constraints on the mechanisms. At the end of this chapter benchmark tests under the light microscope are shown.

A summary, as well as suggestions for further topics of research in the field of micro- and nanorobotics, are presented in section 6.

In the appendix, we present detailed models of friction and piezoelectric actuation. Additionally, a finite element simulation of a planar inertial mechanism demonstrates the agreement of our analytical models with simulation and experiment.

2 *Related Work*

Research related to micropositioning can be separated into research on basic principles and elements, i.e., *actuation* and *bearings*, and research on complete *micromanipulation systems.*

2.1 Actuation

An overview on principles and physical effects suitable for microactuation is given in [FUJITA 89]. In order to provide feasible controllability of the manipulator, only electrically driven actuators, which are able to perform precise displacements, are addressed in this chapter. As fig. 2.1 shows, they can basically be divided into two groups: *Field force actuators* utilize (magnetic and electric) fields to exert forces on masses, which results in accelerations and/or deformations. Conversely, solid state actuators achieve a macroscopic *deformation with molecular forces* stimulated by different physical effects. In the following we present typical micropositioning mechanisms using these actuation principles.

Magnetic Field

Auer has developed a six DOF *direct drive* platform able to control the position within a range of 10 mm / 20 mrad with an accuracy of 1 μm and 10 μrad, respectively [AUER95]. Three pairs of electromagnets levitate a rotor plate with
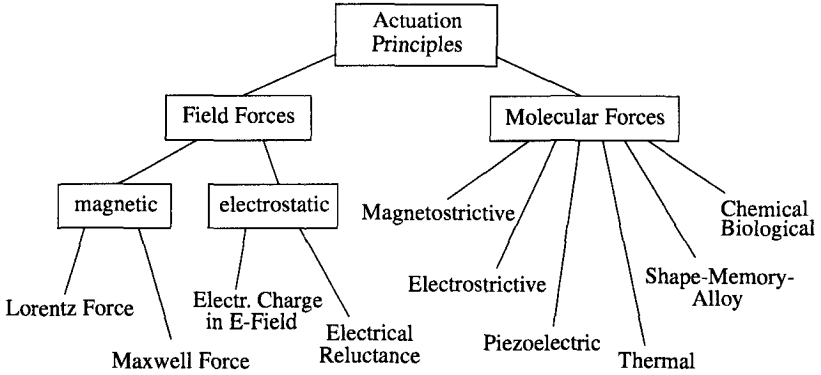
Fig. 2.1: *Actuation principles*

Maxwell (= reluctance) forces, whereas the horizontal propulsion is provided by coils utilizing Lorentz forces. Trumper even increased the resolution of magnetically levitated platforms by inserting it into an oil-filled chamber [TRUMPER94]. Herein, the liquid bath helps both damp the system passively and compensate for gravity. The main drawback of such systems is the need for a very fast controller due to unstable poles and high natural frequencies. This problem becomes even more serious if the actuator has to be miniaturized.

For technical [MIKROTURN95] and laboratory applications [NEWPORT95] *feed screws* driven by electro motors often act as precise 1-DOF positioners. Ball screws are used to minimize the friction and thus to improve the precision. With large mechanical effort Mizumoto has achieved 0.2-nm-resolution by reducing the screw's lead to about 100 µm using a twist-roller frictional drive [MIZUMOTO95]. Such single-DOF positioners are normally arranged in a serial chain to obtain a multi-DOF mechanism. The main drawbacks of these actuator piles are the crosstalk between different DOFs due to the nonideal guideways, the reverse play (back lash), and the systems' large volumes.

Electric Field

Electrostatic actuation is preferably utilized for small mechanisms, such as microactuators produced with silicon machining techniques. Common to all these devices is their low force/torque output. Used together with flexible bearings, they offer only an extremely limited stroke (e.g. cf. [FUKUDA91]). Con-

versely, the main drawback of electrostatic micro-motors is their extremely short lifetime due to unsolved contact problems at the sliding surfaces.

Molecular Force Actuators

Material deformation by molecular forces is widely used for high resolution positioning. *Thermal actuators* [GREITMANN95][YAMAGATA94] as well as *Shape-Memory-Alloys* [SHINJI95] are well accepted because of their simplicity and their compatibility with electromagnetic fields, e.g. for applications inside an electron microscope. Since their response time scales with the structure's volume, these actuators are better suited to microscopic dimensions than to conventional applications. A principal problem is the dissipation of energy which causes undesirable deformations in the environment.

Piezoelectric actuators have been used for micromanipulation for a long time [ELLIS62] and are well accepted for high resolution actuation. They use the distortion of a crystalline grid under influence of an electric field. Fast excitations in the direction of or perpendicular to the electric field are possible, even shear deformations could be activated [BAUER94]. They are inherently stable and easy to control with voltages and hold the position almost without any power consumption. Their major drawbacks, which have prevented their use for conventional applications, are the extremely limited working range[1] and the need for high-voltages.

Enlarging the Workspace

The major handicap of all molecular force (deformation) actuators is their limited range. Efforts to overcome this restriction with mechanical displacement amplification [SCIRE78] result in complicated structures and compliant drive trains.

Another way to achieve longer strokes is a *stepwise movement*, as will be explained in section 3. There are two main principles: Analogously to animals in nature, a mechanism can perform a more or less static *walking* or *crawling* sequence, as with the so called Inchworm motors [BURLEIGH95]. They use three piezo elements – one for transport and two for clamping – to creep with nm-resolution along a theoretically infinitely extended ceramic rod. Compared to electrostatic or electromagnetic drives of the same size, rotational crawling motors [BEXELL95][ASAKAWA92][THORNLEY92], exhibit increased maximum torques at

---

1. E.g. standard piezoelectric materials (PZT) elongate about 0.1% of their length at electrical fields of about 1000-2000 V/mm

lower speeds. It is also possible to design crawlers with more than just one DOF [ZESCH93].

Different from crawling, *inertial drives* rely on the inertia of mass and the nonlinearity of friction (cf. fig. A.1). This dynamic stepping principle is commonly used for rough positioning of STM and AFM tips [BESOCKE86]. Several setups of impact drives [HIGUCHI90] have been investigated in order to improve the velocity [HIGUCHI93], reliability [BUECHI96] and load capacity [AGRAIT91] [RENNER90], and the spatial stability [BAUMANN95]. Applications to drive a robot arm [HIGUCHI92] or to serve as a 3-DOF micropositioner [ZESCH95] have demonstrated their feasibility for high resolution, low force tasks.

Nevertheless, up till now stepping mechanisms are in the laboratory state. Their introduction into a complex manipulation system consisting of several components, especially for spatial motions, has not been addressed yet. Also, to the knowledge of the author, the multi-DOF behavior has not bee studied yet. It is thus one of the main goals of this thesis to develop suitable models for stepping drives and to integrate them into a micromanipulation system with 5-6 DOFs.

Ultrasonic − or travelling wave − motors make use of bending waves passing along elastic structures [FERREIRA96]. These motors utilize the small transversal motion of the structure's cross section to drive a rotor pressed onto the vibrating element. Operation close to the resonant frequency render possible to work with small driving voltages. This advantage is paid off by transient phases at the start and the end of the movements, which are difficult to control precisely.

Conventional positioners - like feed screws or rack and pinion gears - are widely accepted and available for industrial solutions. One could try to overcome their resolution limit with a cascaded arrangement, i.e. a macro/micro manipulator system [SHARON84]. Two actuators are mounted on top of each other in a redundant configuration. One is used for the large movements with a medium resolution whereas the other one operates from a medium range down to the desired final resolution. The control strategy has to deal with the redundancy, but, if carefully implemented, the actuator cascade can be considered as one single motor. Due to the increased number of actuators and sensors and thus the larger dimension, this approach is not adequate for micropositioning tasks.

Discussion of Actuation

Because of the obvious advantages in simplicity and resolution we have selected piezoelectric actuation to drive our nanorobot, as already mentioned in the objec-

tives (cf. section 1.4). It offers an inherently stable open-loop characteristic which reduces the control effort. This issue is very important as the control cycle has a lower limit of some seconds caused by the intensive computation effort needed to extract quantitative position data from the video image (cf. section 2.4). Additionally, piezoelectric actuators are compatible with the operation conditions inside an electron microscope.

To attain a working range large enough for manipulation in the micro- and nanoworld, we have chosen stepping principles. Compared to other strategies they require a smaller dynamic range of the controller and are therefore less troublesome for practical implementations. These aspects will be elaborated in section 3 and section 4.

2.2 Bearings

Practical positioning tasks require motion guidance to achieve the desired kinematic performance. While a platform or a tool has to be moved in the requested (longitudinal) direction in an almost unrestricted manner, all perpendicular (transversal) displacements have to be prohibited as precisely as possible by an appropriate bearing or suspension system. Due to its detrimental influence, static friction must be minimized or avoided completely.

Most mechanical – linear and rotational – guides use lubricated sliding or rolling contacts to serve as a 1-DOF bearing. For clean room or vacuum applications polymer bearings are used because they work properly even without any lubricant. Instead of large static friction, they show a more or less visco-elastic behavior. As an example, Oiwa has investigated a ball center bearing for cylindrical grinding showing a runout better than 10 nm [OIWA93]. Generally, these bearings introduce friction and play into the system, causing backlash. Play can be eliminated by mechanical or magnetical preloading. However, this is paid off by an augmented friction. Furthermore, these systems are rather bulky.

As an alternative to conventional suspension, active levitation principles are completely free of static friction. Air bearings utilize a gas flow to separate moving parts from the stationary ones and serve both for precision applications and to facilitate dislocations of heavy weights. There are two different types used for micropositioning: Normally the bearing is pressurized by an external supply that pumps air through an array of nozzles. The second type, the squeeze film bearing, does not require any air supply: The two surfaces are separated by a gas layer

caused by high frequency oscillations of the stationary plate [PAN67].

Magnetic levitation [SCHWEITZER94] is widely accepted for the suspension of extremely fast rotating spindles and in medicine and high vacuum technology. It is also possible to levitate microparts [BLEULER94]. Embedded in a feedback control system, active suspension principles provide very precise and tunable guidance of moving parts [AUER95].

Nevertheless, this benefit has to be paid off by the need for a high speed controller, which makes it inadequate for micro robotics (cf. section 2.1)

Flexible structures are excellently suited to guide short-stroke mechanisms. Various designs are reported ranging from single rotational hinges [YANG94] to complex structures with up to 4 DOF [RONG94]. As a special case, the *smart structure* directly integrates actuators, and eventually sensors as well, into the suspending elements [HAGOOD88]. The advantage of simplicity and the absence of static friction is paid off by small travel and counteracting elastic forces.

Discussion of Bearings

Conventional bearings can only be used for rough positioning since they introduce undesired friction. Active suspension technologies are not adequate for micromanipulations due to their expensive control. Despite their limited range, we have thus selected flexible structures to build a robot with multiple DOFs. A means to enlarge the working range is presented in section 4.1.2.

2.3 Micromanipulation Systems

In biology and micro-medicine, the handling of µm-sized structures with micrometer screw driven manipulators is widely distributed. For example, manually operated stages with multiple degrees of freedom (DOF) carry glass pipettes to grasp or pierce organic specimens [BROWN92]. Substances can be extracted or injected and characteristic quantities can be measured [SAKMANN95]. The operator is able to achieve sub-micron accuracy by observing her/his actions through a high numerical aperture microscope and by manually controlling the stages.

In an analogous way, manual operation was until now the only reliable method for performing micromechanical assembly tasks. It needs special skill and time, and is mostly restricted to physical experiments in laboratories. For any future industrial application it will be necessary to automate this micromanipulation

tasks. Additionally, it is not possible to achieve sub-micrometer accuracy with manual operation. Dedicated robots equipped with suitable sensors are required to achieve an accuracy sufficient for handling and assembly of microparts. Thus, beginning in the late eighties and early nineties several projects aiming at automated or teleoperated microhandling where launched by different groups.

The Hatamura Laboratory in Japan has developed an ultra precise manipulator to enable a human operator to interact with the microworld [MORISHITA93]. The system's capability was demonstrated by scratching the surface of a VLSI chip in the cavity of a SEM. Hatamura also defined basic rules for micromanipulation which have since become widely used in this field. As a next step, the group built a "*Nano Fabrication World*", consisting of various handling, structuring and observation instruments placed inside a vacuum chamber [HATAKEYA95] [KOYANO95][NAKAO95]. In collaboration with the former group, Sato focused on particle handling [SATO93]. His group investigated a *manipulator with concentrated visual fields*, i.e. with multiple microscopes all observing the same spot from different locations with different observation principles. Using this robot, which works under highly evacuated conditions, the operator is able to pick-and-place particles of the size of a few micrometers by teleoperation [MIYAZAKI95]. The feedback to the operator is provided by the images captured from both a SEM and a LM. The group is also active in force sensing and teleoperation to allow for improved interaction with the nanoworld [SATO94].

The group of Hunter dynamically tests living cells (> 1 kHz) with a "*tele-micro-robot*" achieving nanometer accuracy [HUNTER90]. This manipulator, dedicated for this very task, is driven by six cascaded and independently controlled macro/micro actuators consisting of feed screw drives and piezoelectric elements.
Johannson at the University of Uppsala in Sweden has developed the "*Microman II*", a 4-DOF micromanipulator working in a SEM [JOHANNSON93]. The system is dedicated to the fabrication and assembly of future microrobots with millimeter or even lower dimensions. Due to their special design and tasks, these two systems are unsuited for general micromanipulation.

Inspired by the *ETHZ-Nanorobotics project* (cf. section 2.4), the "Institut de Microtechnique" at the EPFL Lausanne in Switzerland started a *microassembly* project. The robot [BREGUET95] is controlled via a virtual reality interface based on a descriptive model of the microworld [SULZMANN95].

In contrast to all these systems, which try to perform micromanipulation with rather dexterous and complicated manipulators, Fearing proposes a different

approach [FEARING95A]. A planar array of magnetic coils allows him to move *"milli-robots"* to push the target object to the goal position. Moesner even moves one step further. Metallic and non-metallic particles are directly moved with electrostatic fields produced by AC potentials applied to a grid of electrodes [MOESNER95]. Both the *direct and indirect movement of objects by field forces* generated by dedicated actuation arrays, are usually restricted to planar tasks. Further, it is difficult to control the orientation of the objects and the stiffness of the grasp is rather poor.

Discussion of Micromanipulation Systems

Many of the above micromanipulation systems try to overcome the precision related problems of conventional mechanisms with higher manufacturing accuracy and/or with calibration procedures. A considerable number of actuators is needed for large displacements, for fine motion, and for compensation and adjustment. This results in long drive trains which bring forth high sensitivity to temperature changes and low stiffness. The strategy soon reaches its limits, when the size of the manipulators themselves have to be decreased or the fabricational tolerances are no more sufficient. Significant improvements in accuracy and simplicity of the manipulator can be made if the robot and the object positions are directly measured and controlled with sensor feedback. In this case, actuators and mechanisms with a high resolution – but not necessarily a high accuracy – are needed, as stated in section 1.3.

Our concept, specified in cf. section 1.4, is thus to build a general purpose microrobot, which may be inaccurate in the open-loop controlled mode. It has to posses at least six DOFs used for both performing manipulation tasks and sensor guided compensation of errors.

2.4 The ETHZ Nanorobotics Project

The "Nanorobotics Project" at the Swiss Federal Institute of Technology in Zürich ETHZ [CODOUREY95], started in August 1993, aims at the design and implementation of a general purpose robot with the following specifications:
- handling of parts in the size of some micrometers up to several 100 μm
- one or several tools to handle the objects
- accuracy better than 10 nm within a workspace of 1 cm^3 in 5 or 6 DOFs
- suitable for vacuum or cleanroom conditions

- small size, to fit into the cavity of a SEM

In order to achieve these goals, new studies have been launched. According to table 2.1, five topics have been identified as subprojects.

field of research	laboratory of the ETHZ
nanorobot system	Electronic Engineering and Design Laboratory
microtools	Institute of Robotics
mechanical properties of microstructures	Institute of Mechanics
computer vision	Image Science Lab
contact forces	Institute of Solid State Physics

Tab. 2.1: *Research topics and the corresponding laboratories involved in the project. Dark cells indicate the responsibilities discussed in this work.*

Fig. 2.2 shows the setup of the nanorobot system. Its main part is a redundant *3-arm microrobot* operating under a *stereo light microscope* (SLM). The first arm is the object carrier. Its planar DOFs (x, y, φ_z), as well as the tilt motion (φ_x) are driven with the inertial drive principle (cf. section 3.3). Objects lying on top of this manipulator can be positioned along this DOFs with a resolution of better than 10 nm and 1 µrad, respectively. Vertical translations (z) are performed with a micrometer drive. The second arm is equipped with a micro-fabricated tweezer [GREITMANN95], which consists of a thermally actuated bimorph finger and a piezoresistive force sensor finger. The tweezer can be translated along the x- and z-axes and with a further inertial drive rotated in φ_y with a resolution better than 0.1 µrad. The third arm (y, z) carries a vacuum tool based on a glass pipette to pick and place objects [ZESCH97]. All translations of the tool carriers are performed by DC motor-driven micrometer screws with a resolution of 1 µm.

The working space is observed by a stereo light microscope (SLM), in our case a Zeiss Stemi 11, with a maximum numerical aperture of 0.136. The microscope is
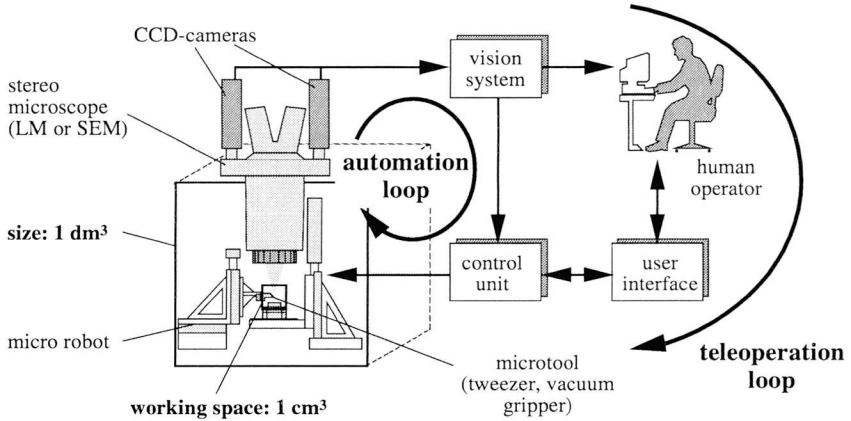
Fig. 2.2: *The ETHZ Nanorobot system.*

equipped with two CCD-cameras for image capturing. The visual information contained in the stereo imagery is used for automated or teleoperated control. In the *automated mode*, a computer vision system, which uses visual tracking algorithms, provides the information necessary to locate tools and target objects [DANUSER96A]. The information from the micro-world is sent to the *control unit*, which moves the robot with an accuracy of about 250 nm [DANUSER96B]. In the teleoperation mode, the human operator directly or indirectly defines the signals for robot control through a dedicated *user interface* [RODRIGUEZ96] while observing the scene. These two levels of control allow the operator to work either teleoperative with more or less direct access to the manipulator or in a semi-autonomous mode [CODOUREY96]. In the latter case only high level commands – such as commitment of goal positions or graphical selection of target objects – are specified and fed to the controller. The control task itself is executed with sensor feedback [PAPPAS96].

During gripping the target object is in mechanical contact with the tool. Adhesion effects [VOEGELI97] restrict the minimum particle size which can be handled reliably to about 50 μm and the resulting placing accuracy to some micrometers. Nevertheless, the positioning accuracy of objects fixed to either a tool or the object carrier, i.e., the closed loop accuracy of the manipulator proposed in this thesis, amounts to about 50 nm.

3 *Stepping Principles for High Precision Motion*

Conventional actuation directly and *continuously* maps the input signal $u(t)$ to the actuator's output $x(t)$ according to

$$x(t) = f(u(t)). \qquad (3.1)$$

With actuation principles such as magnetic or piezo-electric the working range and the resolution in positioning are characterized by the driver's dynamic range. Driving circuitries with a dynamics sufficient for micromanipulation[1] are difficult to design and thus expensive. Nevertheless, these actuation principles are well suited for precise local positioning.

A common way to reduce the demanded dynamics to a smaller local ratio is to divide up the working range into several steps. Such *stepping principles* which are able to perform rough, but long distance motions by utilizing short-stroke actuators will be discussed in this chapter.

3.1 Introduction to Stepping Principles

One way to find solutions to problems in engineering is to look at biological systems: Animals – and humans – approach a goal position with an approximate and

---

1. The ETHZ NanoRobotics project aims at a positional accuracy of 10 nm in a workspace of 1 cm^3, i.e. a dynamic range of 10^{-6} (120 dB).

inaccurate walking or crawling movement (fig. 3.1, left). As soon as the goal lies in the local range they switch to a continuous, but precise control of the extremities (fig. 3.1, right). Using this method, animals are able to position themselves very accurately in a territory much larger than their physical size.
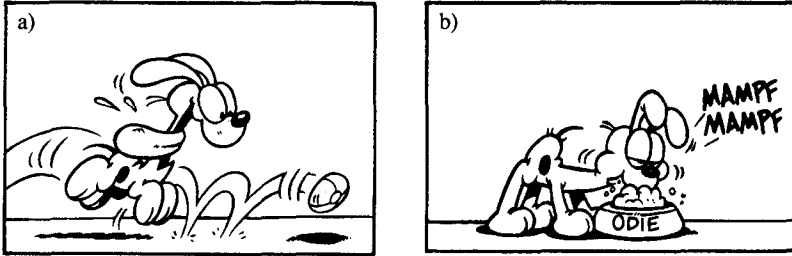

Fig. 3.1: *The animal's two modes of "positioning": Large motions are performed by (a) walking and (b) local movements by continuously controlling the extremities, from Garfield© by Jim Davis.*

Expressed in technical terms, legged creatures posses a reduced actuator stroke to acquire accuracy with *fine motion*. Conversely, they move over large distances by performing one step after the other in a *rough motion* mode. The total displacement can thus be written as

$$x(t) = \sum_i x_i + f(u(t)), \qquad (3.2)$$

i.e., a sum of rough motion steps x_i and a fine displacement $x_{fine}(t) = f(u(t))$. Recall that the rough displacement only depends on the history, but not the current value of the noisy driving signal $u(t)$. From the point of view of control, this two-mode approach reduces the dynamic range by some orders of magnitude[2].

Conventional stepping mechanisms, such as electromagnetic or electrostatic stepper motors move in steps from one equilibrium position to the next, which are given by the motor's design. Hence, the step size Δx is determined by the distance between two equilibrium positions. A grid of equilibria is easy to fabricate in one

---

2. This principle of compressing the signal's dynamic range is already well established for sensors. Optical encoders provide a resolution of up to 100'000 cts per revolution and permit a 1:100 interpolation. Laser interferometers count along a well known wave length scale and provide a fine-resolution down to some nanometers.

or even two DOFs, whereas it becomes very difficult for more than two DOFs. This strategy will not be pursued in this work.

Contrarily, we investigate a different group of stepping principles. Herein, the steps do not rely on geometrically determined equilibrium positions, but rather on a periodic change of kinematic configurations. Let us consider the "stepper" shown in fig. 3.2, (a). It consists of two legs connected by actuators to change the distance l between them. A leg can be moved with respect to the ground, if it is released from the substrate, while the other one is fixed (fig. 3.2, b). Vice versa, in the other kinematic configuration (fig. 3.2, d), leg 1 can be moved, and leg 2 is fixed. For example, walking animals perform this release by lifting the corresponding leg. With an appropriate sequence of releasing, moving in the desired direction, and fixing one leg after the other ($a \rightarrow b \rightarrow c \rightarrow d \rightarrow a$ or vice versa), a net displacement Δx is obtained. Notice that releasing does not necessarily require an uplift of the leg. It is sufficient, if the released leg can be moved freely on the substrate, while the other one rests at its position.
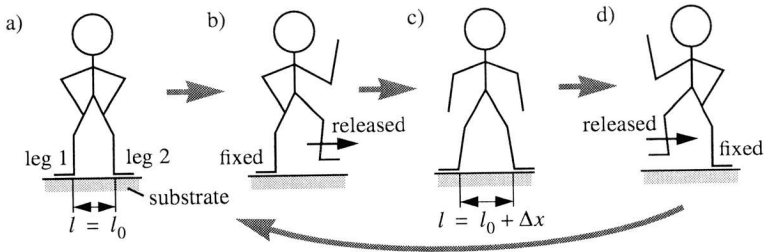

Fig. 3.2: *Phases of stepping motion, (a) initial position, (b) configuration 1 (leg 1 fixed, leg 2 released), (c) intermediate position, Note the changed leg distance!, (d) configuration 2.*

The periodic transition from one configuration to the other, i.e., releasing and fixing of legs, can be performed with different means, also shown in table 3.1:

- Legs can be lifted during the released phase. The result is a *walking* motion. Dynamically raising all legs at the same time generates a *hopping* sequence. Principal drawbacks of these two methods are the need for actuators to lift the legs, as well as vertical oscillations. However, these strategies are well suited for rough terrain and changing ground conditions.
- If all legs stay in contact with the substrate, releasing and fixing can be achieved by controlling the frictional force. *Crawlers* move the released legs

along the surface of the substrate with low friction. At the same time, the frictional force between the fixed legs and the substrate is maximized. This is performed by changing the distribution of weight on the legs or by utilizing clamps. As a significant disadvantage, clamping elements such as electromagnets or mechanical clamps are required. Due to the controllable frictional force, crawling motion is well suited for applications with large load forces. This is why we have selected this principle as a candidate for vertical, weight carrying motions in the nanorobot. It is investigated in section 3.2.

principle of motion	switching principle	application	
		biological	technical
hopping	removal of ground contact	kangaroo	vibrational conveyer
walking	contact removal of single legs	legged animal	walking robot
crawling	control of frictional force	lurch, snake	Inchworm [BURLEIGH95]
inertial drive	nonlinearity of friction	squid	impact drive, stick-slip drive
rolling	continuous leg	motor of salmonella	wheeled vehicles
multiple equilibrium positions	structured substrate	–	stepping motors

Tab. 3.1: *Overview of stepping principles. Those principles investigated in this work are indicated by colored boxes*

- The mechanically simplest principle is the *inertial drive*. It possesses only one actuator and utilizes the nonlinearity of friction (cf. appendix A) and the inertia of mass. Due to uncritical fabricational tolerances, this dynamic means of performing steps is excellently suited for actuation in the microworld. The principle and its implementation will be discussed in section 3.3.

- Rolling is a continuous form of changing the kinematic configuration. As the major drawback, it requires bearings for the roller's axle, which introduce undesirable friction and play. Thus, this method is not investigated in this work.

Due to its physical principle, any stepping motion causes vibrations and is limited in precision. This restriction can be circumvented by adding a *fine motion* mode. As soon as the goal position lies within the working range of the actuator, the control is switched to local positioning. The stepper remains in one of its kinematic configurations, while the actuator is controlled continuously with a high resolution (cf. eq. 3.2). This allows for very precise positioning.

As for all mobile systems, the total deviation between goal and actual position is the sum of the errors of all steps. Thus, if a goal has to be approached accurately, an external sensor is required to update the odometric information. Further, a local feedback loop, able to control the actuator's fine displacement fast and precisely, can improve the system's performance significantly. The issue of combining these two control levels is discussed in [BUECHI96].

We have chosen piezoelectric actuation for our stepping mechanisms. It meets the requirements of both fine and rough motion, i.e., high stiffness, fast response time and inherent stability (cf. section 2.1). The mathematical models of stepping motion as well as the realizations presented in the next chapters are based on these actuators. The fundamentals and a detailed model of piezoelectric actuation can be found in appendix B.

3.2 The Crawling Principle

Crawling is a stepping principle relying on the control of frictional forces between the legs and the substrate. Let us consider a stepper consisting of two clampable legs connected by an actuator situated in-between them, as shown in fig. 3.3. During the forward motion one leg is fixed to the ground (a). After the actuator has reached its end position, the clamping conditions are switched (b). Subsequently, the next half step (c) is performed and leg cleaving is reversed again (d). Such a step sequence results in a net displacement Δx. If performed repeatedly, arbitrary displacements can be achieved. To inverse the direction, the order of the sequence simply has to be reversed.
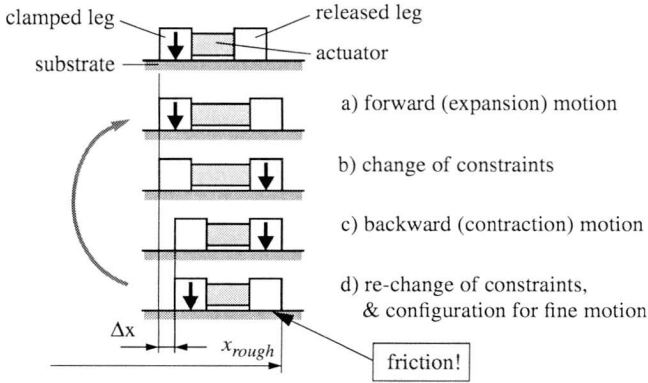
Fig. 3.3: *The crawler's basic stepping sequence*

As a straight forward solution for clamping, the leg could be fixed mechanically with a gripping mechanism. This strategy requires small fabricational tolerances and restricts the motion to a limited geometric manifold, normally to only one DOF. For example, the Inchworm [BURLEIGH95] walks along a very precise ceramic rod using tube piezos to grip the rod. Another method is to generate the normal force magnetically or electrostatically, i.e., by means of field forces. This leads to simple and robust systems.

Fine motion is possible if the leg which has to be positioned accurately is released, whereas the other one is clamped (fig. 3.3, d). Notice that the frictional force acting between the unclamped leg and the substrate has to be minimized in order to achieve a high positioning resolution!

3.2.1 Modeling the Crawler

Fig. 3.4 presents the quasi static model for one half-step (m_1 clamped to the substrate, m_2 released). Herein k_P and k_C denote the actuator's and the released clamp's stiffness, respectively, in x-direction. F_L is an external load force and F_P is the (internal) force acting upon the actuator.

The kinematic constraints can be changed by controlling the normal forces F_{N1} and F_{N2} from F_{Nmin} to F_{Nmax}. According to Coulomb's model of friction (cf. appendix A) the friction between leg and substrate can thus be changed between
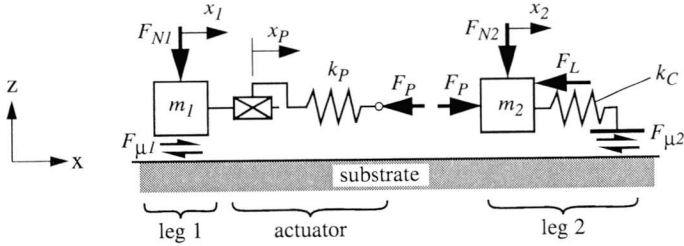
Fig. 3.4: *Elastic model of the crawler loaded with an external load force F_{ext} in the kinematic configuration, where clamp 1 is fixed.*

the released state with its remaining frictional force $F_{\mu,released}$ and the clamped state with a maximum frictional force $F_{\mu,clamped}$.

Step Size

For simplicity, we start the evaluation of the step size Δx in the undeformed state, i.e., the force F_P in the piezo actuator is zero and thus its length is l_0 (fig. 3.5, a).
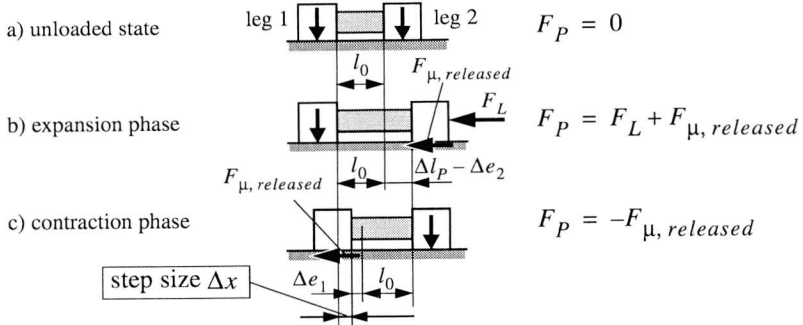

Fig. 3.5: *Displacements of the legs during a stepping sequence.*

During the expansion phase (cf. fig. 3.5, b), i.e., leg 1 is clamped and leg 2 is released, the actuator has to work against the load and the friction which cause an elastic deformation of

$$\Delta e_2 = \frac{F_P\big|_{expansion}}{k_P} = \frac{F_L + F_{\mu,released}}{k_P}. \tag{3.3}$$

Thus, at the end of the expansion phase leg 2 has been shifted by

$$\Delta x_2 = \Delta l_P - \Delta e_2, \tag{3.4}$$

where Δl_P is the piezo displacement given by

$$\Delta l_P = d \cdot \Delta V. \tag{3.5}$$

Conversely, during the contraction phase (cf. fig. 3.5, c) leg 2 is clamped and leg 1 is released. The actuator is subject to tension, which causes an elongation of

$$\Delta e_1 = -\frac{F_P\big|_{\text{contraction}}}{k_P} = \frac{F_{\mu, released}}{k_P}. \tag{3.6}$$

With respect to the undeformed length l_0 this results in a displacement of leg 1 of

$$\Delta x_1 = \Delta l_P - \Delta e_1. \tag{3.7}$$

Finally, the net step of the whole mechanism can be extracted from fig. 3.5. After substituting with eq. 3.3, eq. 3.5, and eq. 3.6, it is given by

$$\Delta x = (l_0 + \Delta l_P - \Delta e_2) - (l_0 + \Delta e_1) = d\Delta V - \frac{F_L + 2F_{\mu, released}}{k_P}, \tag{3.8}$$

i.e, Δx decreases linearly with the load and with the friction at the released clamp.

Stick Condition and Fine Motion

This model is valid, as long as the fixed clamp, does not slip. For the state of fig. 3.4, the dynamic equations for leg 1 (clamped) and leg 2 (released) are

$$F_{\mu 1} = F_P, \tag{3.9}$$

$$m_2 \ddot{x}_2 = F_P - F_L - \text{sgn}(\dot{x}_2) \cdot F_{\mu, released}, \tag{3.10}$$

respectively, with $F_{\mu 1}$ being the frictional force acting on leg1. To prevent slipping of leg 1, $F_{\mu 1}$ must not exceed the maximum frictional force $F_{\mu, clamped}$. With eq. 3.9 and eq. 3.10, this yields the *stick condition*

$$F_L + m_2\ddot{x}_2 + \text{sgn}(\dot{x}_2) \cdot F_{\mu, released} \leq F_{\mu, clamped}. \qquad (3.11)$$

One might argue that the crawler's resolution is limited by stick-slip caused by friction between the released leg 2 and the substrate. Nevertheless, fine positioning is possible thanks to the compliance of clamp 2. If the released clamp sticks at its position due to the friction $F_{\mu, released}$, the displacement of leg 2 becomes

$$x_2 = x_P \cdot \frac{k_P}{k_P + k_C}, \qquad (3.12)$$

i.e., unaffected by the frictional force at the released leg.

To verify our model of crawling motion, we have built the prototype *NanoCrawl*. Its design and performance are discussed in the following section.

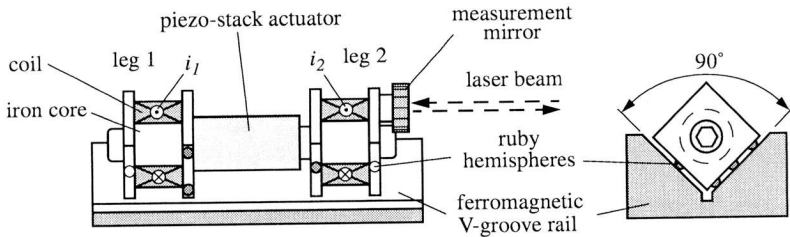### 3.2.2 NanoCrawl – A Micro Crawling Positioner

Experimental setup

Fig. 3.6: *Sketch of the 1-DOF Crawling Mechanism NanoCrawl*

The design of NanoCrawl is outlined in fig. 3.6. The mechanism runs in a polished ferromagnetic V-groove rail and is basically composed of two magnet legs and a piezo stack actuator in-between. Each of the magnets consists of an iron core and a coil wound around its cylindrical section. The two legs can be magnetically clamped to the rail with clamping forces F_{N1} and F_{N2} (cf. fig. 3.4) generated by currents i_1 and i_2 through the coils, respectively.

As shown in fig. 3.7, the mechanism is supported by a configuration of five contact points, formed by ruby hemispheres. They ensure precise linear guidance
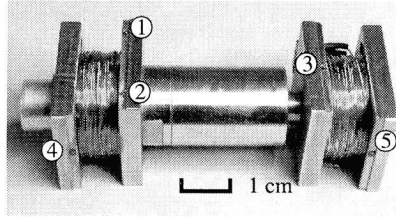
Fig. 3.7: *Bottom view of NanoCrawl. The five ruby hemispheres (1 to 5) act as point contacts to provide a well defined position.*

with low wear. In the actual setup, i.e., ruby on steel, there is no significant difference between the static coefficient μ_0 and kinetic coefficient μ_k of friction (0.122 and 0.120, respectively). The dimensions of NanoCrawl are given in table 3.2.

parameter	leg 1	leg 2
mass	105 g	163
frict. force F_μ: $i = I_{released} = 0$ A $i = I_{clamped} = 0.4$ A	0.35 2.05	0.38 1.93
size piezo voltage V maximum travel Δl_P coefficient of friction $\mu_0 \approx \mu_k \approx \mu$	$79 \times 30 \times 30$ mm^3 0 - 100 V 10.4 µm 0.12	

Tab. 3.2: *Data of NanoCrawl*

A laser interferometer with a resolution of better than 10 nm and a sampling rate of up to 1 kHz served as a position reference. The laser beam was reflected by a mirror attached to leg 2 of NanoCrawl.

Rough Motion

Rough motion aims at approaching a desired goal by means of steps as fast as possible with a remaining error smaller than the actuator's local range Δl_P. Fig. 3.8 shows displacement patterns of m_2 for three different frequencies.
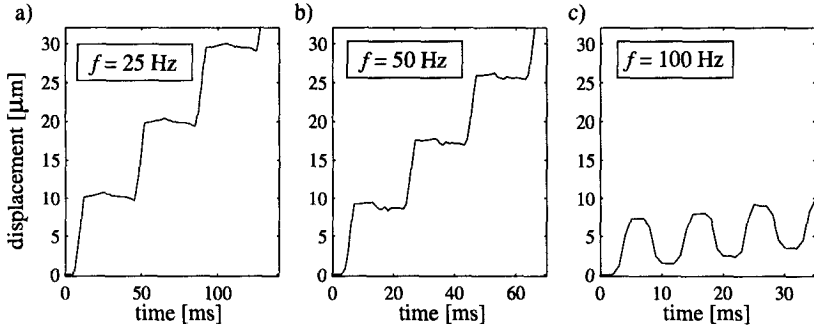
Fig. 3.8: *NanoCrawl's step patterns in the unloaded case ($F_L = 0$) at different frequencies. The voltage stroke ΔV is set to 100 V and the clamping current $I_{clamped} = 0.4$ A.*

Up to 50 Hz (cf. fig. 3.8, a & b) both Δx = 8-9 µm and the displacement pattern agree with our model. A completely different behavior is observed at 100 Hz: The step size Δx decreases to almost zero. This effect arises from the limited current slew rate di/dt caused by the coils' inductance L and the amplifier's finite supply voltage. Thus, the currents i_1 and i_2 reach their steady state values until after a rise/fall time of about 3-4 ms. For 100 Hz (cf. fig. 3.8, c), this leads to conditions where both currents i_1 and i_2 are different from zero during the piezo's elongation/contraction phase. This effect yields undesirable slip phases.

Looking closer at the step patterns, we notice a small, but repeatable backlash during the piezo's recontraction phase at 25 and 50 Hz. It originates from both the drive's compliancy and the aforementioned slip phase. The result is a decreased mean step size $\overline{\Delta x}$ at higher frequencies, as fig. 3.9 confirms. Further, the uncertainty, i.e. the step size's standard deviation σ_x, grows from 1.1% to 2% of $\overline{\Delta x}$. We will show below that this phenomenon becomes even more significant for large loads F_L.

To summarize, we propose to operate NanoCrawl with a frequency and a clamping current of f = 50 Hz and $I_{clamped}$ = 0.4 A, respectively, in order to achieve a maximum velocity of 370 µm/s. Conversely, if the emphasis is put on good repeatability, i.e., a small uncertainty σ_x, the optimal operation conditions are f < 25 Hz and $I_{clamped}$ = 0.4 A,

positive direction **negative direction**

$f = 25$ Hz

$\overline{\Delta x} = 9.83 \mu m$
$\sigma_x = 0.12 \mu m$

$\overline{\Delta x} = -9.70 \mu m$
$\sigma_x = 0.10 \mu m$

step size Δx [μm]

$f = 50$ Hz

$\overline{\Delta x} = 8.44 \mu m$
$\sigma_x = 0.15 \mu m$

$\overline{\Delta x} = -8.44 \mu m$
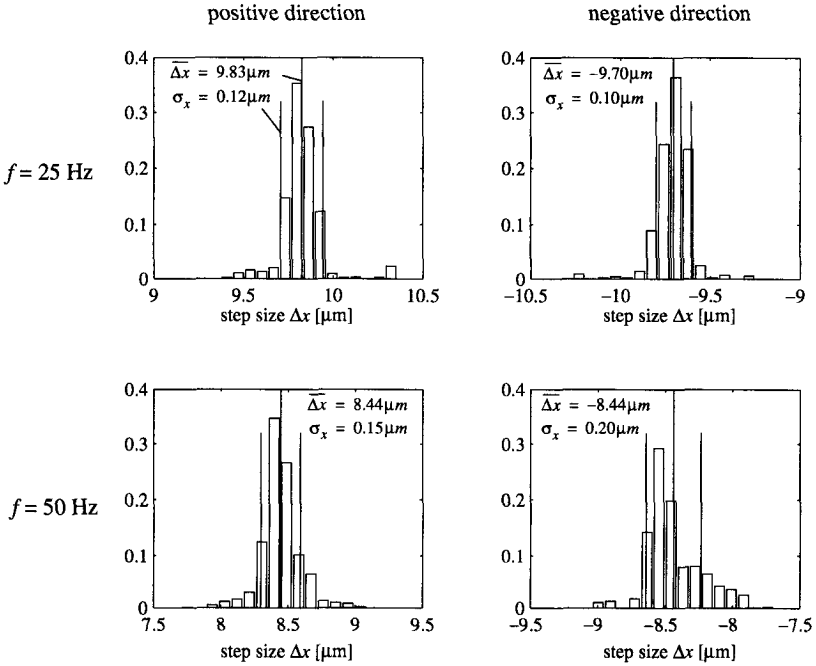$\sigma_x = 0.20 \mu m$

step size Δx [μm]

Fig. 3.9: *Step size distribution at 25 and 50 Hz for positive and negative direction (1000 measurements each)*

Feedback Control

To position NanoStep with nm-accuracy, we implemented a non-linear feedback controller which switches between rough motion and PID-controlled fine positioning [SHIMIZU97]. As fig. 3.10 (a) shows, the mechanism approaches the goal position x_{goal} with its maximum velocity of 0.37 mm/s as long as the error $x_{err} = x_{goal} - x$ satisfies the condition

$$x_{err} < \Delta l_p, \tag{3.13}$$

where Δl_p is the piezo's stroke of 10.4 μm. As soon as the controller changes to fine positioning (fig. 3.10, b), the piezo is guided to the goal by the PID control-
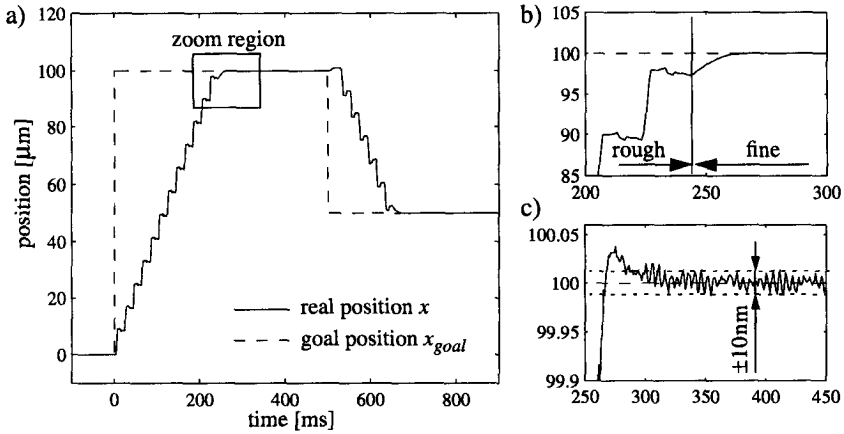
Fig. 3.10: *NanoCrawl's response to steps in the goal position of +100 and -50 μm, respectively, using a PID controller. (a) global view, (b) transition from rough to fine motion, (c) transient phase of fine motion.*

ler. Its parameters were adjusted according to the criterion of Ziegler-Nichols. With this configuration we achieved an accuracy of about 10 nm (fig. 3.10, c)[3].

Load Behavior

A fundamental merit of the crawling principle is the controllable frictional force. It allows us to pull or push loads even larger than the mechanism's weight. NanoCrawl's dependency of the step size on the load F_L is shown in fig. 3.11.

Obviously, Δx decreases dramatically, i.e., the legs begin to slip, when F_L exceeds a certain value. The theoretical limit for very slow motions, i.e., $m \cdot \ddot{x}_2 \ll F_{\mu, clamped}$ can be deduced from eq. 3.11 and is given by

$$|F_L| < F_{\mu, clamped} - F_{\mu, released}. \tag{3.14}$$

Hence, the load capacity can be increased by maximizing the difference between $F_{\mu,clamped}$ and $F_{\mu,released}$, i.e., employing a large current $I_{clamped}$. At 50 Hz these

---

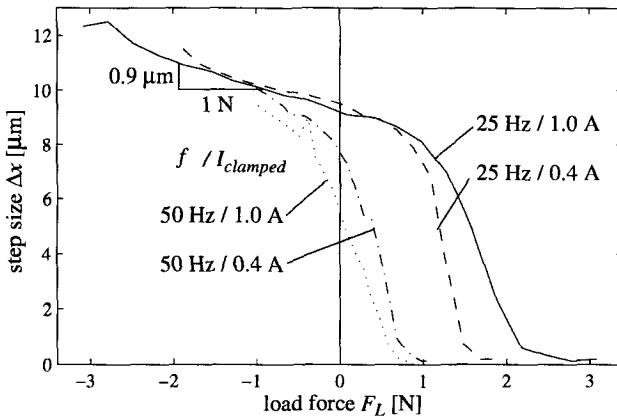3. which is mainly given by the resolution of the interferometer.

Fig. 3.11: *Step size/load characteristic of NanoCrawl at different frequencies f and clamping currents $I_{clamped}$.*

currents do not reach their steady state value and thus undesirable slip occurs. It is therefore also necessary to run NanoCrawl at lower frequencies, e.g. 25 Hz.

In the stable regime Δx decreases approximately linear with F_L, which qualitatively agrees with the elastic behavior expressed by eq. 3.8. The mechanism's resulting stiffness estimated from fig. 3.11 (at $f = 25$ Hz) amounts to 0.9 N/µm.

Discussion of Crawling Motion

With NanoCrawl, presented in this section, we have achieved a positioning accuracy of 10 nm within a large working range and a maximum speed of 0.37 mm/s. The suitable range of load forces is about $|F_L| < 2$ N.
These limitations originate from the mechanism's design. To obtain a better performance it has to be modified as follows:

- increase of the stiffness k_P and k_C to obtain a stiffer load characteristic.
- higher magnetic forces F_N to improve the load capacity.
- decrease of the rise and fall times of the currents, i.e., decrease of the inductance L or increase of the supply voltage, to allow for higher stepping frequencies and consequently higher speed.
- smaller masses m_1 and m_2 to decrease the inertial forces and thus to allow for faster operation.

Commercially available Inchworm motors [BURLEIGH95] use tube piezos to clamp on ceramic rods. Due to their compact design and their high load capacity of several Newtons they are excellently suited for high resolution single-DOF positioning tasks. However, if a multi-DOF positioner is required, the use of magnetic clamps, as with NanoCrawl, is the better strategy, since it leads to less complicated mechanisms. An example of a planar crawling mechanism with three DOFs is shown in [ZESCH93].

As discussed above, the weakest and most expensive elements in crawling drives are the clamps. In the next section we will present a stepping principle that does not require any clamps.

3.3 The Inertial Principle

Compared to crawlers, inertial drives are simpler in design. Let us consider a stepping drive with an asymmetrical leg structure, as shown in fig. 3.12. One leg – the body mass m_1 – rests on a substrate, whereas the other – hereinafter the impact mass m_2 – is suspended by the actuator P, which connects the two legs.
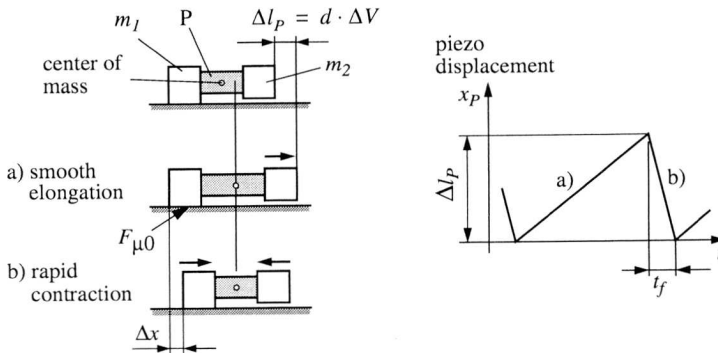

Fig. 3.12: *The principle of inertial drive*

The system can be moved utilizing the nonlinear frictional characteristics (cf. appendix A) as follows: During a smooth elongation of the actuator P, m_2 is shifted while the static friction $F_{\mu0}$ prevents m_1 from moving (a). After having reached its final elongation Δl_P, P is rapidly shrunk (b), which induces an inertial force on m_1. If this force exceeds the static frictional force $F_{\mu0}$, both m_2 and m_1

move towards the mechanism's center of mass yielding a net displacement Δx of the complete mechanism.

In its general form – both m_1 and m_2 are non-zero – the inertial drive is known as *Impact Drive* [HIGUCHI90]. A prototype of an impact drive and its performance is discussed in section 3.3.2. The setup, when m_1 decreases towards zero, is often called *Stick-Slip Drive* (cf. fig. 3.21) [POHL87][HOWALD92][4]. A rotational stick-slip drive is presented in section 3.3.3.

3.3.1 Model of the Inertial Drive

Basically, an inertial drive mechanism can be treated as a two-mass system with an actuator in-between, as shown in fig. 3.13.
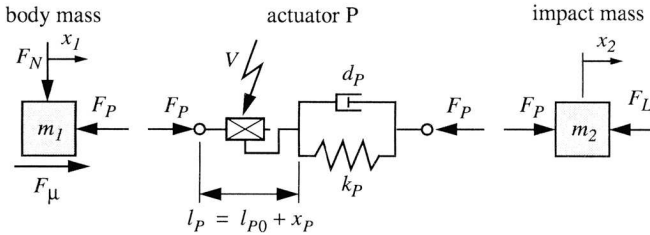

Fig. 3.13: *Mechanical model of an inertial drive loaded with an external load force F_L.*

Basic Relations

The motion of the two masses m_1 and m_2 is given by the equations

$$m_1 \cdot \ddot{x}_1 = -F_P + F_\mu, \tag{3.15}$$

$$m_2 \cdot \ddot{x}_2 = F_P - F_L, \tag{3.16}$$

where F_μ denotes the frictional force between m_1 and the substrate, F_L is an external load acting against the direction of motion and F_P is the internal force affecting the actuator (cf. appendix B.2).

---

4. This principle is also used in a modified form for vibration feeders to transport small objects or bulk goods. In that context, the objects act as m_2.

As long as the *slip condition* is satisfied, i.e.,

$$\dot{x}_1 \neq 0, \tag{3.17}$$

F_μ can be substituted by $-\text{sgn}(\dot{x}_1) \cdot F_{\mu k}$ (cf. eq. A.2). The equations of motion for the inertial drive can then be written as

$$\begin{bmatrix} m_1 & 0 \\ 0 & m_2 \end{bmatrix} \cdot \begin{Bmatrix} \ddot{x}_1 \\ \ddot{x}_2 \end{Bmatrix} + \begin{bmatrix} d_P & -d_P \\ -d_P & d_P \end{bmatrix} \cdot \begin{Bmatrix} \dot{x}_1 \\ \dot{x}_2 \end{Bmatrix} + \begin{bmatrix} k_P & -k_P \\ -k_P & k_P \end{bmatrix} \cdot \begin{Bmatrix} x_1 \\ x_2 \end{Bmatrix} =$$
$$= \begin{Bmatrix} -\text{sgn}(\dot{x}_1) \cdot F_{\mu k} \\ -F_L \end{Bmatrix} + d_P \begin{Bmatrix} -\dot{x}_P \\ \dot{x}_P \end{Bmatrix} + k_P \begin{Bmatrix} -x_P \\ x_P \end{Bmatrix} \quad \Leftrightarrow \quad \dot{x}_1 \neq 0 \tag{3.18}$$

with x_P the actuator displacement $x_P = d \cdot V$. Notice that the gravity force is not treated explicitly. It is considered to be included in the preload force F_N, which presses m_1 to the ground, and the load force F_L. For an inclination angle β against the horizontal plane, (cf. fig. 3.19) the corresponding contributions are $(m_1 + m_2) \cdot g \cdot \cos\beta$ and $(m_1 + m_2) \cdot g \cdot \sin\beta$, respectively.

For the sticking case, if $\dot{x}_1, \ddot{x}_1 = 0$, the mathematical model degenerates to the 1-DOF *equation of fine motion*

$$m_2 \ddot{x}_2 + d_P \dot{x}_2 + k_P x_2 = -F_L + (d_P \dot{x}_P + k_P(x_P + x_1)) \tag{3.19}$$

The drive remains in this state as long as the value of F_μ is smaller than the static friction $F_{\mu 0}$. Using eq. 3.15 and eq. 3.16, we can then write the *stick condition*

$$|F_\mu| = |m_2 \ddot{x}_2 + F_L| \leq F_{\mu 0} = \mu_0 \cdot F_N. \tag{3.20}$$

Since there is steady switching between these two linear models (eq. 3.18 and eq. 3.19) according to the corresponding limit conditions (eq. 3.17 and eq. 3.20 respectively), it is not possible to write the response $x_1(t)$, $x_2(t)$ to an arbitrary input signal $x_P(t)$ in an explicit form. However, the step size Δx can be calculated analytically for a given periodic voltage wave form with an angular frequency of $\Omega = 2\pi \cdot f$ and the assumptions

$$\frac{\Omega}{\omega_0} \ll 1 \ , \quad \omega_0 = \sqrt{\frac{k_P}{m_2}} \quad \text{and} \quad \frac{d_P}{m_2} \gg \Omega, \tag{3.21}$$

i.e., neglect of the transient phase (cf. fig. 3.14, 4). Using these simplifications, we can add the two lines of eq. 3.18 and substitute the position of m_2 with $x_2 = x_1 + x_P$ to obtain the equation of motion in its reduced form as

$$(m_1 + m_2) \cdot \ddot{x}_1 = -\text{sgn}(\dot{x}_1) \cdot F_{\mu k} - F_L - m_2 \cdot \ddot{x}_P. \tag{3.22}$$

This expression for $\ddot{x}_1$ can be integrated numerically or analytically to obtain velocity and step size of the inertial drive for a particular input signal such as the triangular wave investigated below.

Triangular Input Wave

Assuming a triangular input wave form[5] (fig. 3.14, a) with a peak-to-peak voltage ΔV and a cycle ratio

$$\theta = \frac{t_f}{T}, \tag{3.23}$$

we can draw velocity (fig. 3.14, b) and displacement (fig. 3.14, c) of the inertial drive. The net step size Δx is obtained by integrating the velocity of the body mass $\dot{x}_1(t)$, which basically consists of phases of zero velocity (fig. 3.14, 1) and phases of constant – but not equal – acceleration: For the slip phases (2) and (3) the acceleration $\ddot{x}_1$ is given by

$$\ddot{x}_1 = \frac{1}{m_1 + m_2} \cdot (-\text{sgn}(\dot{x}_1) \cdot F_{\mu k} - F_L). \tag{3.24}$$

With the principle of conservation of momentum, i.e., $m_1 \cdot \Delta \dot{x}_1 = m_2 \cdot \Delta \dot{x}_2$, the velocity steps $\Delta \dot{x}_1$ during the transient phases (4) can be calculated with

$$\Delta \dot{x}_1 = -\Delta \dot{x}_P \cdot \frac{m_2}{m_1 + m_2} = \mp \frac{\Delta l_P}{T} \cdot \frac{1}{\theta(1 - \theta)} \cdot \frac{m_2}{m_1 + m_2}. \tag{3.25}$$

The velocity $\dot{x}_1$ at the begin of the shrinking phase (2) at $t = \varepsilon > 0$, $\varepsilon \rightarrow 0$ and at the begin of the expansion phase (3) at $t = t_f + \varepsilon$ can be written as

---

5. [BUECHI95] also looks at parabolic patterns. Because of their upper speed limit they are troublesome to control and thus they are not investigated in this work.
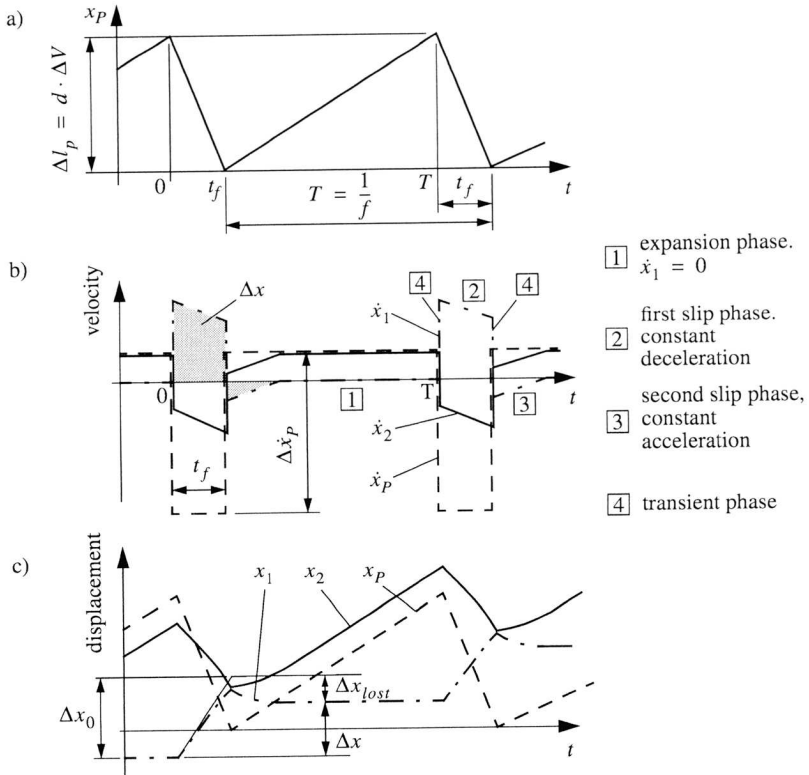
a)

b)

1	expansion phase. $\dot{x}_1 = 0$
2	first slip phase. constant deceleration
3	second slip phase, constant acceleration
4	transient phase

c)

Fig. 3.14: *Step pattern during inertial motion. (a) Input signal, (b) velocities, (c) displacements. The colored area in the velocity graph corresponds to the net displacement* Δx.

$$\dot{x}_1(\varepsilon) = -\Delta\dot{x}_P = \frac{\Delta l_P}{T} \cdot \frac{1}{\theta(1-\theta)} \cdot \frac{m_2}{m_1 + m_2}, \qquad (3.26)$$

$$\dot{x}_1(t_f + \varepsilon) = -\Delta\dot{x}_P + \int_0^{t_f} \ddot{x}_1(\tau)d\tau + \Delta\dot{x}_P = \frac{-F_{\mu k} - F_L}{m_1 + m_2} \cdot t_f. \qquad (3.27)$$

The double integration of the acceleration $\ddot{x}_1$ (cf. eq. 3.24) using the above starting velocities results in a net displacement of

$$\Delta x = \underbrace{\Delta l_p \cdot \frac{m_2}{m_1 + m_2} \cdot \frac{1}{1 - \theta}}_{\Delta x_0} - \underbrace{\frac{\theta^2 \cdot T^2}{m_1 + m_2} \cdot F_{\mu k} \cdot \frac{F_{\mu k} + F_L}{F_{\mu k} - F_L}}_{\Delta x_{lost}} \qquad (3.28)$$

Basically, the step size Δx is the difference between an *ideal step size* Δx_0, depending on the mass ratio and the driving signal, and the *lost motion* Δx_{lost}, which accounts for friction and load effects. For an infinitesimally short fall time t_f the step size become a theoretical maximum of

$$\lim_{\theta \to 0} \Delta x = \Delta l_p \cdot \kappa \qquad (3.29)$$

where κ is the impact factor given by

$$\kappa = \frac{m_2}{m_1 + m_2} . \qquad (3.30)$$

Notice that for the case of an ideal saw-tooth wave form ($\theta \to 0$), Δx_{lost} diminishes to zero, independent of the coefficient of friction, as long as none of the limitations of operation (eq. 3.32 to eq. 3.34) is violated.

Limitations of Inertial Motion

There are several limits that have to be considered in order to achieve a controlled forward propulsion:

- The fall $t_f = T \cdot \theta$ time must be smaller than the rise time $t_r = T(1 - \theta)$:

$$t_f < t_r \quad \Leftrightarrow \quad \theta < \frac{1}{2} . \qquad (3.31)$$

- The absolute value of the load F_L must be smaller than the friction $F_{\mu k}$, i.e.,

$$\left| F_L \right| < F_{\mu k} . \qquad (3.32)$$

Otherwise the system is no longer able to return from the slip phase back to the stick phase. This includes the singular case of $\mu \to 0$, for which the iner-

tial drive would theoretically need an infinite time to accelerate or decelerate.

- For $F_L > 0$ there are two constraints: Firstly, the slip of m_1 has to stop before the next step arises, i.e., t_r has to be longer than the length of the second slip period $t_{slip, 2}$ (fig. 3.14, 3), which is obtained from eq. 3.27 and eq. 3.24 as

$$t_{slip, 2} = \frac{-\dot{x}_1(t_f + \varepsilon)}{\ddot{x}_1 \big|_{\dot{x}_1 < 0}} = \frac{\dfrac{F_{\mu k} + F_L}{m_1 + m_2} \cdot t_f}{\dfrac{1}{m_1 + m_2}(F_{\mu k} - F_L)} = t_f \cdot \frac{F_{\mu k} + F_L}{F_{\mu k} - F_L}. \quad (3.33)$$

After some transformations, the condition $t_{slip, 2} < t_f$ can be written as

$$F_L < F_{\mu k}(1 - 2\theta) \quad (3.34)$$

As the second condition for $F_L > 0$, the net displacement Δx (cf. eq. 3.28) has to be positive, i.e., $\Delta x_0 > \Delta x_{lost}$. This yields an upper limit for t_f given by

$$t_f = T \cdot \theta < \sqrt{\Delta l_P \cdot \frac{m_2}{1 - \theta} \cdot F_{\mu k} \cdot \frac{F_{\mu k} - F_L}{F_{\mu k} + F_L}} \quad (3.35)$$

Load Behavior

As shown in fig. 3.15, the load dependency of the inertial drive is twofold. Firstly, according to eq. 3.28, Δx decreases with increasing F_L. Secondly, the permissible load range, described by eq. 3.32, eq. 3.34, and eq. 3.35, grows with the frictional force $F_{\mu k}$, since working against a load requires a minimum value of $F_{\mu k}$. The optimum $F_{\mu k, opt}$ that maximizes Δx can be derived from eq. 3.28 and is given by

$$\Delta x = \max \quad \Rightarrow \quad F_{\mu k, opt} = (\sqrt{2} + 1) \cdot F_L, \quad (3.36)$$

which is the common tangent to all load curves $\Delta x_{lost}(F_L)$ indicated by the dashed line in fig. 3.15. The minimum lost motion becomes

$$\Delta x_{lost,min} = (3 + 2 \cdot \sqrt{2}) \cdot \frac{(\theta \cdot T)^2}{m_1 + m_2} \cdot F_L. \quad (3.37)$$

However, it is the better strategy to operate in a suboptimal regime, i.e., at a $F_{\mu k}$ larger than the theoretically calculated $F_{\mu k, opt}$. This allows for tackling model
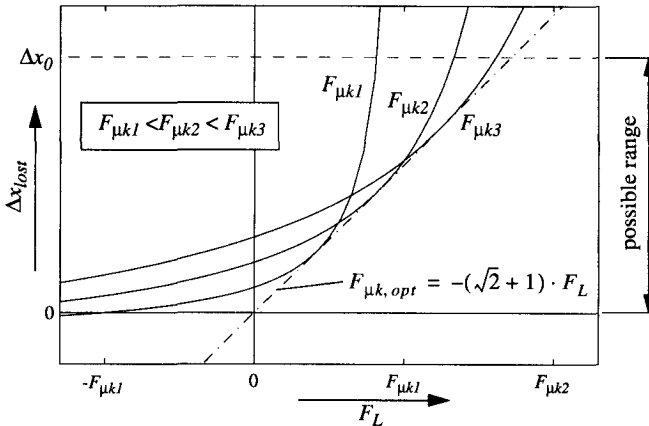
Fig. 3.15: *Load characteristic of the inertial drive at different frictional forces $F_{\mu k}$. Notice that operation is only possible within the range given by eq. 3.32 to eq. 3.35. The common tangent to all curves (dashed) indicates the optimum value for the frictional force $F_{\mu k,opt}(F_L)$.*

inaccuracies and parameter variations, e.g. the large uncertainty in friction. Additionally, operation far from the limits minimizes the influence of friction and therefore leads to smaller variations in the step size [BUECHI96].

The basic configuration of an inertial drive is sketched in fig. 3.12. For practical applications this setup has to be modified to obtain a symmetric mass distribution about the x-axis and a precise guidance. A realization of an impact drive – *NanoStep* – is presented in the following section.

3.3.2 NanoStep - A Translational Impact Drive

We built NanoStep to test inertial motion. It is a 1-DOF impact drive and consists of two masses m_1 and m_2 connected by a piezo-stack actuator, as illustrated in fig. 3.16. Similar to NanoCrawl (section 3.2.2), m_1 runs in a V-groove rail on five ruby hemispheres. Fig. 3.17 shows a picture of the prototype and table 3.3 indicates its parameters.
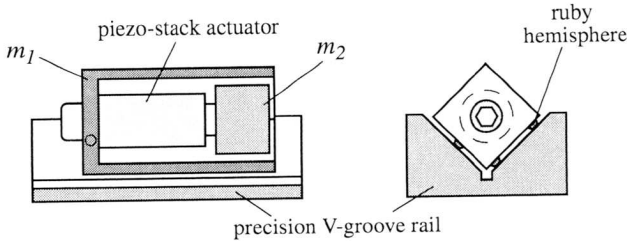
Fig. 3.16: *Sketch of the test-impact drive NanoStep.*

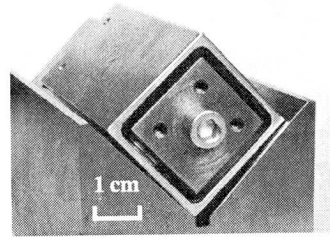|	
body mass m_1	95.4 g
impact mass m_2	201.6 g
impact factor κ	0.68
piezo voltage V	0-100 V
max. displacement Δl_P	8.9 μm
piezo's natural freq.	10 kHz
coeff. of friction $\mu_0 \approx \mu_k$	0.12

Tab. 3.3: *Data of NanoStep.*

Fig. 3.17: *Photograph of NanoStep.*

Rough Motion

The motion of the unloaded inertial drive, shown in fig. 3.18, qualitatively agrees well with the analytical prediction (cf. fig. 3.14, c). For a voltage ΔV of 80 V, i.e., a piezo displacement of $\Delta l_P = 7.2$ μm, we obtained a step size $\Delta x = 2.6$ μm. The displacement of m_1 just after the rapid contraction phase $(t = t_f + \varepsilon)$ of 4.8 μm yields a rough estimate for the impact factor $\kappa = 0.66$. This corresponds with the value of 0.68 obtained from the calculation based on the mass ratio (cf. eq. 3.30).

However, with the actual parameters (cf. table 3.3) the lost motion Δx_{lost} should be 0.42 μm instead of 2.4 μm reckoned from the graph. The reason for this can be found in the strong vibration during the transient phase after the piezo's rapid contraction. This dither effect[6] leads to a net coefficient of friction which is much smaller than the previously measured value and consequently yields a braking distance larger than the calculated one.

---

6. For certain applications, dither is intentionally used to decrease the effective friction.
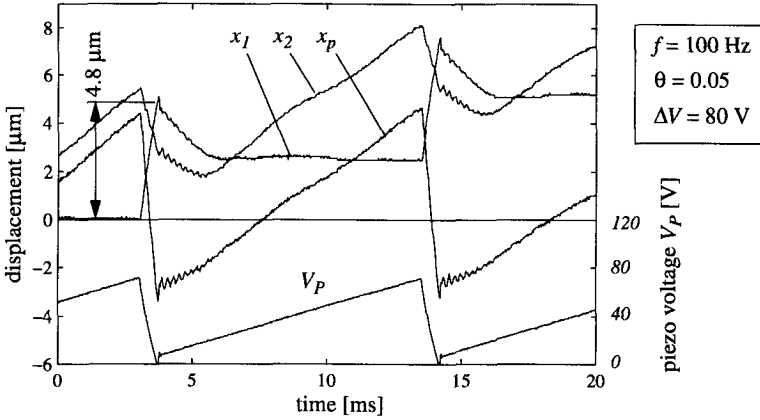

Fig. 3.18: *NanoStep's Motion pattern at unloaded operation ($F_L = 0$).*

From eq. 3.24 to eq. 3.28 we can deduce that the lost motion Δx_{lost} is equally distributed to both slip phases (cf. fig. 3.14, 2 & 3) for $F_L = 0$ and $\mu_k = $ const. In the above case with $\mu_k = 0.12$, this results in a displacement of $\Delta x_{slip} = \Delta x_{lost} / 2 = 0.24$ µm for each slip phase. However, from the fig. 3.18 we can infer a slip distance during the second slip phase of $\Delta x_{slip,2} = 2.4$ µm. Since the acceleration $\ddot{x}_1$, and consequently Δx_{slip}, is inverse proportional to the actual coefficient of friction, i.e., $\mu \cdot \Delta x_{slip} = $ const, we can estimate the effective coefficient of friction during the dither phase μ_{dither} by

$$\mu_{dither} \cdot \Delta x_{slip,2} = \mu_k \cdot \frac{\Delta x_{lost}}{2} \quad \Rightarrow \quad \mu_{dither} = 0.011. \quad (3.38)$$

This is less than 10% of the value measured in the static experiment. The minimization of this oscillations at the end of each step is discussed in section 4.2.6.

Load Characteristics

Referring to fig. 3.15, the inertial drive's step size strongly depends on the load. This characteristic was measured by inclining the NanoStep's rail with an angle β against the horizontal direction. Due to the 45°-inclination of the V-rail treads, the sum of all normal forces F_N supporting the mechanism against gravity becomes $\sqrt{2} \cdot (m_1 + m_2) \cdot g \cdot \cos\beta$.
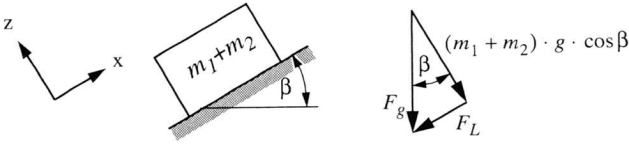
Fig. 3.19: *Loading NanoStep by inclining the rail.*

Apparently, the frictional and load forces are given by

$$F_{\mu k} = \mu_k \cdot F_N = \sqrt{2} \cdot \mu \cdot (m_1 + m_2) \cdot g \cdot \cos\beta, \qquad (3.39)$$

$$F_L = (m_1 + m_2) \cdot g \cdot \sin\beta, \qquad (3.40)$$

respectively, where g denotes the acceleration due to gravity. With $\tilde{\mu} = \sqrt{2} \cdot \mu_k$ the step size $\Delta x(\beta)$ deduced from eq. 3.28 results in

$$\Delta x(\alpha) = \Delta l_p \cdot \frac{\kappa}{1-\theta} - g\tilde{\mu}(\theta T)^2 \cdot \cos\beta \cdot \frac{\tilde{\mu}\cos\beta + \sin\beta}{\tilde{\mu}\cos\beta - \sin\beta}. \qquad (3.41)$$

Fig. 3.20 demonstrates the close agreement between the mathematical model and the measurements. Preloaded by the gravitational force only, NanoStep is able to
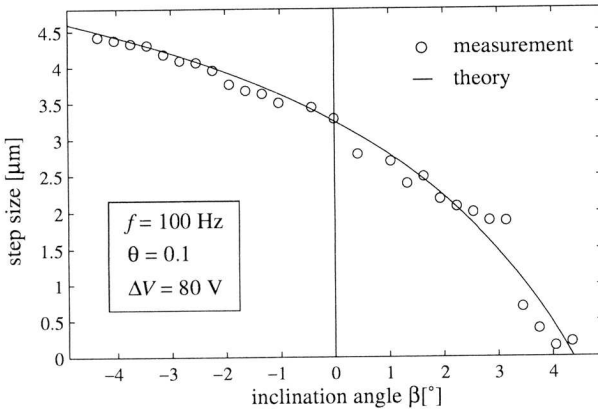

Fig. 3.20: *Theoretical and measured step size / load characteristic of NanoStep moving on an inclined plane.*

climb up a slope of 4.6°. This value corresponds to about 40% of the friction angle $\beta_\mu = \text{atan}(\tilde{\mu}) = 9.7°$, which agrees well with the theoretical model (eq. 3.36). Larger angles could be achieved by introducing additional preload forces.

As one can derive from eq. 3.28, the step size's sensitivity to variations in friction $|\delta\Delta x/\delta F_\mu|$ increases with larger loads F_L. This effect is confirmed by the increasing uncertainty of the step size at large inclination angles β in fig. 3.20.

Until here, we have only investigated translational stepping drives. However, the inertial principle is also appropriate for precise rotations. To demonstrate this, we have built Nanocrab, shown in the following section.

3.3.3 NanoCrab - A Rotational Stick-Slip Drive

The step size Δx of the inertial drive (cf. eq. 3.28) reaches a maximum if m_1 is much smaller than m_2 ($\kappa \to 1$). To achieve this, the design must be changed as follows: The actuator P has to be attached to the ground, whereas the impact mass m_2 (hereinafter m) is no longer fixed to the P but just laid on it. The resulting setup – now termed *stick-slip drive* – is sketched in fig. 3.21.
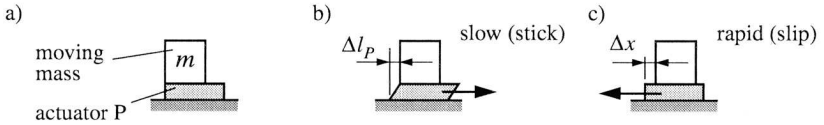

Fig. 3.21: *Scheme of the stick-slip drive, (a) setup, (b) slow deformation, (c) rapid re-deformation.*

Compared to the impact drive (cf. section 3.3.2), the stick-slip drive has the advantage of requiring less elements. Particularly, the absence of a moving actuator helps to simplify the mechanical design and the power supply.

Basic Relations

For the limit $m_1 \to 0$ eq. 3.28 can be simplified to

$$\Delta x = \frac{\Delta l_P}{1-\theta} - \frac{(\theta \cdot T)^2}{m} \cdot F_{\mu k} \cdot \frac{F_{\mu k} + F_L}{F_{\mu k} - F_L}. \qquad (3.42)$$

In the rotational case, the expressions for translation of eq. 3.42 are substituted by the corresponding rotational variables, i.e., $\Delta l_P \to \Delta l_P / r$ (actuator output), $\Delta x \to \Delta \varphi$ (displacement), $m \to I_z$ (inertia) and $F \to M$ (torque). This yields an angular step size of

$$\Delta \varphi = \Delta \varphi_0 - \Delta \varphi_{lost} =$$

$$= \frac{\Delta l_P}{r} \cdot \frac{1}{1 - \theta} - \frac{(\theta \cdot T)^2}{I_z} \cdot M_{\mu k} \cdot \frac{M_{\mu k} + M_L}{M_{\mu k} - M_L} , \qquad (3.43)$$

where r denotes the rotor radius and $M_{\mu k}$ the frictional torque given by eq. 3.44.
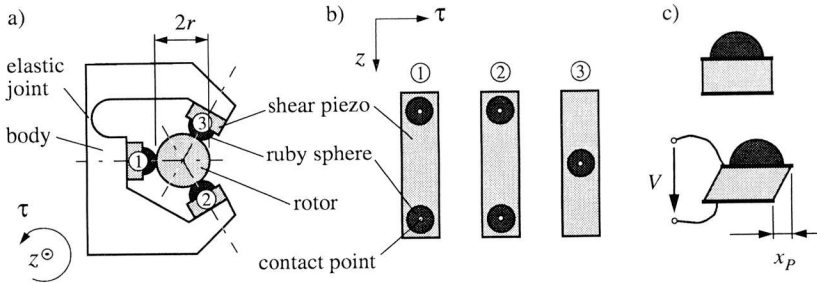
Design of NanoCrab

Fig. 3.22: *Design of NanoCrab: (a) cross section, (b) contact points at the rotor's perimeter arranged in three bearing planes, (c) actuator deformation caused by a voltage V.*

NanoCrab[7], sketched in fig. 3.22, is a rotational micro motor based on the stick-slip principle. The rotor, the only moving part, is a steel shaft of 3 mm diameter. It is supported by five ruby hemispheres, which are used for both suspension and propulsion. The rubies are glued on top of three shear piezo elements (d_{15}-mode, cf. appendix B.1) forming three bearing planes (cf. fig. 3.22, b). Note that there are no additional bearings to guide the rotor.

An elastic joint structure (cf. fig. 3.22, a) provides a preload force F_N necessary to produce sufficient friction. It also fixes the rotor position precisely in four

---

7. The name originates from the cross section of NanoCrab, which looks like the claw of a crab.

DOFs. The remaining two DOFs are, obviously, the motor's output, i.e., the z-rotation (φ_z), and the rotor's axial translation (z). The latter can be constrained by means of either a circular V-groove in the rotor or an additional axial bearing.

When a voltage V is applied to the piezo ceramics, they move the ruby bearings tangentially to the rotor's circumference in τ–direction (cf. fig. 3.22, c), thereby forcing the axle to rotate without any backlash or undesirable friction. Theoretically, infinite angles can be achieved using stick-slip motion (cf. fig. 3.21). The frictional torque $M_{\mu k}$ necessary for operation against a load torque M_L (cf. fig. 3.23) can be calculated with eq. 3.44.
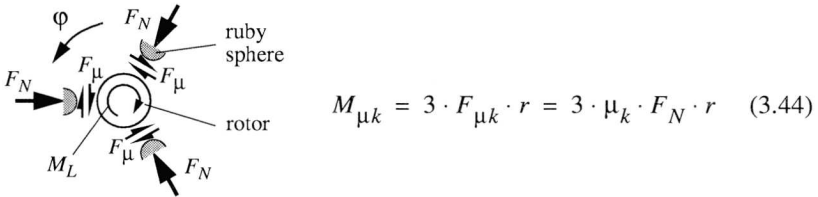

$$M_{\mu k} = 3 \cdot F_{\mu k} \cdot r = 3 \cdot \mu_k \cdot F_N \cdot r \quad (3.44)$$

Fig. 3.23: *Generation of the frictional torque $M_{\mu k}$ by preloading NanoCrab's rotor.*

Compared to electromagnetic motors, NanoCrab operates at low speed and relatively high torques, which eliminates the need for additional gear units. A further advantage is the inherent stability. This offers the possibility of open-loop opera-

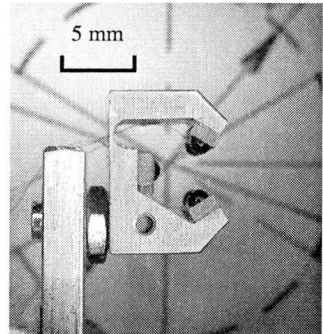| size	$8 \times 8 \times 11$ mm^3
rotor diameter $2r$	3 mm
nominal step size $\Delta\varphi_{nom}$	0.14 mrad
angular resolution	< 0.1 µrad
working frequency f	< 2 kHz
max. speed	1 rpm
max. holding torque $M_{\mu 0}$	0.92 mNm
max. load torque M_{Lmax}	0.37 mNm
max. driving volt. ΔV_{max}	270 V
piezo constant d (PXE71)	1.6 nm/V

Tab. 3.4: *Data of NanoCrab*

Fig. 3.24: *Cross section of NanoCrab (without rotor).*

tion and position holding without power consumption. NanoCrab's principal parameters and a photo are presented in table 3.4 and fig. 3.24, respectively.

In the following, we investigate the influence the preload force, the rotor inertia and elasticity on the step size, as well as the axial stability of NanoCrab.

Preload Characteristics

Fig. 3.25 shows the dependency of both the step size $\Delta\varphi$ (at zero load) and the maximum load torque M_{Lmax} from the preload force F_N.
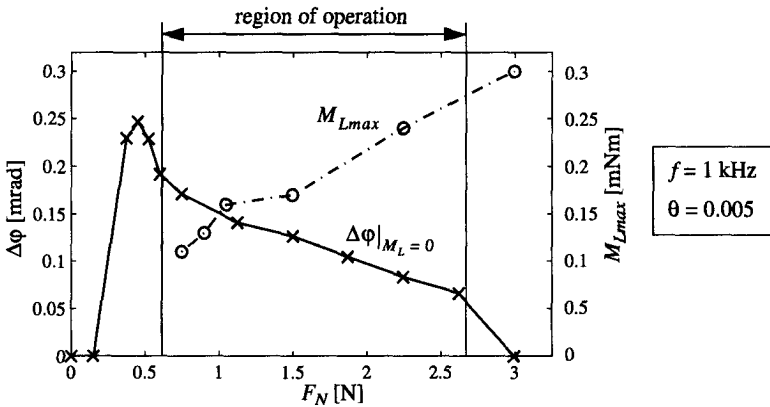

Fig. 3.25: *NanoCrab's step size (at $M_L = 0$) and maximum output torque as a function of the preload force F_N.*

In the region of operation, i.e., from $F_N = 0.6$ N up to 2.7 N, $\Delta\varphi$ decreases and M_{Lmax} grows approximately linear with increasing $M_\mu \propto F_N$ in accordance with eq. 3.43 and eq. 3.44. This opposing behavior allows for adjusting the motor's impedance, i.e., the ratio between torque and speed $\omega = \Delta\varphi \cdot f$, by varying F_N. However, the range of adaptation is limited. On one side, the drive becomes unstable for $F_N < 0.6$ N. On the other side, the rotation stops at large preloads F_N due to the finite mechanical stiffness of the actuation structure, as explained below.

Influence of Rotor Inertia and Elasticity

In this experiment, we varied the rotor inertia I_z. As fig. 3.26 demonstrates, the step size $\Delta\varphi$ grows, i.e., $\Delta\varphi_{lost}$ decreases, with increasing I_z in accordance with

eq. 3.43. In the region $\Delta\varphi < 0.05$ mrad the inertial motion is significantly impaired. We explain this effect with the axle's surface roughness which is in the same order of magnitude or larger than the actuator step Δl_P.
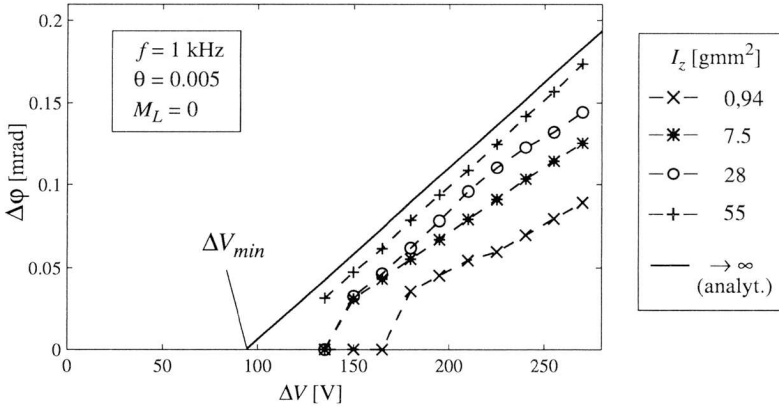

Fig. 3.26: *Step size / voltage behavior for different rotor inertias I_z.*

During the slip phases (cf. fig. 3.21, c), the actuators and the supporting structure are loaded by the frictional torque $M_{\mu k}$. As shown in fig. 3.27, the resulting elastic deformation $\Delta x_{el} = r \cdot \Delta\varphi_{el}$ – termed *elastic loss* – yields a reduced stroke $\Delta\tilde{l}_P$ at the contact points, where slip takes place. It is given by

$$\Delta\tilde{l}_P = \Delta l_P - \Delta x_{el} = \Delta l_P - r \cdot \Delta\varphi_{el} = d \cdot \Delta V - r \cdot \frac{M_{\mu k}}{k_{\varphi el}}. \qquad (3.45)$$
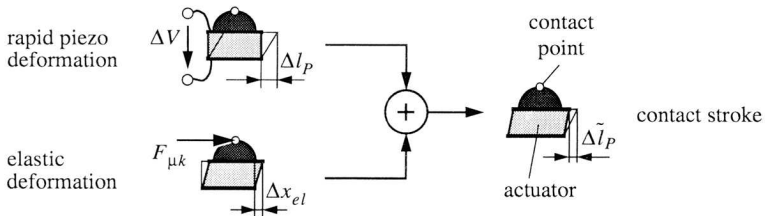

Fig. 3.27: *Evaluation of the displacement of the contact points $\Delta\tilde{l}_P$ during the rapid deformation (slip) phase.*

Herein $k_{\varphi el}$ denotes the drive's stiffness in φ_z-direction.

The elastic loss defines a minimum operation voltage ΔV_{min} below which $\Delta \tilde{l}_P$ becomes zero. Practically, this means that for $\Delta V \leq \Delta V_{min}$ the actuator is no longer able to generate a force large enough to overcome the friction.

From fig. 3.26 we estimated a value of $\Delta V_{min} = 92$ V for the theoretical case of $I_z \to \infty$, i.e., $\Delta \varphi_{lost} = 0$. Then, according to eq. 3.43, the step size $\Delta \varphi$ becomes equal to the contact stroke $\Delta \tilde{l}_P$, for $\theta \ll 1$. For $\Delta V = \Delta V_{min}$, i.e., $\Delta \varphi = 0$, and the above parameters we can thus write

$$\Delta \varphi \Big|_{\substack{\Delta V = \Delta V_{min} \\ \theta \ll 1}} = \Delta \tilde{l}_P = d \cdot \Delta V_{min} - r \cdot \frac{M_{\mu k}}{k_{\varphi el}} = 0. \tag{3.46}$$

After solving this relation for $k_{\varphi el}$ and inserting $M_{\mu k} = 0.92$ mNm, which was gained from static measurements, we obtain a value for the rotational elasticity of $k_{\varphi el} = 9.4$ Nm/rad.

To conclude, at an operation voltage $\Delta V = 270$ V more than 35% of NanoCrab's piezo displacement is lost due to lost motion and elasticity. There are two modifications to increase the step size or to lower ΔV_{min}. Firstly, the rotor mass/inertia has to be made as large as possible in order to decrease $\Delta \varphi_{lost}$. Secondly, the drive's mechanical design has to be stiffened to reduce $\Delta \varphi_{el}$.

Axial Stability

Precise manipulations require accurate rotations about particular axes. One way to achieve this is keeping the axle's runout as small as possible by mechanical means, e.g. with precise guidance. For NanoCrab, the runout is determined by the shape of the rotor, which is a roller of a needle bearing[8].

Fig. 3.28 shows the rotor's radial displacement for three full rotations scanned with a probe, which itself was tracked by an interferometer. The standard deviation of the runout is less than 120 nm with cross correlation factors between different revolutions of the order of 0.8. The non-repeatable part is less than 40 nm. Sporadic spikes, e.g. at 0.6 mrad, are explained with uncertainties in the displacement measurement, which is based on a mechanical scanning technique. They are neglected in our considerations.

---

8. The manufacturer specifies the maximum error in cylindricity to about 0.5 µm.
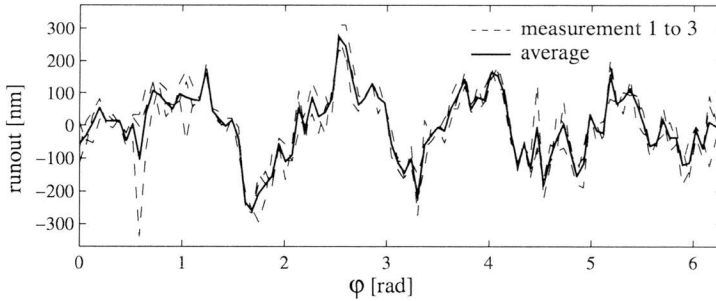
Fig. 3.28: *Runout of NanoCrab's rotor for 3 rotation.*

NanoCrab's excellent center stability can even be improved by using better axles – a cylindricity of 0.1 μm is state of the art for precise rollers – or by implementing a feed forward compensation to eliminate the systematic part of the error.

Application of Rotational Stick-Slip Motors

NanoCrab is used to rotate a tweezer in the our nanorobot (cf. section 2.4). A variant, *TableCrab,* acts to tilt the platform that positions microobjects under the microscope. Analogously to NanoCrab, it is composed of a magnetically preloaded rotor, i.e., a steel half-cylinder, and shear piezos for actuation. TableCrab's cross section is sketched in fig. 3.29. A photograph of the prototype
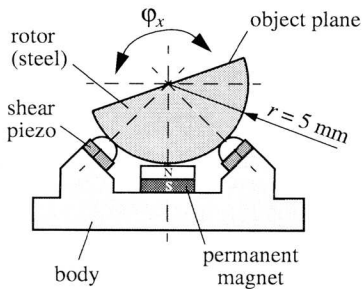

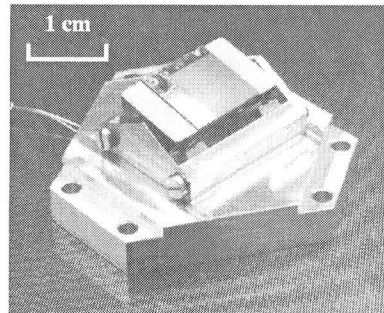**Fig. 3.29:** *TableCrab's cross section*

Fig. 3.30: *Prototype of TableCrab carrying a silicon wafer.*

is shown in fig. 3.30. It allows for concentrically tilting its object plane with a resolution of better than 0.03 μrad and has a tilt range of ±40°.

Inertial drives are able to act as joint motors for conventional serial-chain manipulators, too. Fig. 3.32 shows a 3-DOF microrobot driven by three stick-slip actuators. It positions loads of up to 1 g in its spherical workspace of 6 cm in diameter with a resolution of about 100 nm.
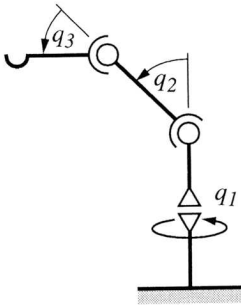

Fig. 3.31: *NanoCrane's kinematic setup: Spokey [BAUMANN95] rotates the vertical axis (q_1) whereas the shoulder (q_2) and the elbow (q_3) joints are driven by two modified NanoCrabs.*
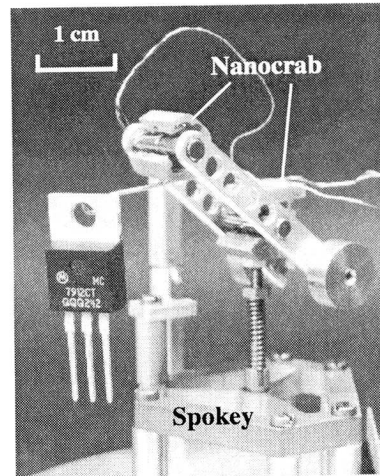

Fig. 3.32: *Photo of NanoCrane, a 3-DOF micro-robot based on stick-slip drives.*

3.4 Summary of Stepping Principles

In this section we investigated stepping principles for micropositioning. As a general merit, they combine a large working range with high resolution by switching between two modes of motion, i.e., between stepping and local positioning. We used piezoelectric actuation which allowed for simple and effective implementation. Two different concepts have been investigated and realized. Their major advantages and drawbacks are summarized in table 3.5.

	crawling	inertial motion
pros	+ fair repeatability + high load capacity, able to work against gravity + large range of stepping frequencies	+ fast positioning with very high resolution + extremely simple structure with one actuator per DOF + no clamps needed + easy expandable to multiple DOFs (cf. section 4.2)
	+highly dynamic and stable open-loop control	
cons	- additional actuators needed for clamping - small fabricational tolerances	- high demand to the bandwidth of the driving amplifier - sensitive to external forces - vibration excitation due to restricted wave forms
	-poor open-loop accuracy due to error propagation	

Tab. 3.5: *Comparison of stepping principles*

Crawling mechanisms are well suited for micropositioning tasks which need significant actuation force. Since a guiding structure is required, they are normally used for one-DOF mechanisms or as single actuators in complex kinematic chains. Conversely, **inertial drives** are well suited for positioning tasks almost free from loads, e.g. on a horizontal plane. Nevertheless, they are also adequate to work against loads, if sensor feedback is employed.

In the next chapter, we will apply stepping principles to actuate multi-DOF mechanisms for precise execution of spatial motions.

4 *Multi-Degree-of-Freedom*
Micropositioning

Conventional robotic structures are insufficient for high resolution manipulation in the microscopic domain for two reasons. Firstly, they use serial arrangements of articulated joints and links (fig. 4.1, a) [CRAIG89] to attain a workspace with multiple DOFs. Each actuator and link has to carry all subsequent ones. This leads to long and compliant structures and therefore, to large vibration amplitudes. Secondly, the resolution is limited by friction and play in the robot joints [ARMSTRONG91].

Solutions to both problems are investigated in the following chapter. Based on this foundation, two high resolution 3-DOF mechanisms are presented.

4.1 Mechanisms for Micropositioning

4.1.1 Parallel Structures

In contrast to serial-chain manipulators, *parallel structures* (fig. 4.1, b) connect a platform to the inertial system with several drive trains [MERLET93][CLAVEL88]. Often, such mechanisms consist of links, which are subject to pure tension or compression load, and – in contrast to serial manipulators – of active *and* passive joints. In fully parallel manipulators [STEWART65][HAN89] the actuators are
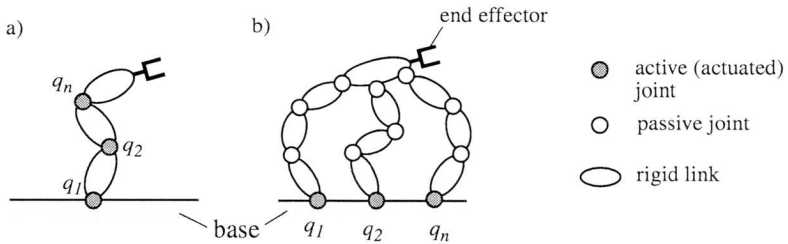
Fig. 4.1: *(a) Serial and (b) parallel chains*

fixed to the base system and therefore do not contribute to the moving mass. Parallel structures are stiffer than serial ones and consequently possess higher resonant frequencies.

The fundamental drawback of parallel manipulators is their limited working range, caused by self-collisions of different chains and a large number of singularities. Attempts have been made to expand the accessible volume with geometric optimization [HARA89] or by using redundant actuation [HAYWARD93]. However, since the desired displacements needed in micromanipulation are small (< 1 cm) compared to the robot's size (~10 cm), the problem of limited range is irrelevant. Also, the relatively small rotational range is not a real handicap, since in any case, the orientational range is limited by collisions with the microscope (cf. section 5.1.1) rather than by the mechanism itself.

More aggravating with parallel robots is the need for passive joints. In order to avoid friction and play we propose the use of flexible structures instead of conventional sliding or roller bearings (cf. section 2.2).

4.1.2 Flexible Structures

Flexible Hinges

Conventional bearings (fig. 4.2, a) are commonly replaced with discrete flexible hinges or pivots (fig. 4.2, b) to avoid friction or play. Usually, they are cut out of bulk material by electro discharge machining. They can be optimized for a large mechanical advantage, i.e., to be very compliant in the direction of motion but stiff in all transverse directions. By an appropriate combination of several pivots and links in a monolithic structure custom made mechanisms could be designed

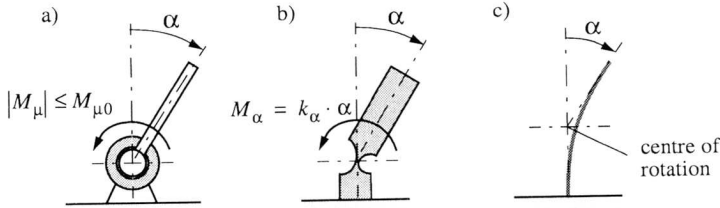[RONG94][SMITH92]. A hand module with six DOFs has been built by Arai [ARAI92].

Fig. 4.2: *Rotational joints: (a) cylindrical, (b) flexible hinge, (c) flexible beam with distributed deformation*

Fig. 4.3 shows a flexible pivot and its parameters. The angular and longitudinal stiffness k_α and k_x can be approximated with eq. 4.1 and eq. 4.2 [SMITH92], respectively, as long as h, $r \gg t$. E is the Young's modulus of the hinge material.
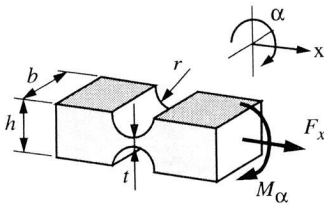
Fig. 4.3: *Flexible hinge*

$$k_\alpha = \frac{M_\alpha}{\alpha} = \frac{2Ebt^{5/2}}{9\pi r^{1/2}} \qquad (4.1)$$

$$k_x = \frac{F_x}{x} = \frac{E \cdot b}{\pi (r/t)^{1/2} - 2.57} \qquad (4.2)$$

$$\sigma = \frac{4E}{3\pi} \cdot \sqrt{\frac{t}{r}} \cdot \alpha + \frac{F_x}{bt} \qquad (4.3)$$

This technology reaches its limits, if the angle α of more than only a few degrees is required. Due to the extremely localized deformation in the narrow section, the mechanical stress σ, given by eq. 4.3, quickly exceeds the elastic limit. The effects are short life time and hysteresis due to plastic deformation.

The concept of Distributed Deformation

To increase the allowable deflection, one could think about distributing the highly localized deformation over a wider region. As an example, fig. 4.4 shows a thin beam with a cross section $t \times b$ loaded with a torque M_z and a force F_y. Using Euler's linear-elastic equation, the beam's deflection can be expressed by eq. 4.4.

Obviously, for a given angle α, the stress, given by eq. 4.6, scales with t/l instead of $\sqrt{t/r}$ for the hinge (cf. eq. 4.3). Thus, for a beam with l of the same dimension or bigger than the hinge's radius r, the mechanical stress is drastically decreased.
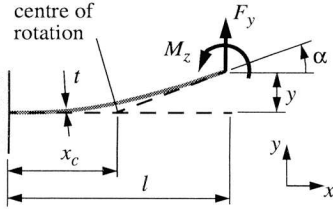
$$\begin{bmatrix} F_y l \\ M_z \end{bmatrix} = \frac{2EI_B}{l^2} \begin{bmatrix} 6 & -3 \\ -3 & 2 \end{bmatrix} \begin{bmatrix} y \\ \alpha l \end{bmatrix} \quad (4.4)$$

$$\text{with } I_B = \frac{t^3 b}{12} \quad (4.5)$$

Fig. 4.4: *Deflection of the linear, flexible beam subject to bending torque and lateral force load*

$$\sigma(x=0) = \frac{6(M_z + F_y l)}{t^2 b} \quad (4.6)$$

The benefit of the smaller stress is paid off by an lower transverse stiffness. Furthermore, the kinematic parameters depend on the load. For example, the flexible beam's center of rotation shifts from $x_c = l/3$ for $M_z = 0$ to $x = l/2$ for pure torque load ($F_y = 0$). This undesirable variation in geometry can be decreased with more sophisticated kinematic structures such as parallelograms [SMITH92] or cross-beam pivots [YANG94]. As mentioned in section 1.3, global sensor feedback is required anyway to achieve an accuracy sufficient for micropositioning. Thus, inaccuracies and changes in the geometry can be compensated with the corresponding actuators.

In the following sections, we present two manipulators relying on the aforementioned designs, i.e., parallel and flexible structures.

4.2 Abalone – A 3-DOF Impact Drive

In section 3.3 we have demonstrated, that the inertial principle is a practical way to precisely move objects on a horizontal tread. It is the aim of this chapter to investigate a planar inertial mechanism with three DOFs, allowing one to position objects in the field of view of the microscope (cf. section 5.1.1).

4.2.1 Planar Inertial Drive Configurations

A straightforward solution for a planar inertial mechanism with three DOFs could be envisioned as a serial stack of three single inertial drives, since it has well defined directions of actuation. However, this advantage is paid off by expensive guiding structures. For reasons of simplicity and rigidity, it is a better strategy to utilize a 3-DOF configuration which is supported by a planar joint. Fig. 4.5 shows possibilities to generate 3D-impacts (x, y, φ_z) acting upon a body mass m_1.
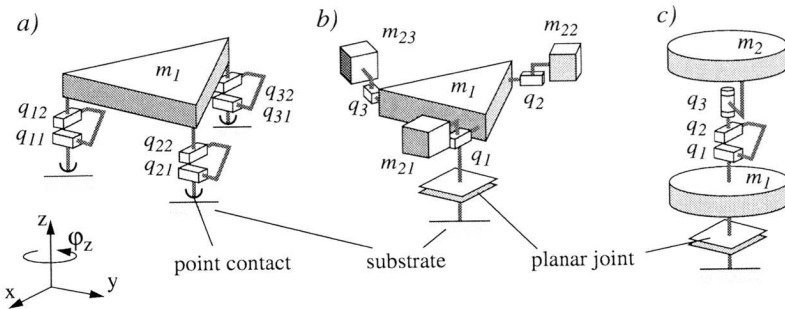
Fig. 4.5: *Different designs for planar inertial drives: (a) Stick-slip drive with three articulated legs, (b) with three impact masses, (c) setup of Abalone with 3D-impact mass. The actuators can be arranged in series, as sketched in (c), or in parallel.*

As a first solution, the *stick-slip principle* could be used, as proposed in [BREGUET95] (fig. 4.5, a). A platform (m_1), supported by three point-contact legs, slides on a flat substrate. Each leg can be moved in the x- and y-directions relative to the platform by two piezo elements (q_{i1} and q_{i2}). If an appropriate vector of voltages V_1 to V_6 is applied to the actuators, the platform moves in the desired direction on the plane. Rough motion, based on the stick-slip effect, and fine motion by continuously controlling the voltages is possible in each direction.

According to [HILLER95], we can calculate the mechanism's number of DOFs:
- number of bodies $\qquad n_B = 1$
- number of joints $\qquad n_J = 3$

Each leg has $n_{DOFi} = 7$ joint-DOFs, i.e., two actuated and five passive DOFs at the point contact. Hence, the number of DOFs for the mechanism results in

$$n_{DOF} = 6n_B - \sum_{i=1}^{n_J} (6 - n_{DOFi}) = 6 + 3 = 9.$$ (4.7)

Three DOFs are assigned to rough motion (between legs and substrate) and fine motion (body to legs) each. The three remaining DOFs theoretically allow for changing the distances between the contact points. However, to achieve a reliable behavior, these ego-motions have to be eliminated by additional constraints. Due to the piezos' nonlinearity and hysteresis, feedback control on the actuator level would be required to control the constraint space. In addition, the need for six actuators and amplifiers to control three DOFs makes it an expensive solution.

A different approach to planar inertial positioning is an impact drive with *multiple impact masses* (cf. fig. 4.5, b), as demonstrated in [YAMAGATA90]. The body m_1 rests on the tread with a planar joint. If the actuators are properly arranged, it can be moved arbitrarily in the plane using the inertial principle. However, relative to the substrate, each of the impact masses possesses only four DOFs: three for rough motion in the planar joint, and only one for fine motion with the corresponding actuator. As a consequence, the resolution of two DOFs is restricted to the resolution of rough motion (0.2 to 1 µm), which is far poorer than the actuators' theoretical limit.

The study of the basic impact drive configuration (cf. fig. 3.12) teaches us a simpler solution: Obviously, the body mass m_1 moves exactly in the direction of the impact generated by the actuator P and the mass m_2. Thus, in order to achieve a 3D-displacement, we simply have to control the direction of impact on m_1, i.e., *one single* impact mass m_2 has to be moved in the desired direction by an appropriate arrangement of three actuators, as sketched in fig. 4.5, c.

4.2.2 Design of Abalone[1]

Mechanism

Since the actuation structure has to be very stiff to generate 3D-impacts in a controllable manner, a parallel structure (cf. section 4.1.1) is selected for Abalone. It basically consists of two concentric platforms, which represent m_1 and m_2, con-

---

1. The name originates from a shell animal living in the sea. It has about the same contour as the mechanism proposed in this chapter.

nected by three actuator chains in parallel (fig. 4.6), similar to the one in [GOSSELIN96]. Each chain contains an elastically preloaded piezoelectric stack-actuator and two flexible joints (fig. 4.7, b). They correspond to the prismatic (P) and the rotational (R) joints, respectively, in fig. 4.6.

Abalone's body is cut out of a single piece of titanium[2] by wire erosion (fig. 4.7, a). The actuators are shrunk into the metal body with an excess of 3.5 μm at room temperature. This is a very compact and simple means of fixing the piezo ceramics, since there is no need for screws or glue, that would reduce the mechanism's quality and strength. In addition, it provides a built-in preload which is necessary to transmit tensile loads (fig. 4.7, b).
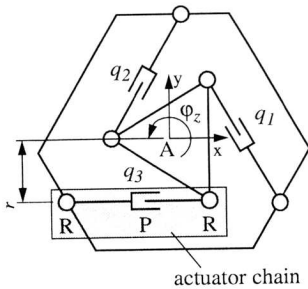
Fig. 4.6: *Kinematic Struc-ture of Abalone*
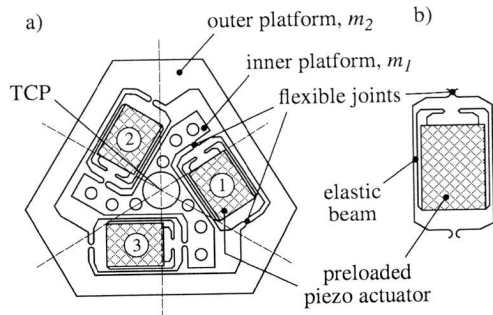
Fig. 4.7: *Sketch of (a) Abalone with (b) preloaded piezo stack-actuator*

By considering the actuator chain, i.e., the piezo element and the two corresponding hinges, as one joint with one translational and two rotational DOFs, the number of Abalone's internal DOFs can be written as

$$n_{DOF} = 3n_B - \sum_{i=1}^{3} (3 - n_{DOFi}) = 3 - 0 = 3 \qquad (4.8)$$

The outer platform m_2, carrying the tool center point (TCP), can be fine-positioned arbitrarily in all three directions by applying an appropriate voltage vector $V = [V_1, V_2, V_3]^T$ to the actuators. Rough positioning is performed with inertial

---

2. Compared to steel, aluminum, and bronze, titanium yields the best compromise between strength, fatigue limit, corrosion resistance, and internal damping.

motion. Fig. 4.8 shows a photograph of the prototype of Abalone and table 4.1 outlines its principal specifications.

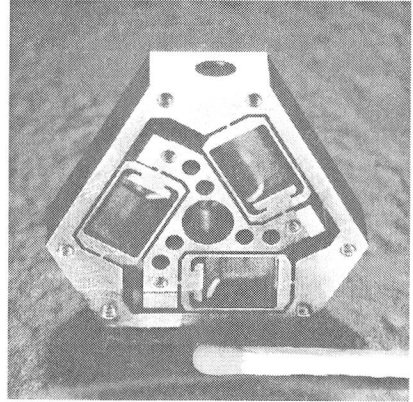|	*transl.*	*rot.*
DOF	x, y	φ_z
local range	5.3 μm	0.68 mrad
max. step size	3.4 μm	0.4 mrad
impact factor κ	0.73	0.81
speed at 400 Hz	1 mm/s	1.2 mrad/s
size	$32 \times 38 \times 9$ mm³	
mass	24g	
materials	titanium / PZT	
voltage range	0-100 V	

Tab. 4.1: *Data of Abalone*

Fig. 4.8: *Prototype of Abalone, bottom view*

Frictional Contact

Abalone is supported by three spherical legs, glued to the inner platform, i.e. m_1. For reasons of wear and to avoid excessive adhesion, we selected ruby hemispheres (Al_2O_3). Due to the non-linear characteristic of friction, the three DOFs of rough motion are coupled and cannot be treated independently. To minimize the crosstalk, the tread's surface has to be extremely flat, i.e., the size of asperities must be much smaller than the addressed nominal step size of the order of some microns. The friction has to be approximately constant all over the desired working range and, at the same time, has to be equal at all three legs. Furthermore the surface must not be damaged by the moving Abalone. A list of possible substrate materials is shown in table 4.2.

Although Abalone was able to run on steel and aluminum, the substantial surface roughness of our grinded test treads caused large disturbances during inertial motion. According to this criterion, both silicon and glass showed about the same, convenient behavior. However, after some test movements, the silicon surface was scratched by the rubies. Conversely, on the harder glass we could not observe any damage visible under a light microscope.

material	surface finish	roughness R_a [μm]	compression strength [N/mm²]	coefficient of friction μ
stainless steel	ground	1-5 μm	700	0.12
aluminum	eloxated	2-8 μm	240	0.14
silicon wafer	plane etched	< 20 nm	500-(3000)	0.11
glass	hardened	< 100 nm	1000-1300	0.10

Tab. 4.2: *Contact properties of possible tread materials (from [DUBBEL90]). The coefficient of friction μ against ruby was measured on an inclined plane.*

To conclude, we have chosen hardened glass as a tread for all further experiments. According to Hertz [DUBBEL90], the stress due to Abalone's weight becomes 43 N/mm² at the contact point for this material combination.

4.2.3 Kinematics and Workspace

Fine Motion Kinematics

The actuator strokes q_i are several orders of magnitude smaller than the dimensions of the mechanism. Hence, a linearized relation can be used to calculate the local kinematic properties. The geometric relation between small link extensions $Q = [q_1, q_2, q_3]^T$ and the resulting displacements $^A X = [x, y, r\, \varphi_z]^T$ of the TCP, expressed in Abalone's coordinate system A (cf. fig. 4.6), is given by

$$Q = J^{-1} \cdot {}^A X = \frac{1}{2}\begin{bmatrix} 1 & -\sqrt{3} & -2 \\ 1 & \sqrt{3} & -2 \\ -2 & 0 & -2 \end{bmatrix} \cdot {}^A X \quad \Rightarrow \quad J = \frac{1}{3}\begin{bmatrix} 1 & 1 & -2 \\ -\sqrt{3} & \sqrt{3} & 0 \\ -1 & -1 & -1 \end{bmatrix}, \quad (4.9)$$

where r = 8.7 mm is the distance of the actuators' center line to the geometric center of Abalone. As can be derived from eq. 4.9, points of constant rotation φ_z are located on planes perpendicular to the diagonal $q_1 = q_2 = q_3$ of the joint space Q. Due to the actuators' restricted stroke of

$$|q_i| \leq q_{max} = 2.5 \ \mu m \ , \qquad i = 1..3 \,^3 \qquad\qquad (4.10)$$

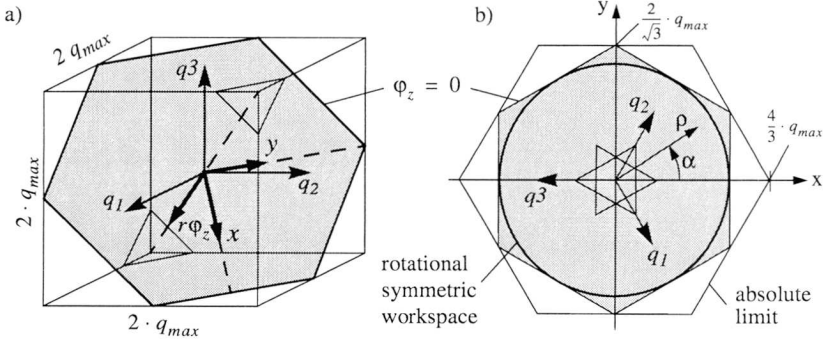these planes are limited by the side walls of a cube as shown in fig. 4.9, (a).

Fig. 4.9: *Local working range of Abalone: (a) 3D representation in the joint space Q, (b) 2D projection along $r\varphi_z$-axis showing the boundaries for pure translation and the absolute limit.*

Considering these constraints, we can draw the projection of the workspace along the $r\varphi_z$-axis (fig. 4.9, b).

Although the maximum displacement ρ_{max} is $4/3 \ q_{max}$, this value is not really useful, since it exists for six particular directions α only. Further, these motions inevitably cause an angular displacement of $\varphi_z = \pm q_{max}/3r$. Pure translation is possible only within the ($\varphi_z = 0$)-contour of fig. 4.9. Additionally, in order to achieve a homogenous behavior and to simplify the control, we limit the stroke ρ to q_{max}. (fig. 4.9, b). The remaining workspace is a double cone inscribed into the limit-cube of the joint space Q given by

$$|r\varphi_z| + |\rho| \leq q_{max} \ , \qquad \rho = \sqrt{x^2 + y^2}. \qquad\qquad (4.11)$$

Its axis coincides with the $r\varphi_z$-direction, whereas the base circle falls into the ($\varphi_z = 0$)-plane, as sketched in fig. 4.10

---

3. The stack actuators used in Abalone can only elongate. To allow for symmetric operation, a voltage offset, and consequently a displacement offset is introduced. Displacements up to $\pm q_{max}$, which is half of the original unidirectional working range, can then be performed bidirectionally.
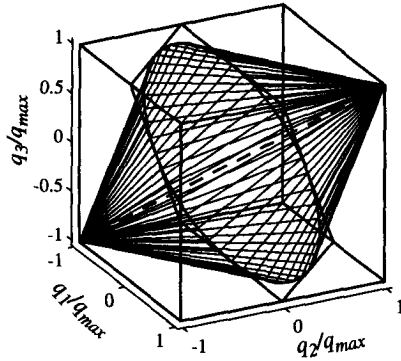
Fig. 4.10: *Practical, rotational symmetric workspace of Abalone*

Rough Motion Kinematics

Analogously to the 1-DOF case (cf. eq. 3.28), the step size vector $\Delta^A X$ – expressed in the body-fixed system A – is the difference of an ideal step $\Delta^A X_0 = K \cdot \Delta^A L_P$ and the lost motion $\Delta^A X_{lost}$. The actuator stroke $\Delta^A L_P$ is a product of Abalone's local Jacobian J (cf. eq. 4.9) and the joint stroke ΔQ. Finally, $\Delta^A X$ can be written as

$$\Delta^A X = K \cdot \Delta^A L_P - \Delta^A X_{lost} = K \cdot (J \cdot \Delta Q) - \Delta^A X_{lost}. \qquad (4.12)$$

K is a matrix containing the cycle ratio θ and the impact factors κ given by

$$K = \frac{1}{1-\theta} \cdot \begin{bmatrix} \kappa_{trans} & 0 & 0 \\ 0 & \kappa_{trans} & 0 \\ 0 & 0 & \kappa_{rot} \end{bmatrix}, \quad \begin{aligned} \kappa_{trans} &= \frac{m_2}{m_1 + m_2} = 0.72 \\ \\ \kappa_{rot} &= \frac{I_2}{I_1 + I_2} = 0.81 \end{aligned}, \qquad (4.13)$$

where I_1 and I_2 are the moments of inertia about the z-axis of the body mass and the impact mass, respectively.

Actually, $\Delta^A X_{lost}$ is difficult to calculate for motions other than pure rotation or pure translation due to unmodeled effects such as non-ideal piezo actuators or the non-linearity of friction. Therefore, we propose a simplified method to evaluate $\Delta^A X$, which is presented in section 4.2.5.

In the following experiments Abalone's pose (x, y, φ_z) was measured with the computer vision system built into our nanorobot system (cf. section 2.4). The sensor resolution is 50 nm and the accuracy amounts to 250 nm. Translations and rotations were observed by tracking two objects mounted on Abalone's impact frame m_2. Notice that the pivot object did not necessarily coincide with the rotational center.

4.2.4 Calibration of Fine Motion

Abalone's kinematic parameters are mostly determined by the shape of its body, which was cut out of a bulk block by wire erosion. This fabrication process resulted in a very precise geometric Jacobian J (eq. 4.9), which was confirmed by finite element (FEM) analysis and speckle interferometry (cf. appendix C). Contrarily, the piezo actuators, used to convert the input voltage V into the joint displacement Q, are non-linear and subject to creep and ageing. They are the main sources of error in Abalone's model.

The transformation from the voltage V to the displacement ${}^A X$ can be written as

$$ {}^A X = J \cdot Q = J \cdot (\mathrm{diag}(D_p) \cdot V) = J_V \cdot V. \tag{4.14} $$

The fine motion Jacobian J_V is the product of the geometric Jacobian J and a diagonal matrix $\mathrm{diag}(D_P)$, which contains the piezo coefficients d_{Pi}, according to

$$ J_V = \frac{1}{3}\begin{bmatrix} 1 & 1 & -2 \\ -\sqrt{3} & \sqrt{3} & 0 \\ -1 & -1 & -1 \end{bmatrix} \cdot \begin{bmatrix} d_{P1} & 0 & 0 \\ 0 & d_{P2} & 0 \\ 0 & 0 & d_{P3} \end{bmatrix}. \tag{4.15} $$

Fitting the parameters d_{Pi} to a set of measurements yields the estimated values $\tilde{D}_P$ and $\tilde{J}_P$ given by

$$ \tilde{D}_P = \begin{bmatrix} 5.20 \\ 5.56 \\ 5.20 \end{bmatrix} 10^{-8}\,\mathrm{m/V} \quad \Rightarrow \quad \tilde{J}_V = \begin{bmatrix} 1.73 & 1.85 & -3.47 \\ -3.00 & 3.21 & 0 \\ -1.73 & -1.85 & 1.74 \end{bmatrix} 10^{-8}\,\mathrm{m/V}. \tag{4.16} $$

The value of $\tilde{D}_P$ agrees well with the data specified by the manufacturer (5.5 µm ±10 % at 100V).

4.2.5 Multi-DOF Inertial Motion

Abalone's rough motion behavior is investigated by measuring the displacements ΔX for different motions. According to the repeatability criterion of Buechi [BUECHI96], we ran the amplifier at an amplitude of $\Delta V = 50$ V instead of the maximum of 100 V. The stepping frequency and the cycle ratio were set to $f = 400$ Hz and $\theta = 0.1$, respectively.

Rough Motion Calibration

Movements of a length of 100 μm and a number of $n_{steps} = 97$ steps, were carried out in 12 different directions. To test the repeatability, the procedure was repeated 5 times. The goal positions which were regularly distributed on a circle with a radius $\rho = 100$ μm were blindly approached, i.e., without sensor feedback. The result is presented in fig. 4.11.
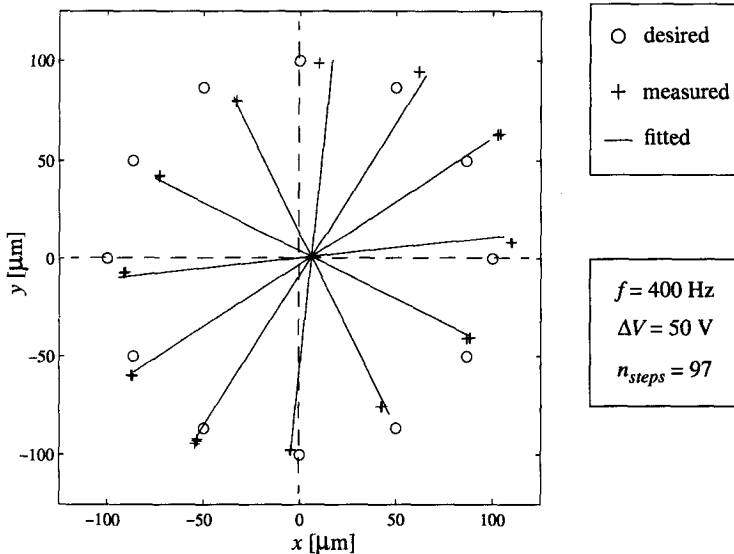

Fig. 4.11: *Performance test of Abalone's rough motion.*

There are two main deviations from the expected rotational-symmetric behavior:
- The circle of goals (fig. 4.11, desired) is deformed to an ellipse (fig. 4.11, measured). Similar to fine motion (cf. eq. 4.15), this effect originates from different piezo constants d_{P_i}. Therefore, we adjusted the rough motion

parameters of the actuators to the measurement. The updated model was used to calculate corrected goal positions relying on the same control signals V as before (fig. 4.11, fitted). The mean error between the updated goals, i.e., the calibrated model, and the measured positions is smaller than 7 % of the desired displacement.

- The significant translational offset pretends an asymmetric behavior of Abalone. To find the reason for this path following error, we turned Abalone by 180° around its z-axis. The same experiment before and after the rotation yielded a comparable length and direction of the offset motion with respect to the world system W. Our conclusion is, that external forces originating from an inclination of the tread or Abalone's wiring are the reason for this shift effect. This issue will be discussed below.

Correspondingly, for rotations we obtained a step size of 0.155 mrad ±3 % as well as a translational shift with the same direction as above.

Reduced Model for Rough Motion

Inertial drives are normally run with a constant step size $\|\Delta X\|$. Hence, it is adequate to calibrate them for a nominal step size Δx_{nom}. If the components of $\Delta^A X_{lost}$ are small compared to Δx_{nom}, it is possible to approximate $\Delta^A X$ (cf. eq. 4.12) with a single rough-motion Jacobian $J_{V, rough}$ according to

$$
\lim_{\|\Delta X_{lost}\| \to 0} \Delta^A X \approx K \cdot J \cdot \Delta Q = K \cdot J \cdot \mathrm{diag}(D_{P, rough}) \cdot \Delta V =
$$
$$
= J_{V, rough} \cdot \Delta V \qquad , \quad (4.17)
$$

where $D_{P,rough}$ contains the effective piezo parameters for rough motion. Fitted to the above experiments, the estimated value $\tilde{J}_{V, rough}$ for the rough Jacobian $J_{V, rough} = K \cdot J \cdot \mathrm{diag}(D_{P, rough})$ amounts to

$$
\tilde{J}_{V, rough} = \begin{bmatrix} 5.2 & 7.1 & -13.6 \\ 9.0 & 12.3 & 0 \\ 6.7 & 9.2 & 8.8 \end{bmatrix} \cdot 10^{-9} \mathrm{m/V} .
$$

The elements of $\tilde{J}_{V, rough}$ are by a factor of 2-3 smaller than the estimated fine motion Jacobian J_V (cf. eq. 4.16). The reason for this can be found in the impact factors κ (eq. 4.13), the piezo's non-linearity, and the non-zero ΔX_{lost}. Neverthe-

less, the reduced model yields an estimation of $\Delta^A X$ with a maximum error beyond 10%, which is sufficient for sensor guided or teleoperated positioning.

Repeatability

An important factor for feedback control is repeatability. A good repeatability of the plant leads to fast convergence, which is especially meaningful for controllers with a low control rate, caused, for example, by the slow information processing of vision data (cf. section 2.4).

We performed 50 uncalibrated displacements with a length of 100 µm in x-direction. The result, shown in fig. 4.12, is a standard deviation of $\sigma_x = 0.94$ µm and $\sigma_y = 0.72$ µm (~ 83 µrad) in radial and lateral direction, respectively. This is less than 1% of the desired displacement and corresponds to the error calculations based on variation of friction [BUECHI96].
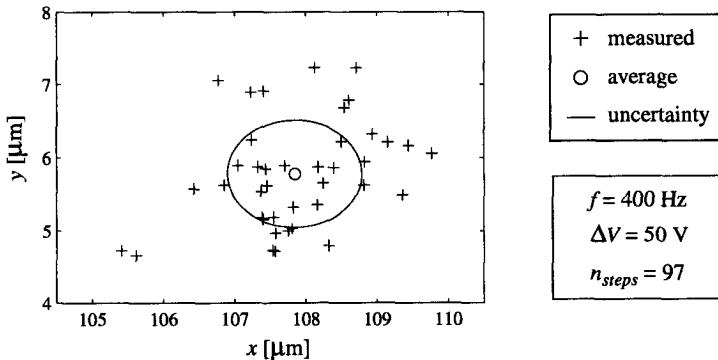
Fig. 4.12: *End position of 50 movements in x-direction*

Motion on Inclined Planes

During rough motion, Abalone is very sensitive to load forces. We investigated this characteristic by moving Abalone on an inclined plane.

Let the tread be tilted by an angle $-\beta$ about the y-axis. Abalone moves in the radial direction ρ, which spans an angle α with the x-axis (fig. 4.13). During the slip phases the inner platform m_1 is accelerated according to eq. 4.18. Notice that in the general case the direction of the acceleration $\ddot{x}_1$ is not parallel to the direction of motion e_ρ. Due to the constant value of the coefficient of friction μ_k (cf.
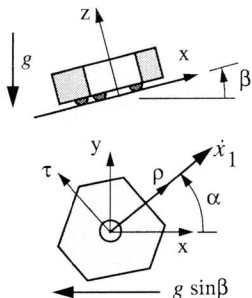
$$\ddot{x}_1 = -g \cdot \mu_k \cdot e_\rho - g \cdot \sin\beta \cdot e_x \quad (4.18)$$

e_ρ is a unit vector pointing in the actual direction of motion and e_x denotes the unit vector in x-direction.

Fig. 4.13: *Definition of the tilted setup*

appendix A), the period of slip after the fall-phase is prolonged due to the tread's inclination. This yields additional losses in both radial (e_ρ) *and* tangential (e_τ) direction. Thus, in contrast to the single-DOF case (cf. section 3.3.2), an external force not only changes the length of a step $\|\Delta X\|$, but it also leads to deviations from the desired direction of motion e_ρ.

In the experiment, Abalone performed five repetitions of displacements of 100 μm in the directions $\alpha = 0°$, $45°$, $90°$, $135°$, and $180°$ each. The results for tilt angles $\beta = \pm 1°$ ($\pm 20\%$) are compared to the horizontal case in fig. 4.14. In agree-
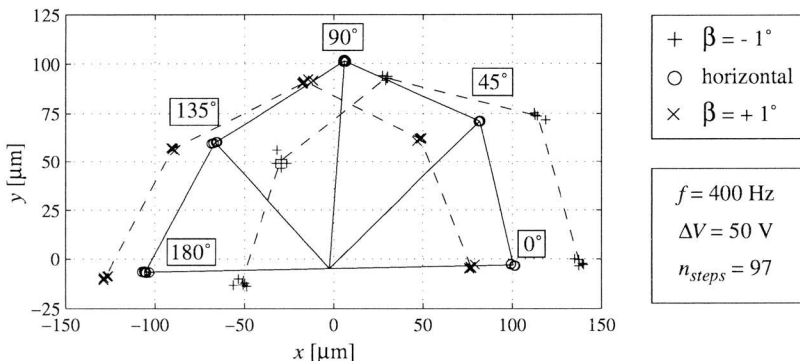

Fig. 4.14: *Rough motion on an inclined plane. Each displacement was performed from the origin (0/0) to the indicated goal position.*

ment with the theoretical analysis, we obtain a shift in ΔX of about -0.25 µm/° in the x-direction, i.e., 25% of the step size per degree. Also, the aforementioned crosstalk is confirmed qualitatively by a reduction of the y-components.

According to our model, the path following error due to the load sensitivity of multi-DOF inertial motion can be reduced as follows:

- External load forces and inclinations of the tread must be minimized.
- The frictional force $F_{\mu k}$ can be augmented, e.g by a larger preload F_N[4] or by increasing the coefficient of friction μ_k using specific materials.
- The mechanical model can be extended with a multi-DOF lost motion term, which incorporates a known or estimated load F_L.

Center Stability

If Abalone is rotated, the drift motion, observed in former experiments, as well as frictional variations cause significant deviations from the desired trajectory. To quantify this effect, we investigated the center stability during a full circular rotation. The result is presented in fig. 4.15. Notice that the tracked objects used as a reference for position and orientation do not coincide with Abalone's center.
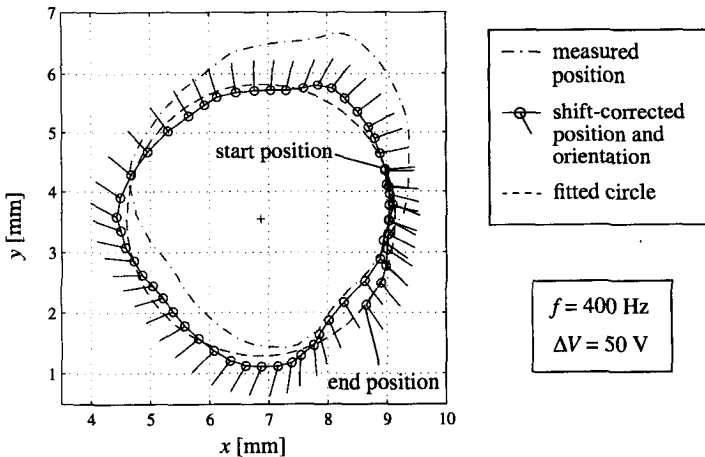

Fig. 4.15: *Position and orientation of an object fixed to Abalone's inertial frame during a 420°-rotation.*

---

4. which is currently the gravitational force.

There is a translational offset of about 1 mm after 360° of rotation which is about 1.5% of the distance travelled by the ruby contact points (78 mm). To obtain the shift-corrected path, we interpolated this offset from the start to the end and subtracted it from the measured data. Then, its maximum deviation from the fitted circle trajectory is less than 0.4 mm.

The main reason for this poor performance can be found in Abalone's geometry. Due to technical limitations the length of the actuator lever, $r = 8.7$ mm, and the diameter of the planar frictional joint (rubies) cannot be scaled down to the same extent as the typical displacements in micropositioning. Most of the "actuation energy" is required to rotate Abalone, whereas only a negligible part serves for translation. Thus, the positioning accuracy becomes rather poor if rotations are involved.

The center stability can be improved by the following means:
• sequentially performing rotations and translations
• redesign with a decreased distance of both the actuators and the legs from the rotational center
• feedback control of Abalone's position, eventually with on-line estimation of the model parameters [PAPPAS96].

4.2.6 Vibrations

Inertial drives produce significant vibration during rough motion sequences (cf. fig. 3.18), which can obstruct the manipulation task. In this section we investigate remedies to minimize these vibrations.

Abalone's Resonances

Fig. 4.16 presents the frequency response of Abalone resting on its ruby legs. The three resonances between 2 kHz and 2.5 kHz (1 to 3) can be approximated by out-of-plane vibrations of the almost rigid outer platform m_2. Conversely, the following modes (4, 5, and higher) are planar bending oscillations of exactly this frame.

If a cover is mounted on Abalone to form a working platform for microoperations, the resonances are lowered to frequencies beginning at about 1.2 kHz [ROMI97]. A detailed FEM analysis of the dynamic behavior as well as the experimental verification is presented in appendix C.
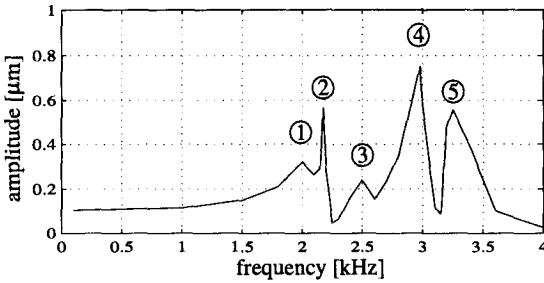
Fig. 4.16: *Frequency response of Abalone.*

Spectrum of the Input Signal

The input signal triangle(τ,θ), used to perform steps with the inertial principle, and its spectrum are shown in fig. 4.17. The Fourier coefficients are given by

$$\begin{bmatrix} a_n \\ b_n \end{bmatrix} = 2 \cdot \int\limits_0^1 u(\tau) \cdot \begin{bmatrix} \cos(2\pi n \cdot \tau) \\ \sin(2\pi n \cdot \tau) \end{bmatrix} d\tau, \quad u(\tau) = \frac{1}{2} \cdot \text{triangle}(\tau, \theta), \quad (4.19)$$

$$c_n = \sqrt{a_n^2 + b_n^2}, \quad (4.20)$$

where $\tau = t/T$ is the dimensionless time. Since the harmonics n fade out slowly with an exponent between -1 and -2, there is sufficient energy in the harmonics to

Fig. 4.17: *(a) Normalized triangle wave form and (b) its fourier-spectrum for $\theta = 0.1$.*

excite one or more of Abalone's weakly damped resonances. To allow for precise manipulations, the input signal has to be modified.

Modified Wave Form

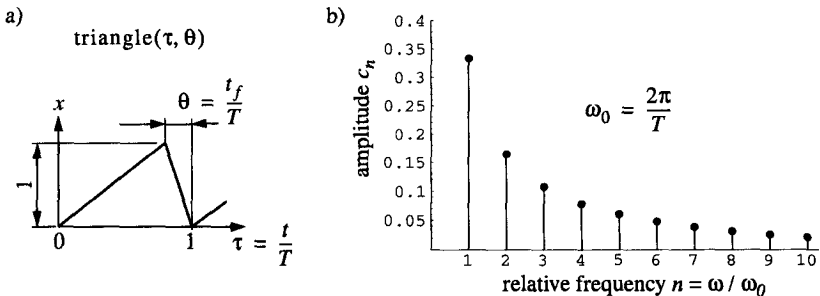Excessive vibration at Abalone's resonance frequencies can be avoided by cutting off the signal spectrum at a limit frequency f_{max}[5]. The modified signal is reconstructed from the first n_{max} harmonics according to

$$\text{trianlge}_{mod}(\tau) = \frac{1}{2} + \sum_{n=1}^{n_{max}} a_n \cos(2\pi n \cdot \tau) + b_n \sin(2\pi n \cdot \tau) \qquad (4.21)$$
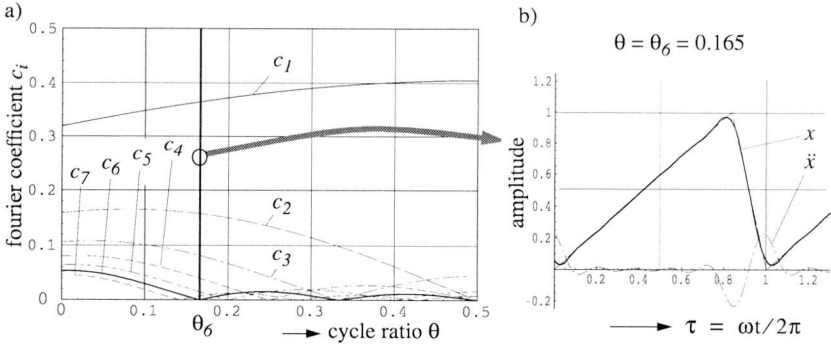
Fig. 4.18: *(a) Fourier coefficients $c_i(\theta)$ between pure saw tooth ($\theta = 0$) and symmetric triangle ($\theta = 0.5$), (b) modified triangle wave composed of the first 5 harmonics at $\theta = \theta_6 = 0.165$.*

According to fig. 4.18 (a), all Fourier coefficients c_n with $n \geq 2$ periodically become zero with growing cycle ratio θ. We benefit from this characteristic by selecting $n_{max} = 5$ and $\theta = \theta_6 = 0.165$ ($\Rightarrow c_6 = 0$). The result is the voltage signal drawn in fig. 4.18 (b).

Fig. 4.19 compares the result of inertial motion using the modified wave triangle$_{mod}(\tau)$ (b) to the original wave at $\theta = 0.05$ (a) at a frequency. With the modified

---

5. The spectrum has to be cut off below Abalone's first resonance f_1. Due to higher modes it is not sufficient to eliminate only a finite number of harmonics.

Fig. 4.19: *Influence of the bandwidth of the input signal, (a) triangle wave at θ = 0.05,(b) modified triangle composed of five harmonics at θ = 0.165, f = 200 Hz.*

signal, which was limited to a frequency of 1 kHz, we were able to eliminate the parasitic oscillation during the slip phase (2.5 kHz) almost completely. However, this method causes prolonged fall times t_f and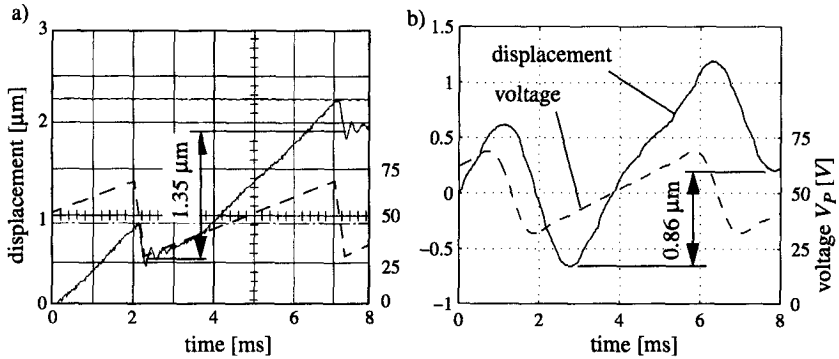 smaller peak accelerations. Consequently, Δx decreases from the original value of 1.35 μm to 0.86 μm. A beneficial side effect of this limited-bandwidth control is the reduced input power and thus the lower demands to the driver.

To conclude, the input wave form for inertial drives must be selected depending on the constraints of the task. If a high velocity is desired, one has to apply signals with a slope as steep as possible. On the other hand, for high precision motions, which do not tolerate excessive disturbances, it is advantageous to clip the input signal at the cost of lower rough motion speed.

4.2.7 Discussion of Abalone and its Applicability

Abalone possesses a large working range and an extremely high resolution. Due to its inherent stability and a repeatability of about 1% of the desired displacement it is able to approach a goal roughly without any sensor. However, for accurate positioning tasks feedback control is inevitable to eliminate errors originating from creep, hysteresis, frictional variations, and load effects. Abalone's stable characteristic allows for controlling with a slow sample rate. As an example, a high precision application using computational vision feedback is demonstrated in section 5.3.2

Global sensors, such as vision, are usually not fast and accurate enough to allow for positioning with nm-accuracy. A possible relief is to run Abalone as a servo drive, i.e., to add a local feedback loop based on additional joint or local sensors.

Abalone is preferably used as a horizontal 3-DOF table to position objects under a microscope (cf. section 5.2.2). To render 6-DOF manipulations possible, three out-of-plane DOFs (z, φ_x, φ_y) have to be added, as sketched in fig. 4.20. Such a spatial mechanism is presented in section 4.3.
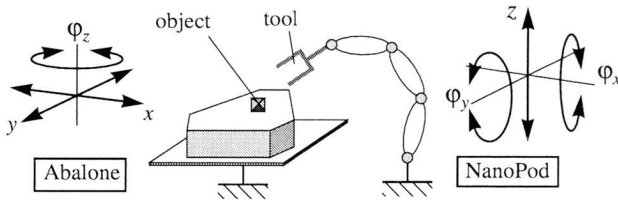
Fig. 4.20: *Distribution of DOFs*

4.3 NanoPod – A Flexible Spatial Platform

For operation under a light microscope a robot has to be small and must not impair the image acquisition. Various designs of micromanipulators with three or more DOFs are reported in the literature. Keller proposes a 3-DOF serial chain microrobot [KELLER96]. However, due to its compliancy it is not suitable for manipulations in the sub-micrometer range. Further, it requires extremely small fabricational tolerances. These drawbacks can be eliminated with parallel mechanisms, such as presented in [PERNETTE96][LEE89]. Mainly, they are tripod structures, as sketched in fig. 4.21, i.e., a reduced form of the Stewart platform [STEWART65]. Their handicap is the limited working range, originating from the use of both piezoelectric actuators and flexible joints.

To circumvent this restriction, we propose a new design, *NanoPod*[6]. It is a flexible parallel manipulator dedicated for micropositioning along the z-, φ_x-, and φ_y-direction (cf. fig. 4.20).

---

6. A parallel **nano**meter-resolution mechanism based on a tri**pod** structure.

Fig. 4.21: *Reduced 3-DOF Steward platform for out-of-plane motions, equipped with prismatic actuators (P) and spherical (S) and cylindrical (R) joints* [HUNT83].

4.3.1   Kinematics of NanoPod

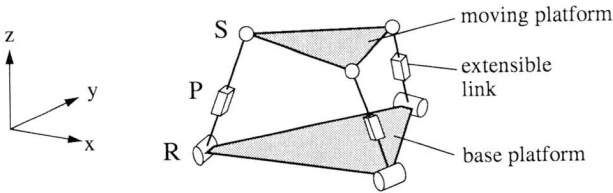To enlarge the working range of the above tripod mechanism (cf. fig. 4.21), we have changed the design as follows:

- The local joint deformation has been distributed over an extended region to allow for large displacements (cf. section 4.1.2). This has been realized by replacing the RPS (rotational-prismatic-spherical) drive trains with flexible beams.
- The piezo stacks (P) have been exchanged for large stroke actuators. In our prototype we used a serial arrangement of micrometer screws and piezo actuators. For future designs, crawling drives (cf. section 3.2) such as Inchworm motors [BURLEIGH95] could be employed.

The resulting design of *NanoPod* is outlined in fig. 4.22, whereas the principal structure is shown in fig. 4.23.

For the kinematic analysis, the flexible elements are considered as 6-DOF joints (3R3P) which store energy during elastic deformation. The number of DOFs is given by

$$n_{DOF} = 6n_B - \sum_{i=1}^{n_J} (6 - n_{DOFi}) = 6 - 3 \cdot (-1) = 9, \qquad (4.22)$$

i.e. all three actuators *and* the platform's six DOFs could be adjusted independently. Nevertheless, due to the elastic energy W_{el} stored in the beams there are six additional constraints, which represent the minimum of the potential energy:
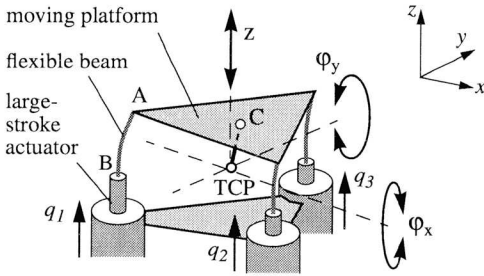
Fig. 4.22: *Basic design of NanoPod*
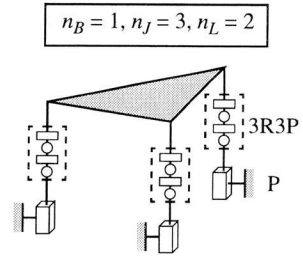
Fig. 4.23: *Kinematic configuration of Nanopod*

$$F_i = \frac{\partial W_{el}}{\partial x_i} \stackrel{!}{=} 0 \;, \quad i = 1 \dots 6. \tag{4.23}$$

Herein, F_i is a generalized force acting on the platform and x_i the platform's corresponding generalized coordinate (position or orientation). NanoPod can thus be considered a *3-DOF* mechanism with a *finite stiffness*. Due to geometric non-linearity and the parallel loop structure, it is difficult to calculate the platform's forward and inverse kinematics or its dynamic model analytically. That is why we derived a numerical model with FEM analysis, using the software package ANSYS[©] [ANSYS95].

The chosen approach of distributed flexibility yields new problems, which are investigated in the following:
- low natural frequencies due to reduced link stiffness
- vibration excitation originating from the stepping drives (cf. section 3.2)
- plastic deformation and creep in the flexible elements causing irreversibility, hysteresis, and fatigue.

4.3.2 Experimental setup

The test rig of NanoPod is shown in fig. 4.24. It consists of a platform carrying a marker at its tool center point (TCP) and three flexible beams [ANQUETIL97]. They are spring steel wires which are glued into holes in the platform. Each spring base can be moved in z-direction by a serial arrangement of a micrometer

stage for large motions and a piezo actuator for high resolution displacements. Additional micrometer screws are intended to adjust the geometry of NanoPod's base triangle in the x/y-plane. The dimensions are indicated in table 4.3.

DOF	z, φ_x, φ_y
transl. range	15 mm
rotational range	$\pm 25\,°$
resolution	2 nm /
	0.07 µrad
lateral stiffness k_x, k_y	376 N/m
first resonant freq.	27 Hz
platform diameter $2r$	64 mm
beam length l	20 mm
beam diameter d_B	0.3 mm
materials: platform	aluminum,
beams	spring steel

Tab. 4.3: *Data of NanoPod*
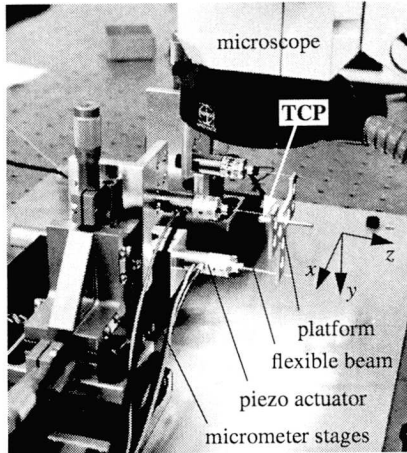
Fig. 4.24: *Prototype of NanoPod*

The TCP's pose is inferred using a light microscope. Since the employed 2D-vision system measures displacements perpendicular to the optical axis only, the whole mechanism was tilted by 90° with respect to the microscope. Hence, we were able to observe displacements along to the x, z, and φ_y-directions with a resolution of 100 nm. Due to NanoPod's threefold symmetry, we assumed its behavior to be homogenous in the x/y plane[7]. It was therefore sufficient, to examine the TCP motion in the axial (z) and radial (x and φ_y) directions.

4.3.3 Large Motions

Obviously, displacements in the z-direction are simple rigid body motions without any change in the geometry of the flexible structure. Such translations are trivial and limited by the actuators' stroke only. More interestingly, rotations about the x- and y-axes cause deformations in the beams.

---

7. This assumption was confirmed by FEM simulations

Lateral Shift

It is important to avoid radial displacements of the tool center point (TPC) as much as possible. This is motivated be the requirement to keep the end effector in the microscope's field of view. Several FEM simulations with different beam cross sections have been performed aimed at finding an optimum configuration. As a compromise between size, stiffness, and limitation of stress, we have selected 20 mm long cylindrical wires of a diameter of 0.3 mm [ANQUETIL97].
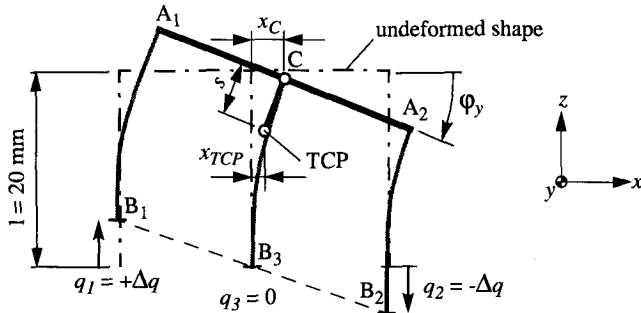
Fig. 4.25: *Diagram of large displacements* (φ_y).

In agreement with linear beam theory, the center C of the tilted platform performs a shift x_C in the lateral direction. According to fig. 4.25, the shift of points on the platform's axis of symmetry vary with their distance s from C. To find the optimum location for the TCP, i.e., the point with a minimum lateral displacement x_{TCP} in the entire working range, we have performed the following tilting experiment. The shift $x_{C,i}$ of C was measured for $i = 1...n$ tilting angles $\varphi_{y,i}$ ranging from -27° to +27°. Using the constraint

$$x_{TCP,i}(s) = x_{C,i} - s \cdot \sin\varphi_{y,i} \qquad (4.24)$$

we can formulate the quadratic error criterion of

$$E = var(x_{TCP}(s)) = \frac{1}{n} \cdot \sum_{i=1}^{n} (x_{TCP,i}(s) - \overline{x_{TCP}})^2 = \min \qquad (4.25)$$

$$\Rightarrow \frac{dE}{ds} \overset{!}{=} 0$$

with $\overline{x_{TCP}}$ the mean value of all TCP positions $x_{TCP,i}$. The result is an optimum of $s = 10.47$ mm, i.e., about half of the beam length l.

A comparison of FEM simulation and experiment using the optimized distance s[8] is presented in fig. 4.26. The qualitative results are in close agreement with each other. Interestingly, the real structure exhibits a smaller shift than the model in the simulation. The difference is firstly due to model inaccuracies, but also due to a significant lateral creep $\dot{x}_{TCP}$ (2 µm/min at $\varphi_y = 26°$). This effect, which originates from the visco-elastic behavior of the glue used to fix the wires, allows the platform to partially relax back to the center during the measurement. A possibility to reduce this creep is to clamp the wires mechanically on the platform without any polymer layer in between.
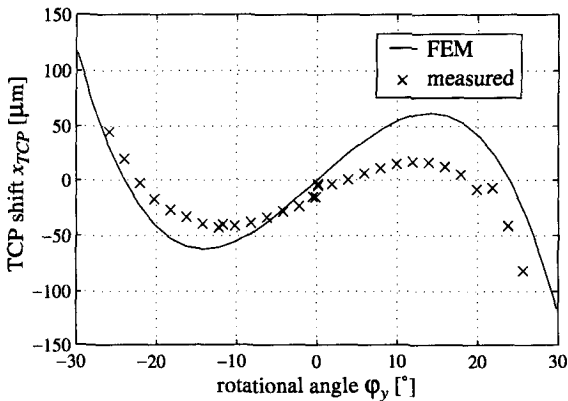
Fig. 4.26: *Lateral shift x_{TCP} of NanoPod's TCP due to rotations around the y-axis ($\varphi_x = 0$).*

To summarize, the TCP's maximum lateral shift within a working range of $\pm 30°$ is smaller than ± 100 µm, which is sufficient for operation under the light microscope. Large displacements are encountered at the border of the working range. A range reduction could therefore significantly improve the behavior, e.g. $|x_{TCP}| < 25$ µm at a range of $|\varphi_x, \varphi_y| < 22°$.

---

8. The optimization was performed independently for the FEM model and the experimental data and led to almost the same value for s.

Bending Stress

The platform's virtual center of rotation is situated approximately at a distance $s \approx l/2$ from the platform center C. According to eq. 4.4, this indicates almost a pure torque and hence, an equally distributed deformation along the flexible elements. The bending stress can be approximated by

$$\sigma_B = \frac{E}{2} \cdot \frac{d}{l} \cdot \varphi_y. \qquad (4.26)$$

For a tilt angle of $\varphi_y = 20°$ this yields a value of 450 N/mm^2, as can be observed for beam 3 in fig. 4.27.
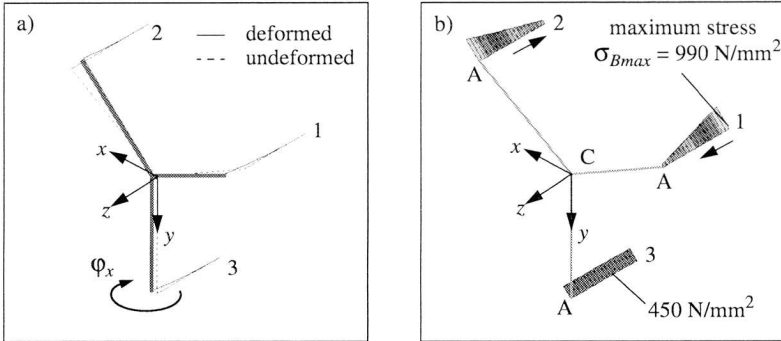
Fig. 4.27: *Excitation of $\varphi_y = 20°$, i.e. $Q = (+10.0, -10.0, 0)^T$ mm, (a) deformed shape, (b) bending stress along the beams*

Due to geometric non-linearity, the stress distribution in the beams 1 and 2 becomes highly uneven at large deflections, as fig. 4.27, (b) shows. At an displacement of 30° the FEM simulation indicates a theoretical maximum of 1400 N/mm^2, which is significantly higher than the elastic limit of spring steel (1000 N/mm^2 $\rightarrow \varepsilon_{elast} = 4.8\%$). Thus, to avoid plastic deformation, the rotational range has to be reduced or NanoPod's geometry is to be changed. This could be done with longer and/or thinner wires (cf. eq. 4.26). Nevertheless, the limit of this form of parameter tuning is given by the minimum stiffness required for micromanipulation.

4.3.4 Local Kinematics

For the design of a controller, the local kinematics and dynamics of NanoPod, i.e., Jacobian J, resonant frequencies, and stiffness of the mechanism, are of high importance.

Jacobian

The relation between the actuator displacement dQ and the deflection of the TCP dX depends on the actual position:

$$dX = J(\varphi_x, \varphi_y) \cdot dQ \quad , \quad dX = \begin{bmatrix} dz \\ r \cdot d\varphi_x \\ r \cdot d\varphi_y \end{bmatrix} \quad , \quad dQ = \begin{bmatrix} dq_1 \\ dq_2 \\ dq_3 \end{bmatrix}, \quad (4.27)$$

where $r = \overline{AC} = 32$ mm is the platform radius (cf. fig. 4.22). Due to geometric non-linearity $J(\varphi_x, \varphi_y)$ is difficult to calculate explicitly except for certain, well defined positions. E.g. in the undeformed shape ($\varphi_x, \varphi_y = 0$) it is given by

$$J(\varphi_x, \varphi_y)\Big|_{\varphi_x, \varphi_y = 0} = J_0 = \frac{1}{3} \cdot \begin{bmatrix} 1 & 1 & 1 \\ -1 & -1 & 2 \\ \sqrt{3} & -\sqrt{3} & 0 \end{bmatrix}. \quad (4.28)$$

The reader might have noticed the evident similarity to Abalone's Jacobian (cf. eq. 4.9), which is caused by the same triple-symmetry.

The non-linear change of $J(\varphi_x, \varphi_y)$ was evaluated numerically with FEM analysis and experimentally at NanoPod's prototype[9]. In table 4.4 we compare the results to the analytical model J_0 at two different positions. The elements of J vary less than 7% of the nominal value in the entire working range. This allows the implementation of a feedback controller with a time-invariant, *nominal Jacobian* J_{nom}. Alternatively, thanks to the smooth dependency on the structure's position, an inexpensive approximation model or an adaptive controller [PAPPAS96] is relatively trivial to implement.

---

9. Due to the measurement setup only z- and φ_x-displacements could be observed.

---

method	$\varphi_y = 0°$	$\varphi_y = 20°$
analytical	$\begin{bmatrix} 0.333 & 0.333 & 0.333 \\ -0.333 & -0.333 & 0.666 \\ 0.577 & -0.577 & 0 \end{bmatrix}$	–
FEM	$\begin{bmatrix} 0.333 & 0.333 & 0.333 \\ -0.333 & -0.333 & 0.666 \\ 0.577 & -0.577 & 0 \end{bmatrix}$	$\begin{bmatrix} 0.337 & 0.323 & 0.338 \\ -0.317 & -0.343 & 0.670 \\ 0.550 & 0.558 & 0.008 \end{bmatrix}$
measured	$\begin{bmatrix} 0.352 & 0.332 & 0.327 \\ - & - & - \\ 0.576 & 0.576 & 0.015 \end{bmatrix}$	$\begin{bmatrix} 0.360 & 0.312 & 0.329 \\ - & - & - \\ 0.550 & -0.573 & 0.013 \end{bmatrix}$

Tab. 4.4: *Comparison of NanoPod's Jacobian at two different positions ($\varphi_x = 0$).*

Frequency Response

The flexible beams, which carry the platform, are subject to lateral bending. Due to the resulting compliance along the corresponding directions (x, y, φ_z) Nano-Pod is susceptible to low frequency disturbances. Fig. 4.28 presents the response to a harmonic excitation, measured with a laser interferometer.

For lateral translation (x, y) and axial rotation (φ_z) we consider the deformation to take place in the flexible beams only, forcing them into an S-shape. Then, the structure's stiffness k_{trans} and k_{rot} can be approximated by

$$k_x = k_y = k_{trans} = 3 \cdot k_{beam} = 3 \cdot \frac{12 \cdot E \cdot I_B}{l^3} = 376 \text{ N/m}, \quad (4.29)$$

$$k_{\varphi_z} = k_{rot} = 3r^2 \cdot k_{beam} = 3r^2 \cdot \frac{12 \cdot E \cdot I_B}{l^3} = 0.393 \text{ Nm/rad}, \quad (4.30)$$

respectively, where E is the Young's modulus of steel ($2.1 \cdot 10^5$ N/mm^2) and I_B the beam's second moment of area. We obtain resonant frequencies of

$$f_1 = \frac{1}{2\pi} \cdot \sqrt{\frac{k_{trans}}{m_{platform}}} = 35.5 \text{ Hz} \qquad (4.31)$$

$$f_2 = \frac{1}{2\pi} \cdot \sqrt{\frac{k_{rot}}{I_{z,\,platform}}} = 52.7 \text{ Hz}, \qquad (4.32)$$

where $m_{platform}$ and $I_{z,platform}$ denote the platform's mass (7.55 10^{-3} kg) and its rotational inertia about the z-axis (3.59 10^{-6} kgm^2), respectively.
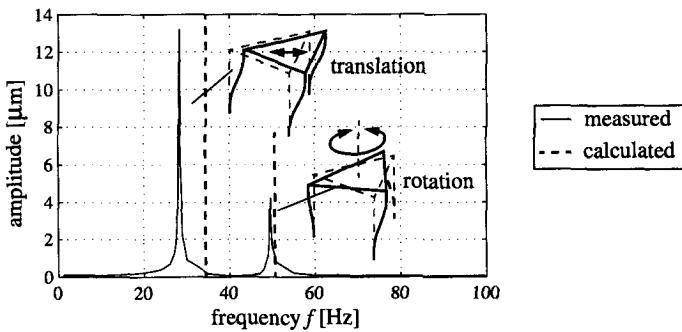
Fig. 4.28: *NanoPod's frequency response.*

The difference between calculation and experiment originates from unmodeled compliances (glue, actuators) and the simplified calculation, such as neglect of the beams' mass and the platform's asymmetrical geometry. Dynamic FEM analysis demonstrated a maximum variation of the first two natural frequencies of less than 15% in the entire workspace ($|\varphi_x, \varphi_y| \le 30°$).

At any rate, these frequencies are much too low for operation in the microscopic range. Firstly, the structure is likely to be excited by acoustic noise or electromagnetic fields (50 Hz!). Without any signal applied to the actuators, we measured a RMS noise of 26 nm in the TCP's x-coordinate during a period of one minute. Secondly, the low eigenfrequencies and the systems small damping yield long transient phases of the order of several hundred milliseconds.

One would in the first instant try to increase the stiffness k, and thus the resonant frequencies f_{res} by scaling the beams' dimensions d and l. From eq. 4.29 and eq. 4.30 follows that the stiffness k is proportional to

$$f_{res}^2 \propto k \propto \frac{I_B}{l^3} \propto \frac{d^4}{l^3}.$$ (4.33)

However, this strategy increases the actuator loads, too. They can be estimated by deriving the elastic energy W_{el} stored in the structure by the corresponding coordinate q_i according to

$$F_i = \frac{dW_{el}}{dq_i} = \frac{d}{dq_i}\left(\frac{1}{2}\sum_{j=1}^{3}\int_0^l EI_B \cdot \rho_j^2(\xi) \cdot d\xi\right) \propto \frac{d^4}{l}.$$ (4.34)

where $\rho_j(\xi)$ is the bending radius of beam j at the location ξ. An upper limit to these forces is given by the actuators' limited power and strength. Thus, the potential of stiffness adaptation by means of geometric scaling is by far to small for the required magnitude of stiffening. A more promising approach is proposed in the following section.

4.3.5 Discussion and Possible Improvements

Compared to conventional manipulators, NanoPod's principal advantages are its simple structure and uncritical fabricational tolerances. By using 1-DOF crawling actuators and ordinary spring steel wires, we have built an inexpensive spatial micropositioning stage with a high 3D-resolution.

Limits of NanoPod

In the current configuration, Nanopod can be used as a $(z\varphi_x\varphi_y)$- stage with the following specifications:
- rotational range of $\pm 20°$, determined by the elastic limit of the beams
- lateral shift of $\pm 25\,\mu m$ within the above working range, 100 μm at $\pm 30°$
- lateral and axial stiffness of 376 N/m and 0.393 Nm/rad, respectively
- first resonant frequencies of the order of 30 Hz.

To meet the requirements for the NanoRobot (cf. section 2.4), the platform's static and dynamic stability has to be augmented significantly.

Improved design - NanoPod II

NanoPod's lower vibrational modes are lateral oscillation of the rigid platform (x, y, φ_z), i.e., perpendicular to the actuation space (z, φ_x, φ_y). The mechanism thus has to be stiffened by introducing an additional structure which is compliant in z-, φ_x-, and φ_y-direction, but stiff along the other DOFs. Such a support could be a slotted membrane or a set of additional beams. Our proposition – *NanoPod II* – is presented in fig. 4.29. Here, stiffening is realized by means of three tangential beams (2), similar to those used to transmit the actuators' displacement (1). In contrast to the first construction (cf. fig. 4.23), loads acting on the platform mainly generate tension and pressure in the six beams, whereas the desired displacements are still covered by bending deformation.
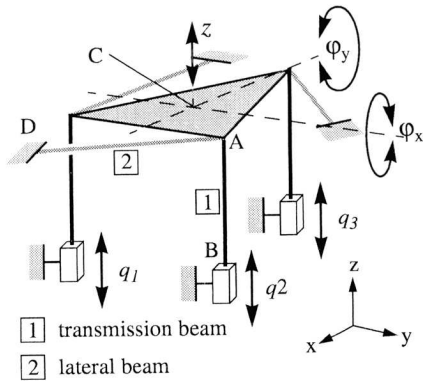
Fig. 4.29: *Design of NanoPod II, using additional flexible beams (2).*
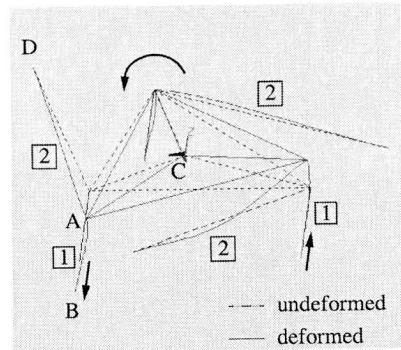
Fig. 4.30: *FEM simulation of Nano-Pod II's y-rotation.*

FEM simulations with lateral beams of diameter 0.3 mm and length 60 mm yielded a stiffness of $3.72 \cdot 10^5$ N/m and 583 Nm/rad in the radial and axial directions, respectively. The resulting resonant frequencies are located above 500 Hz, which significantly reduces the sensitivity to external excitations.

The stabilization with a laterally-stiff structure has the additional advantage of decreasing lateral shifts x_C of the platform center C. If the remaining error has to be reduced further, one or more bases of the lateral beams (fig. 4.29, D) could be articulated with additional actuators. With the help of a calibrated feed-forward model or sensor feedback, it should then be possible to keep the platform at its initial position or control it in six DOFs.

4.4 Summary of Multi-DOF Micromanipulation

In this chapter we presented two high resolution 3-DOF mechanisms relying on the stepping principle. Their major parameters are summarized in table 4.5.

feature	Abalone	NanoPod
DOFs	x, y, φ_z	z, φ_x, φ_y
workspace: translational rotational	20 mm 570° (wires!)	15 mm 20°
resolution: translational rotational	< 10 nm < 1.2 μrad	< 2 nm < 0.07 μrad
first resonant frequency	1.2 kHz	27 Hz
actuation, voltage	stack piezos, 100 V	Inchworms, 1000 V
size	$32 \times 38 \times 9$ mm^3	$\phi 64 \times 80$ mm^3

Tab. 4.5: *Comparison of 3-DOF stepping mechanisms*

Abalone is a planar, piezo-driven 3-DOF platform relying on the inertial principle. Due to its compact parallel design, it possesses high resonant frequencies and is therefore adequate for fast and accurate positioning tasks on horizontal planes. Abalone has a repeatability of better than 1% of the performed displacement and an extremely high local resolution in the nanometer domain.

Complementary to Abalone, **NanoPod** is a spatial mechanism, actuated by crawling drives. Based on a distributed-flexible structure, it provides a high 3D-resolution and a large workspace. For use under a light microscope, the configuration simply consists of three actuators, three flexible beams, and a rigid platform. If the mechanism has to work under a SEM, undesirable displacements could be compensated by additional actuators and beams.

The combination of these two multi-DOF mechanisms into a robot system with six relative DOFs will be discussed in the next chapter.

5 *System Integration*

Micromanipulation not only requires a robot able to perform spatial movements. There is also the need for tools to grip the parts as well as for devices that control the robot or provide an interface to the macro-world (cf. fig. 1.2). The cooperation of such instruments generates various constraints on the design of a micromanipulator. These aspects are discussed within the framework of the ETHZ-NanoRobotics project (cf. section 2.4).

As an experimental platform for all other members of the project, a prototype of a microrobot has been built. The micropositioning mechanisms investigated throughout section 2 to section 4 are used to form a multi-arm manipulator. Experiments demonstrate the performance of our micromanipulation system. Finally, a proposition for an improved future design is outlined.

5.1 Considerations on Handling of Microparts

The fundamental constraints determining the size as well as the kinematic configuration of a robot dedicated for microhandling arise from the microscope needed to observe the processes. Other important parameters are the tools' geometry and the kinematic requirements for basic handling operations, i.e., the *skills* necessary to deal with microparts.

5.1.1 Microscopic Environment[1]

This class of determinants can be divided into optical, geometrical and SEM-specific limitations (table 5.1).

	constraint	value	consequence
optical	field of view (FoV) much smaller than working range	LM: 0.9 x 0.7 mm^2 (at 66 ×), SEM: 20 x 20 μm^2 (at 10'000 ×)	both objects **and** tool(s) must be brought into the FoV, rotational axes should closely cross in one point
	short depth of field	< 100 μm	necessity to change plane of focus, i.e. **either** object **or** gripper is in focus
	visibility	20° stereo angle + 5° beam cones	no part of the robot allowed in the visibility cone during precise operations
geometrical	limited distance to objective lens	distance: 31 mm, diameter: 90 mm	small manipulator, limited x and/or y rotations
	limited space in the SEM's cavity	few dm^3	small and simple mechanism
SEM	electron beam	vacuum: 10^{-5} mbar, e$^-$-current: <200 μA	vacuum compat., no lubricants, small heat dissipation, low field emission (E, H)

Tab. 5.1: *Constraints to the manipulator originating from the microscope.*

As shown in fig. 5.1 the microscope has an extremely limited working volume i.e., a field of view (FoV) × depth of field, of $(700 \times 900) \times 100$ μm^3. Both the objects and the tools – which we from now on call "agents" – have to be visible during handling and assembly operations. Thus, the robot must be able to position them independently in the microscope's working volume. For example, each

---

1. If not explicitly mentioned, the light microscope's properties are addressed.

agent requires actuation along the z-direction to move into the microscope's narrow focal region, although one vertical DOF would be sufficient to adjust the distance between two agents. Therefore, a *redundant robot,* having more DOFs than the specified 5-6 DOFs for microhandling (cf. section 2.4), is needed.
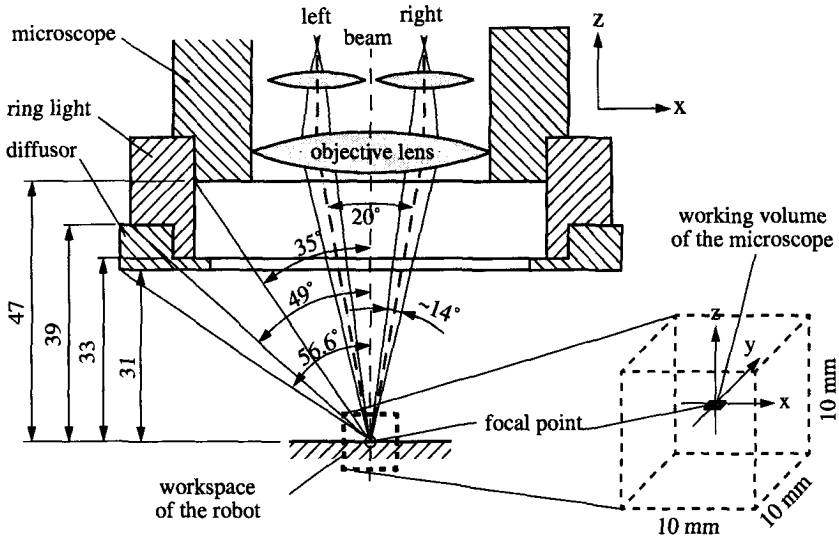
Fig. 5.1: *Cross section through the stereo light microscope (Zeiss SV 11) showing the space available for the robot's operation and the relationship between workspace and sensing region.*

5.1.2 The Robot's Tools

For handling particles of different size and shape and to allow for hand-in-hand operation, two different tools have been integrated in the nanorobot. Both of them rely on contact gripping, i.e., the target object is in mechanical contact with the tool during gripping.

Tweezer [GREITMANN95]

The tweezer consists of a bimorph actuator finger and a piezoresistive sensor finger with a length of 1500 μm and a thickness of 10 μm each. It is thermally actuated and can grasp objects with clamping forces of up to several mN. Since it is

able to transmit torques and thus, allows us to rotate the grasped objects in a manipulation system, the corresponding manipulator arm should be equipped with one or two orientational DOFs. However, due to shading of the microparts by the tweezer, the useful range of rotation is limited to less than 90°.

Vacuum Tool [ZESCH97]

Micro sucking tools normally consist of glass pipettes pulled from mm-sized glass tubes. Diameters of fractions of a micrometer can be achieved, depending on the task. Pipettes grasp the workpiece from one side only and thus, are well suited to operate at locations difficult to access such as grooves or holes. The simplicity in adjusting the active gripping area by the fabrication process facilitates an adaptation to the particle size. A major drawback, however, is the non-compatibility with the SEM environment (vacuum). Also, the capacity in transmitting torques is limited, which results in reduced clamping stability.

To adjust the micropart's orientation, the tools have to be rotated with respect to the object table. At the same time, the object's position must not be changed, or at least has to be kept within the microscope's FoV. As a consequence, all rotational axes of the robot should intersect more or less precisely at this fixed spot[2]. This characteristic can be realized with mechanical means (cf. section 3.3.3) or by compensating the translational shift with sensor feedback.

5.1.3   Skills Required for Microhandling

By microhandling we mean *pick-and-place* operations at arbitrary positions and orientations as well as *assembly* operations, which require application of forces.

For picking a target object, the tool has to approach this object close enough to grasp it and then to lift it from the substrate (cf. fig. 5.2, a). During the transport phases loss of parts is avoided by maintaining the gripping force (cf. fig. 5.2,b). However, for small particles (< 100 μm) the adhesion between gripper and object is usually sufficient to guarantee stable holding. The most difficult sub-task is the deposition [FEARING95B]. Small objects can only be released from the gripper thanks to the adhesion force between object and substrate or by stripping them off at an edge (cf. fig. 5.2, c). During picking (a) and placing (c), the manipulator has to perform short, but precise movements, whereas in phase (b) the accuracy is

---

2. which obviously has to coincide with the microscope's point of focus.

less crucial than the ability to transport and orient the objects over long distances. Also, phase (b) does not demand full visibility to the object.
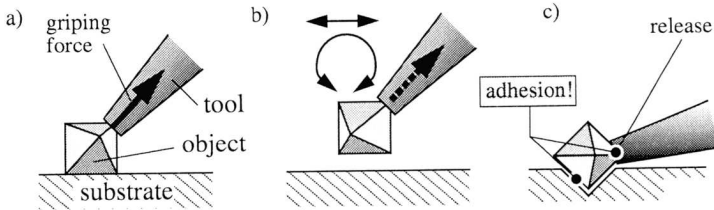

Fig. 5.2: *Basic skills for pick-and-place operations: a) pick, b) hold and transport, c) place.*

During assembly operations, the tool has to hold microparts robustly and has to apply forces necessary for the process. The robot arm carrying the tool must be stiff enough to tackle stiction and adhesion forces between the microparts.

5.2 Kinematic Layout of the Robot

5.2.1 Multi-Arm Configuration

The most intuitive way to perform spatial handling operations is to use a 6-DOF manipulator. However, this approach causes complicated mechanisms with long and compliant actuator chains. A different approach is to split the robot into separate arms each of them bearing its individual DOFs. If designed correctly, a tool mounted on one arm – the *tool carrier* – can be moved arbitrarily, i.e. in 6 DOFs, relative to a workpiece attached to the other arm – the *object carrier.*

The following rules determine the distribution of DOFs:
- To obtain a compact design, it is advisable to split the rotational DOFs, i.e. not to concentrate them in one arm.
- For redundant axes, only one of them needs high mechanical resolution.
- Translational shifts which exceed the dimensions of the FoV must be compensated by additional actuators of the same arm to maintain visibility of the corresponding agent[3].

3. This item becomes important for the extremely small FoV at high magnifications of the microscope (SEM: 20 x 20 μm at $10'000 \times$).

- Due to the short focal length, i.e., the limited space under the microscope, large tilt angles φ_x, φ_y are difficult to obtain. To tilt more than 45°, both arms involved have to perform part of the rotation.

Together with the constraints given from the microscope (section 5.1.1) these consideration lead to a distribution of DOFs shown in table 5.2.

	task	DOF	range	resolution
object carrier	planar positioning objects	x, y	10 mm	10 nm
	focusing	z	10 mm	10 μm
	orientation of objects	φ_z	360°	0.1°
	tilting of objects	φ_x	45-90°	0.1°
tool carrier(s)	vertical motion, focusing	z	10 mm	10 μm
	removal from the FoV	x or y	10 mm	10 μm
	drift compensation (if needed)	x, y	1-2 mm	10 μm
	orientation of tool(s)	φ_y , (φ_x)	45-90°	0.1°

Tab. 5.2: *Specifications for the robot's arms.*

5.2.2 Prototype of the Nanorobot

The need for two different tools and the multi-arm approach directly leads to the following manipulator configuration with three arms:

- As the central element of the *object carrier*, Abalone (cf. section 4.2) serves as a planar positioning table. It is lifted up and down by a commercially available micrometer stage [NEWPORT95] and carries TableCrab to tilt the objects (cf. section 3.3.3).
- The *gripper* is mounted on a y/z-stage and can be rotated around a horizontal axis by NanoCrab (cf. section 3.3.3).
- A third micrometer stage moves the *pipette* in x and z direction.

Fig. 5.3 presents a photo of the nanorobot's prototype and also specifies its principal parameters.

object carrier (Abalone)
  x, y: ...15 mm / 10 nm
  z: .....25 mm / 1 µm
  φ_z: ....360° / 1 µrad
  φ_x: ....±40° / 0.3 µrad

gripper arm
  x, z: ...13 mm / 1µm
  φ_y: ....360° / 0.1 µrad

pipette arm
  y, z: .. 25 mm / 1 µm

range / resolution
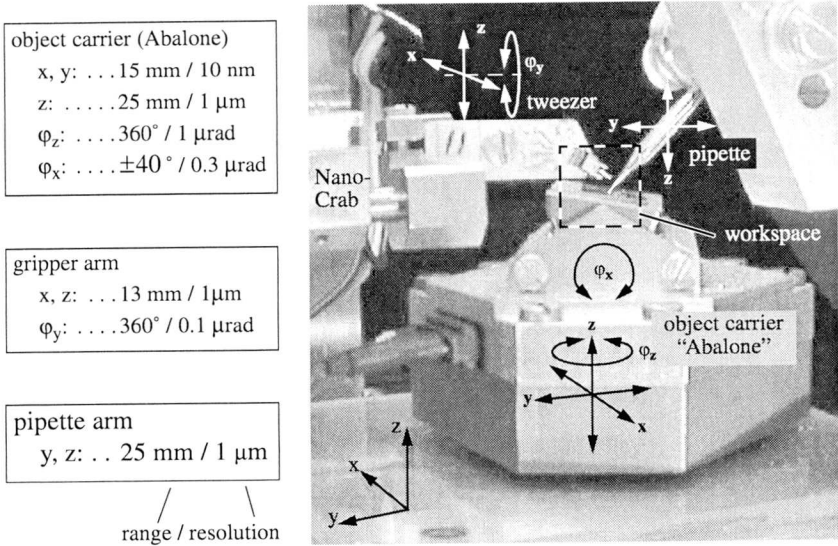
Fig. 5.3: *Close up view of the nanorobot prototype showing the manipulator's main elements and the corresponding DOFs.*

5.2.3 Kinematic Model

To design the controller, the kinematic model of the robot, particularly its Jacobian, has to be known. Fig. 5.4 sketches the geometrical relationships. The joint parameters q_i of the model are indicated in table 5.3.

DOFs	objects	gripper	pipette
translation	$x_A(t), y_A(t), z_A(t)$	$x_G(t), z_G(t)$	$y_P(t), z_P(t)$
rotation	$\varphi_A(t), \varphi_T(t)$	$\varphi_G(t)$	–

Tab. 5.3: *Actuated joint parameters*

Fig. 5.4: *Relationship of different arm coordinate systems (Abalone A, Gripper G, Pipette P) to the base frame W.*
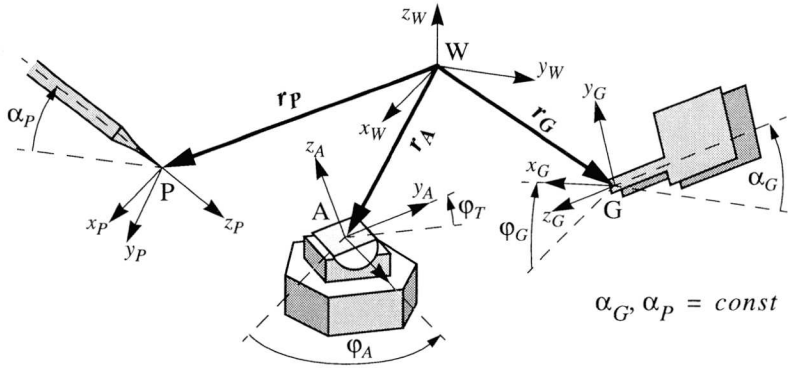
The homogenous transformation [CRAIG89] $^W_A T$ mapping the object carrier base A into the world coordinate system W (fig. 5.4) is calculated according to eq. 5.1:

$$^W_A T = \text{Trans}[r_A] \cdot \text{Rot}[z_W, \varphi_A] \cdot \text{Rot}[x_A, \varphi_T] =$$

$$= \begin{bmatrix} c_A & -s_A c_T & -s_A s_T & r_{Ax} \\ s_A & c_A c_T & -c_A s_T & r_{Ay} \\ 0 & s_T & c_T & r_{Az} \\ 0 & 0 & 0 & 1 \end{bmatrix} \quad , \quad (5.1)$$

where $r_A = (r_{Ax}, r_{Ay}, r_{Az})^T$ is the A-system's time-variant distance from the global origin W and $c_A = \cos(\varphi_A)$, $s_A = \sin(\varphi_A)$, $c_T = \cos(\varphi_T)$, etc. Analogously, the transformations for the frames G and P are given by eq. 5.2 and eq. 5.3, respectively, with $c_G = \cos(\varphi_G)$, $c_{\alpha G} = \cos(\alpha_G)$, $c_{\alpha P} = \cos(\alpha_P)$, etc.

$$
{}^W_G T = \text{Trans}[r_G] \cdot \text{Rot}[y_W, -\varphi_G] \cdot \text{Rot}\left[x_G, \alpha_G + \frac{\pi}{2}\right] =
$$

$$
= \begin{bmatrix}
c_G & -s_G c_{\alpha G} & s_G s_{\alpha G} & r_{Gx} \\
0 & s_{\alpha G} & -c_{\alpha G} & r_{Gy} \\
s_G & c_G c_{\alpha G} & -c_G s_{\alpha G} & r_{Gz} \\
0 & 0 & 0 & 1
\end{bmatrix}
\tag{5.2}
$$

$$
{}^W_P T = \text{Trans}[r_P] \cdot \text{Rot}\left[x_P, -\left(\alpha_P + \frac{\pi}{2}\right)\right] =
$$

$$
= \begin{bmatrix}
1 & 0 & 0 & r_{Px} \\
0 & -s_{\alpha P} & c_{\alpha P} & r_{Py} \\
0 & -c_{\alpha P} & -s_{\alpha P} & r_{Pz} \\
0 & 0 & 0 & 1
\end{bmatrix}
\tag{5.3}
$$

Relative to the tools, the position of the object to be handled can then be calculated by using the transformation sequences

$$
{}^G_A T = {}^W_G T^{-1} \cdot {}^W_A T \quad \text{(gripper, 6 DOFs)}
\tag{5.4}
$$

$$
{}^P_A T = {}^W_P T^{-1} \cdot {}^W_A T \quad \text{(pipette, 5 DOFs).}
\tag{5.5}
$$

For hand-in-hand operations the pipette has to be moved relative to the gripper (4 DOFs) according to

$$
{}^G_P T = {}^W_G T^{-1} \cdot {}^W_P T .
\tag{5.6}
$$

Based on these transformations, the different Jacobians can easily be obtained according to [CRAIG89]. In this 3-arm configuration, singularities are encountered only at $\varphi_A = 90°$ for the system "object-gripper" $(A \to G)$. The degree of redundancy is 2 for $A \to G$ (x, z) and $A \to P$ (y, z), and 1 between the tools themselves (z).

5.3 Experiments and Benchmark Tests

5.3.1 Microhandling Operations

The performance of our system has been demonstrated with several microoperations. Fig. 5.5 (a) shows the results of 2D and 3D *pick-and-place* operations teleoperated via the user interface (cf. fig. 2.2, teleoperation loop). Pyramidal and planar structures consisting of metallic balls with a diameter of 200 µm were assembled on a flat silicon substrate.
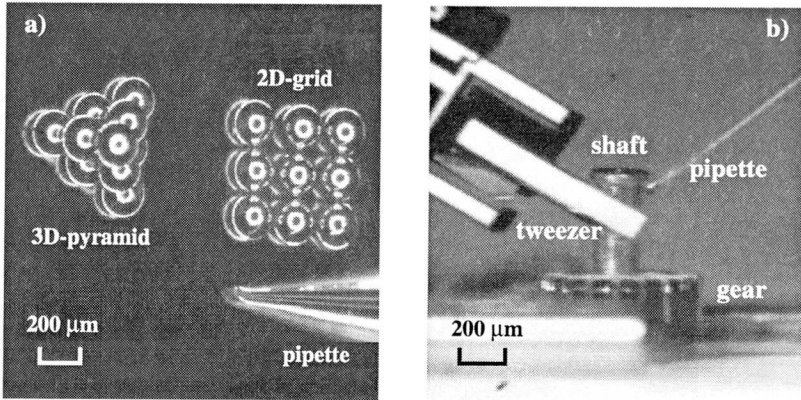

Fig. 5.5: *Benchmark tests: (a) 2D (grid) and 3D (pyramidal) structures assembled with metallic balls, (b) assembly of a planetary gear using hand-in-hand operation between tweezer and pipette.*

The robot is also able to perform *hand-in-hand* operations, i.e., to use its tools simultaneously in order to solve complex handling tasks. Examples are large rotations, grasping from a side that is not accessible in one attempt or increasing the handling force. Such an application is shown in fig. 5.5 (b): A 200 µm-diameter shaft of a planetary gear was orientated with the help of both tweezer and pipette. Subsequently, the axle was inserted into its seat. Except for pressing the bearing's cap into its seat, which requires high forces, all assembly steps could be executed successfully with the nanorobot. Similarly, we assembled a micro ball bearing and mounted a 80 µm-sized glass sphere on top of an AFM cantilever, which was required to measure large-area adhesion forces [VOEGELI97].

On even substrates the accuracy of contact manipulations is limited to about 10 μm, which is mainly determined by sticking problems during the place sequence (cf. section 5.1.3). Due to the significant adhesion at the contact between tool and object [FEARING95B], it is extremely difficult to release the objects exactly at the desired location. Given an ideal tool, i.e., without adhesion, the operator would be able to place microparts with an accuracy of about 2 μm, which is motivated by the diffraction limit of the employed microscope.

5.3.2 Sensor Guided Positioning

The aforementioned lower boundary for accuracy in teleoperation (2 μm) is far poorer than the resolution of the manipulator (< 10 nm). However, we can take full advantage of the mechanical resolution by directly measuring the robot's position using computational vision (cf. section 2.4).
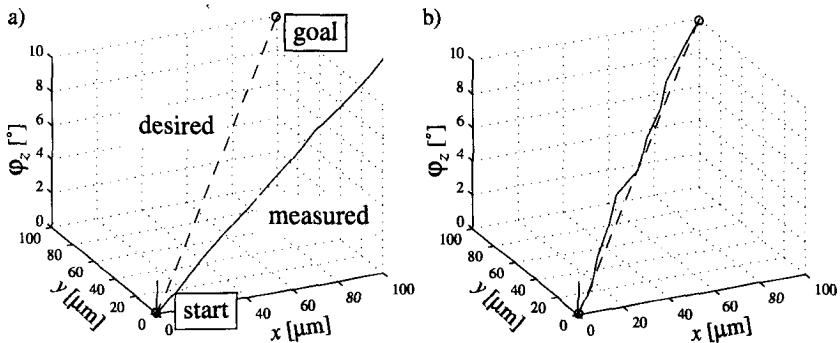
Fig. 5.6: $xy\varphi_z$-trajectories of the nanorobot: (a) open loop with inaccurate starting position and orientation, (b) closed loop control using visual feedback (from [PAPPAS97]).

Fig. 5.6 presents a test trajectory executed with Abalone. In open loop mode we notice a large deviation from the desired path (a). The error contains a systematic part due to inaccurate knowledge of the system and a random part. As soon as the adaptive vision feedback loop is closed (cf. fig. 2.2, automation loop), the systematic part is compensated depending on the specified value for the path following error (b). If this tolerance is reduced at the end of the motion, Abalone is able to meet the goal position with an accuracy better than 50 nm [PAPPAS97]. Laser interferometrical tests with one DOF yielded a closed loop accuracy even better than 10 nm [BUECHI96].

5.4 Proposal of an Improved Design

Although the microscopic constraints (cf. table 5.1) are satisfied, the prototype configuration is not optimal due to the following shortcomings
- Changing the microscope's plane of focus requires the actuation of two (or more) DOFs, which detrimentally affects the tool-object relation.
- The objects can be positioned relative to the tool (pipette) in 5 DOFs only.
- The micrometer stages limit the resolution in the z-direction to 1 µm.
- The nanorobot is not SEM compatible due to the large micrometer stages and the magnetic field emission of the DC-motors

Because of these problems we propose an improved design, as sketched in fig. 5.7. Here, the emphasis is laid on an optimal one-tool operation rather than on a multiple-tool environment

The main modification compared to the first setup (cf. section 5.2.2) is the introduction of an *adjustment stage*, on top of which the actual *micromanipulator* is mounted. It allows one to change the visible region of the workspace without affecting the object-tool relation. This additional xyz-stage only serves for observation purposes (cf. optical constraints, table 5.1), but not to perform precise movements. Thus, a resolution of about 10 µm is sufficient. This can be realized, for example, by using cheap micrometer drives.

The large, slow, and low-resolution micrometer-driven tool carriers in the manipulator are exchanged for *NanoPod* (section 4.3) which is driven by three Inchworm motors [BURLEIGH95]. The result is a mechanism able to move the tool relative to the microparts lying on top of *Abalone / TableCrab* (cf. section 4.2 & section 3.3.3) arbitrarily in 6 DOF with nm/µrad-resolution. Since the rotational range of each single joint is restricted to 20-40°, we have chosen a redundant setup with a large stroke consisting of NanoPod and TableCrab. If an even wider tilt range is required, a supplementary 360°-axis, e.g. NanoCrab (cf. section 3.3.3), could be mounted between the mobile platform of NanoPod and the tool.

In addition to the increased flexibility, this design is much smaller and more compact compared to the first one. If the adjustment stage is actuated by non-electromagnetic drives such as ultrasonic motors, it is possible to run the nanorobot inside an SEM.
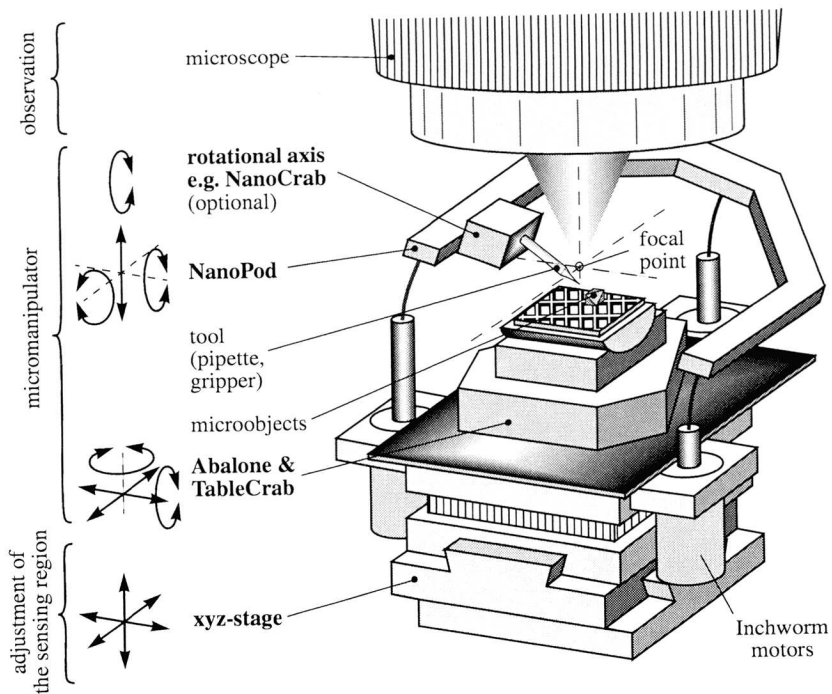
Fig. 5.7: *Sketch of the improved nanorobot design.*

5.5 Summary

In this chapter we discussed the combination of mechanisms presented earlier in section 3 and section 4 to a manipulator with 6 DOFs. Design rules satisfying the micromanipulation constraints were elaborated in order to render a systematic development of powerful mechanisms possible. In a prototype configuration, Abalone, TableCrab, NanoCrab, and additional micrometer screw drives formed a nanorobot system working under a stereo light microscope. We demonstrated the possibility of performing operations, such as pick-and-place and assembly tasks. Using vision feedback we were able to control the robot's position with an accuracy better than 50 nm.

Having learned from the drawbacks of the first design, we proposed a manipulator with an improved kinematic structure dedicated to 6-DOF microoperations in an SEM environment.

6 *Conclusions*

Previous research has shown, how important dealing with microparts is and will be in engineering, biology or medicine. In the treatment of particles, a crucial task is positioning. Special tools which allow a suitable interaction with the microworld are required. The aim of this thesis is therefore to develop compact and reliable mechanisms which are able to perform basic positioning tasks. The actual work must be considered as an integral part of the Nanorobotics project at the ETH Zurich (cf. section 2.4) and is thus strongly connected to the research of the partners.

6.1 Contributions

Different problems had to be solved during the design of a sophisticated microrobot. The principal contributions are outlined in the following section. Their interconnections to each other are displayed graphically in fig. 6.1.

6.1.1 Actuation Principles

We have selected piezo-driven stepping principles for the actuation of the microrobot (fig. 6.1, 1) due to mechanical simplicity and a large ratio between working range and resolution. For both the crawling and the inertial principle, a mathematical model was derived, which relied on rigid bodies and elastic actuators.
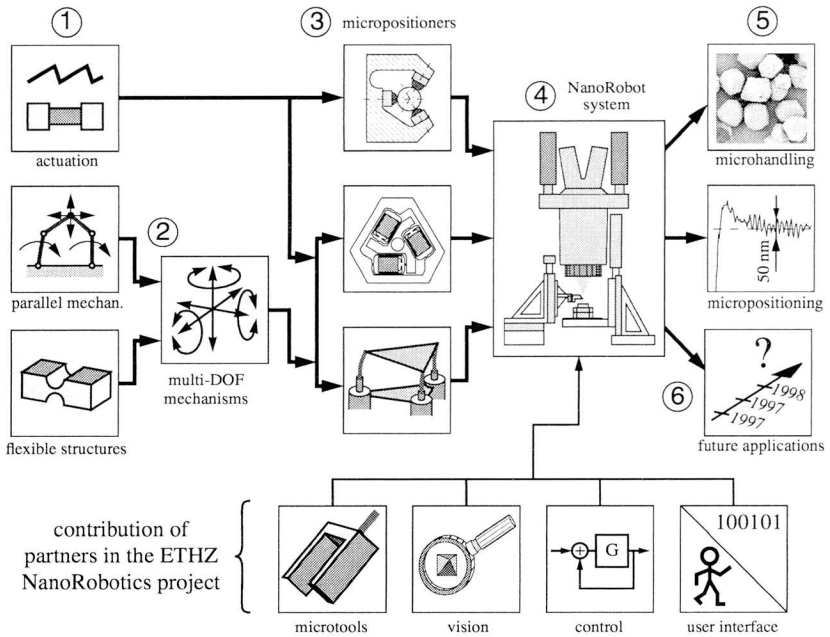
Fig. 6.1: *Contributions of this work to micromanipulation*

Based on these, the mechanisms and their control algorithms were optimized for repeatability, load capacity and dynamic response. Experiments proved the feasibility of our approach and demonstrated the potential of stepping drives for micropositioning. The contributions of this part can be summarized as follows:

Crawling Drive

- We found the optimum stepping frequency which yields a maximum rough positioning velocity. However, if high repeatability is the main goal, the crawler has to be driven at a reduced rate.
- There is an optimum clamping force, which has to be adjusted according to the load force and the desired stepping frequency.
- Despite the presence of static friction, it was possible to control the position with an accuracy better than 10 nm in fine positioning mode. By dividing the motion in a stepping phase, a local mode, and a special switching sequence,

we were able to continuously expand this accuracy over a – theoretically – infinite workspace.

Inertial Drive

- We derived a generalized model for the stepping behavior of the inertial drive which considers the influences of elasticity, friction, arbitrary loads, and preload forces, as well as amplitude, shape, and frequency of the input signal.
- An important result of this model is the explicit formulation of an optimum frictional force. Using this approach, it is possible to adjust the preloading force to a wide range of load forces.
- The effect of elasticity on the drive's performance was quantified and used to define a lower limit for the driving voltage.
- The usefulness of the stick-slip principle, a special case of the inertial drive, was demonstrated for a rotational motor. As well as a high resolution, this motor also has an extremely small runout.

Although, the stepping drives investigated in this thesis are highly sensitive to external forces, they are capable of positioning "heavy" loads extremely accurate if sensor feedback is employed.

6.1.2 Multi-DOF Mechanisms

Due to the drawbacks of conventional robot structures, i.e. friction, play, and compliance we selected flexible parallel structures for the design of multi-DOF mechanisms (fig. 6.1, 2). Our contribution consists in the investigation of two complementary microstages with three DOFs: Abalone – a planar piezo-driven platform relying on the inertial principle, and *NanoPod* – a spatial mechanism with high resolution using crawling drives (fig. 6.1, 3).

Abalone

- Abalone can be positioned with good repeatability and a resolution in the nanometer range. Its working range is limited by the size of the – passive – tread only.
- It was shown that operating the inertial mechanism with a voltage wave form having a spectrum cut off below the first resonance frequency is able to reduce disturbing vibrations to a great extent. At the same time, inertial

motion was still possible, however with a reduced step size. FEM simulation and experiments indicated that the resonances begin at about 1.2 kHz.

- Abalone's performance, in particular the path following behavior, is highly sensitive to external loads, such as inclinations of the tread's surface. Further, off-center rotations show significant translational shifts and noise. Hence, high precision movements over long distances can be performed only with the help of sensor feedback.

NanoPod

- Thanks to the use of distributed flexible structures, NanoPod's working range is more than one order of magnitude larger than similar mechanisms using discrete flexible joints.
- Undesirable lateral displacements were minimized by geometrical optimization of the structure. Further improvement could be achieved with additional compensation actuators.
- The lack of static friction and the use of piezoelectric actuators rendered local 3D-positioning with nm-resolution possible.
- We proposed an additional lateral stiffening structure which augments the mechanism's low transversal stiffness.

6.1.3   Micromanipulation System

The knowledge gained during this work, as well as the results from the other partners in the project were used to design and build a prototype NanoRobot system (fig. 6.1, 4). In this context, our contribution is the design and implementation of the manipulator and the execution of basic experiments (fig. 6.1, 5).

Design

The stereo light microscope environment strongly determined the design of a first prototype of the nanorobot as follows:

- Due to the limited accessibility of the workspace, but also because of the lack of general purpose instruments, we integrated two different tools into the robot: A thermally actuated tweezer [GREITMANN95] and a vacuum tool based on a glass pipette [ZESCH97].
- The manipulator is a multi-arm setup containing an object carrier and two tool carriers.

- We equipped the robot with redundant actuation in order to satisfy the optical constraints given from the microscope.

Having learned from the insufficiencies of the first configuration in microhandling experiments, we proposed a manipulator with an improved kinematic structure. It is better adapted to the microscopic environment and should facilitate 6-DOF microoperation. Additionally, it is able to work under an electron microscope, since it utilizes only piezoelectric actuators and has a size of about 1 dm^3.

Experiments

We have demonstrated the possibility of performing teleoperative microhandling operations, such as pick-and-place and microassembly. Furthermore, a vision feedback controller has been implemented which allows for positioning of objects with an accuracy of about 50 nm [PAPPAS97]. With this system, we were able to automate specific tasks such as following a given spatial trajectory.

6.2 Outlook

It was not possible, of course, to solve all problems in the field of micropositioning within this thesis. Some of the potential extensions have already been discussed in the corresponding chapters. These are:

Stepping Principles and Mechanims

- The effect of different materials or surface roughness on the performance of stepping drives have been mentioned only briefly. It is expected, that an adaptation of the frictional contact properties could improve the performance of these mechanisms, e.g., the load capacity.
- Methods of active or passive damping could significantly reduce vibrations or accelerations. This can be of interest at particular locations such as the substrate which carries the microobjects or the tool tip.
- The cross talk between different DOFs in multi-directional stepping drives has to be investigated further. A better model should contribute to a reduced open-loop path following error, but also to a better closed-loop performance.
- As already mentioned by Büchi [BUECHI96], a local feedback loop, able to control the actuator's fine displacement at high speed and precisely, could improve the stepper's performance significantly.

Micromanipulation System

- For robust, user-friendly operation, the automation loop has to be closed for objects *and* tools. Depending on the task, additional joint sensors, e.g. at the piezo level, or local sensors, which measure contact forces or surface potentials, could be integrated. These sensors are also suitable to provide the human operator with additional information in the teleoperation mode.
- To achieve a better resolution of the global vision sensor, the manipulator has to work under a SEM. Our robot is well suited for that environment, i.e., it is compatible with vacuum conditions and does not impair the electron beam of the microscope. Also, it is small enough to fit into the cavity of a SEM.
- As a next step, simple tasks such as sensor guided grasping and placing, as well as primitive assembly tasks have to be automated. The fundamentals of hand-in-hand operation have to be studied for more complex skills. As a consequence, the interface has to be adapted to transmit the "higher" level commands specified by the operator.
- In addition to a microhandling system, further infrastructure, such as micropart suspenders, transportation devices, etc. are required to configure a fabrication line and to connect the microassembly stations to the macro world.

Further Applications (fig. 6.1, 6)

Apart from the primary goal of handling microobjects, single components of the robot are suitable to work under a high resolution microscope. Abalone, for instance, offers a compact design with short kinematic chains and is not difficult to control. It is an effective means for positioning objects under a SEM, either with teleoperation or computer vision feedback. Another perspective is the combination of Abalone with local probe microscopes to scan a large specimen in its entirety while at the same time retaining atomic resolution.

References

Publications

[AGRAIT91]   Agrait N., "Vertical inertial piezoelectric translation device for a scanning tunneling microscope", Rev. Sci. Instr., 63(1):263-264, Jan. 1992.

[ANSYS95]   ANSYS Workbook for Revision 5.2, Sept. 1995, ANSYS, Inc., 201 Johnson Road, Houston, PA, USA

[ARAI92]   Arai T., et al., "Micro hand module using parallel link mechanism", Proc. Japan/USA Symp. on Flexible Automation, vol 1, July 1992.

[ARMSTRONG91] Armstrong B., "Control of Machines with Friction", Kluwer Academic Publishers, 1991.

[ASAKAWA92]   Asakawa N., Takeushi Y., Shimizu H., Inada H., "Development of highly accurate rotational positioning device", IFToMM Int. Symp. of machines and Mechanisms, p 808-811, Sep 1992, Nagoya.

[AUER95]   Auer F., van Beek H.F., de Veer B., "A magnetically levitated, six degrees of freedom high accuracy positioning system", MAG95 Magn. Bear., Magn. Drives and Dry Gas Seals Conf., Aug. 1995, Alexandria, USA

[BAUMANN95]   Baumann D., "Hochauflösender Mechanismus zum Positionieren eines Rotors", Swiss Patent No. 1485/95-9, 1995.

[BAUER94]   Bauer A., Möller F., "Piezo actuator special design", Actuators 94, p 128-132, 1994, Bremen.

[BESOCKE86]   Besocke K., "An Easily Operable Scanning Tunneling Microscope", Surface Science, vol 181:145-153, 1987.

[BEXELL95]   Bexell M., Tiensuu A.L., et al., "Characterization of an inchworm prototype motor", Sensors and Actuators A, vol. 43:322-329, Nov. 1994.

[BINNIG82]   Binnig G., Rohrer H., Gerber C., Weibel E., "Surface studies by scanning tunneling microscopy", Phys. Rev. Lett., vol 49:57, 1982.

[BINNIG86]   Binnig G., Rohrer H., "Scanning tunneling Microscopy", Journ. of Research & Development, IBM, vol 30(4): 355-369, 1986.

[BLEULER94]   Bleuler H., et. al., Micromachined active magnetic bearings, 4th Int. Symp. on Magn. Bearings, p 349-352, Aug. 1994, Zürich, Switzerland.

[BREGUET95]   Breguet J.-M., Clavel R., Renaud P., "A 4 degrees of freedom microrobot with nanometer resolution", Institute de microtechnique, Lausanne, Switzerland.

[BROWN92]   Brown K.T., Flaming D.G., "Advanced Micropipette Techniques for Cell Physiology", 1992.

[BRUECK94]   Brück R., Hahn K., Stieneck J., "Technology description methods for LIGA processes", Journal of Micromechanics and Microengineering, v 5(2):196-198, June 1995.

[BUECHI95]   Büchi R., Zesch W., Siegwart R., "Inertial mechanisms for positioning microobjects: An analytical analysis", SPIE Conf. on Microrobots and Micromechanical Systems, p. 89-97, Oct. 1995, Philadelphia, USA.

[BUECHI96]   Büchi R., "Modellierung und Regelung von Impact Drives für Positionierungen im Nanometerbereich", Diss. ETH Nr. 11788, Aug. 1996, Zürich.

[BURLEIGH95]   Burleigh, "The Micropositioning Book", 1990, Burleigh Instruments, Inc., Fishers, NY, USA.

[CLAVEL88]   Clavel R., "DELTA, a fast robot with parallel geometry", Proc. Int. Symp. on Industrial Robots (ISIR 88), p 91-100, 1988.

[CODOUREY95]   Codourey A., Siegwart R., Zesch W., Büchi R., "A robot system for automated handling in micro-world", Conf. on Intel. Robot Systems, 1995, Pittsburgh.

[CODOUREY96]   Codourey A., Rodriguez M., Pappas I., "Human machine interaction for manipulations in the microworld", 5th IEEE Int. Workshop on Robot and Human Communication, Nov. 1996, Tsukuba, Japan

[CRAIG89]   Craig J., "Introduction to Robotics", Addison-Wesley Publishing Company, Inc, New York, 1989.

[CROMMIE93]   Crommie M.F., Lutz C.P., Eigler D.M., "Confinement of electrons to quantum corrals on a metal surface", Science, vol 262:218-220, Oct. 1993.

[DANUSER96A]   Danuser G., Mazza E., "Stereo light microscope calibration for 3D submicron vision", Proc. of the 18th ISPRS Mondial Congress, vol 31/B5:101-108, July 1996, Vienna, Austria.

[DANUSER96B]   Danuser G., Mazza E., "Observing deformations of 20 nanometer with a low numerical aperture microscope", Optical Inspection and Micromeasurements, SPIE vol 2782:180-191.

[DREXLER92]   Drexler K.E., "Nanosystems", John Wiley & Sons, New York, 1992.

[DUBBEL90]   Dubbel, "Taschenbuch für den Maschinenbau", 17. Auflage, Springer Verlag Berlin-Heidelberg, 1990, Germany.

[ELLIS62]   Ellis, G.W., "Piezoelectric Micromanipulators", Science, vol. 138:84-91, Oct. 1962.

[FATIKOW95]   Fatikow S., Magnussen B., Rembold U., "A piezoelectric mobile robot for handling of microobjects", Int. Symp. on Microsystems, Intelligent Materials and Robots, p 189-192, Sept. 27-29, 1995, Sendai, Japan.

[FEARING95A]   Fearing R.S., "A planar milli-robot system on air bearing", 7th Int. Symp. on Robotics Research, Oct. 1995, Herrsching, Germany.

[FEARING95B]   Fearing R.S., "Survey of Sticking Effects for Micro Parts Handling", IEEE/RSJ Conf. on Intell. Robots and Systems, vol 2:212-217, 1995, Pittsburgh, PA.

[FERREIRA96]   Ferreira A., Minotti P., Le Moal P., Ferniot J-C., "An integrated five-degrees of freedom piezoelectric micromanipulator", SPIE Symp. on Smart Structures and Materials, vol 2717:720-731, Febr. 1996, San Diego.

[FUJITA 89]   Fujita H., "Studies of micro actuators in Japan", IEEE Conf. on Robotics and Automation ICRA 89, p 1559-1564, 1989.

[FUKUDA91]   Fukuda T., Fujiyoshi M., Kosuge K., Arai F., "Electrostatic micro/nano manipulator with 6 d.o.f.", ASME Micromechanical Sensors, Actuators and Systems, vol 32:197-202, 1991.

[FUKUDA93]   Fukuda T., Arai F., "Microdevices and Micro Robotics", 2nd. Conf. on Mechatronics and Robotics, p 533-544, Sept. 1993, Duisburg/Moers, Germany.

[GARDNER91]   Gardner J.W., Hingle H.T., "From instrumentation to nanotechnology", Gordon and Breach Science Publishers S.A., Philadelphia.

[GHAZVINI96]   Ghazvini M., "Modellgestützte, mehrdimensionale, inverse Interpolation zur effizienten Verbesserung der Positionier- und Orientierungsgenauigkeit", Diss. ETH Nr. 11889, 1996, Zürich.

[GOSSELIN96]   Gosselin C.M.,Lemieux S., Merlet J.P., "A new architecture of planar three-degree-of-freedom parallel manipulator", IEEE Conf. on Robotics & Automation ICRA 96, p 3738-3743, 1996, Minneapolis.

[GREITMANN95]   Greitmann G., Buser R., "Tactile micro gripper for automated handling of microparts", Transducers 95 - Eurosensors IX, 8th Int. Conf. on Solid-State Sensors & Actuators, 1995, Stockholm, Sweden.

[HAGOOD88] Hagood N.W., et. al., "Development of integrated components for control of intelligent structures, smart materials, structures and mathematical issues", U.S. Army Res. Office Workshop, p 80-104, Sept. 1988, Blacksburg, USA.

[HAN89] Han C.-S., Tesar D., Traver A.E., "The optimum design of a 6 dof fully-parallel micromanipulator for enhanced robot accuracy, ASME Conf. Adv. in Design Automation, vol 19(3): 357-363, Sep. 1989, Montreal.

[HARA89] Hara A., Sugimoto K., "Synthesis of parallel micromanipulators", J. of Mechanisms Transmissions and Automation in Design, vol. 111:34-39, Mar. 1995.

[HATAKEYA95] Hatakeyama M., et. al, "Fast atom beam (FAB) processing with separated masks", IEICE Trans. on Electronics, vol 78C(2):174-179, Feb 1995.

[HAYASHI92] Hayashi I., Iwatsuki N., Fujimoto K., "Output characteristic of a piezoelectric cycloid motor driven near resonance", IFToMM Int. Symp on Theory of Machines and Mechanisms, p 801-803, Sep. 1992, Nagoya.

[HAYWARD93] Hayward V., "Design of a hydraulic robot shoulder based on a combinatorial mechanism", 3rd Int. Symp. on Experimental Robotics, p 297-309, 1993, Koyoto.

[HIGUCHI90] Higuchi T., Yamagata Y., Furutani K., Kudoh K., "Precise positioning mechanism utilizing rapid deformations of piezoelectric elements", IEEE Micro Electro Mechanical Systems, p 222-226, Feb. 1990, Napa Valley.

[HIGUCHI92] Higuchi T., Yamagata Y., "Micro robot arm utilizing rapid deformations of piezoelectric elements", Advanced Robotics, vol. 6(3):353-360, 1992

[HIGUCHI93] Higuchi T., Furutani K., Yamagata Y., Kudoh K., Ogawa M., "Improvement of velocity of impact drive mechanism by controlling friction", Journal of Advanced Autom. Techn., vol 5(2):71-76, 1993.

[HILLER95] Hiller M., "Kinematic und Dynamik für Mechanismen, Fahrzeuge und Roboter", Lecture notes, 1995, ETH Zürich, Switzerland.

[HOWALD92]   Howald L., Rudin H., Güntherodt H.-J., "Piezoelectric inertial stepping motor with spherical rotor", Rev. Sci. Instrum., vol 63 (8), Aug. 1992.

[HUNT83]   Hunt K.H., "Structural kinematics of in-parallel-actuated robot-arms", Trans. ASME Journal of Mechanisms, Transmissions and Automation in Design, vol 105:705-712, Dec. 1983.

[HUNTER90]   Hunter I., Lafontaine S. et al., "Manipulation and dynamic mechanical testing of microscopic objects using a tele-microrobot system", IEEE Control Systems Magazine, p 102, Feb. 1990.

[ISRAELACH95] Israelachvili N.J., Landman U., "Nanotribology: friction, wear and lubrication", Nature, vol 364:607-616, April 1995.

[JACOBSEN89]   Jacobsen S.C., Price R.H., et.al., "The wobble motor: Design, fabrication and testing of an eccentric-motion electrostatic microactuator", IEEE Conf. Robotics & Automation, vol 3:1536-1546, 1989.

[JOHANNSON93] Johannson S., "Hybrid techniques in microrobotics", 1st IARP Workshop on Micro Robotics and Systems, June 1993, Karlsruhe

[KOTA94]   Kota S., Ananthasuresh G.K., Crary S.B., Wise K.D., "Design and fabrication of micro-electromechanical systems", ASME J. of Mechanical Design, vol 116:1081-1088, Dec. 1994.

[KOYANO95]   Koyano K., Sato T., Miyazaki H., "Construction of manipulation system with concentrated visual fields for ultra micro object handling", Proc. of 72nd Annual Spring Meeting, p 281-284, 1995.

[LEE89]   Lee K.M., Arjunan S., "A three degree of freedom micromotion in-parallel actuated micromanipulator", IEEE Conf. on Robotics & Automation 89, vol 3:1698-1703, April 1989, Sacramento, CA, USA.

[MERLET93]   Merlet J.-P., "Parallel Manipulators: state of the art and perspectives", Trans. IMACS/SICE Int. Symp. on Robotics, Mechatronics and Manufacturing Systems, p 21-27, Sept. 1992, Amsterdam, Netherlands,.

[MIKROTURN95] Mikroturn, "Ultraprecision turning machines", Produkt overview, Hembrug, Harlem-Holland, 1995.

[MIYAZAKI95] Miyazaki H., "Fabrication of three-dimensional micro structures by heaping up fine particles", Proc. of 72nd Annual Spring Meeting, p 273-276, 1995.

[MIZUMOTO95] Mizumoto H., Yabuya M., Shimizu T., Kami Y., "An angstrom-positioning system using a twist-roller friction drive", Precision Engineering, vol. 17:57-62, 1995.

[MOESNER95] Mösner F.M., Higuchi T., "Devices for particle handling by an AC electric field", Proc. IEEE Micro Electro Mechanical systems, p 66-71, Jan. 29-Feb. 2, 1995, Amsterdam, Netherlands.

[MORISHITA93] Morishita H., Hatamura Y., "Development of ultra precise manipulator system for future nanotechnology", 1st IARP Workshop on Micro Robotics and Systems, p 34-42, June 1993, Karlsruhe, Germany.

[NAKAO95] Nakao M., Kanayama S., Hatamura Y., "Structure and working characteristic of concentrated motion manipulator in nano-manufacturing world", Proc. of 72nd Annual Spring Meeting, p 277-280, 1995.

[NEUKOMM95] Neukomm P.A., "Sensor und Aktorsysteme", Lecture notes, 1993, ETH Zürich, Switzerland.

[NEWPORT95] Scientific & Laboratory Products, "The Newport Catalogue 94/95", 1994, Newport Corp., Irvine, CA, USA.

[OIWA93] Oiwa T., Kyusojin A., "Development of precise cylinders by ball centers: effect of ball wear", Precision Engineering, vol 15(2): 106-111, Apr. 1993.

[PAN67] Pan C.H.T., Broussard P.H., "Squeeze-film lubrication", Proc. Gas Bearing symp. on Design Methods and Applications, p 12/1-12/35, April 1967, Southampton, UK.

[PAPPAS96] Pappas I., Codourey A., "Visual control of a microrobot operating under a microscope", IROS 96, IEEE/RSJ Int. Conf. on Intelligent Robots and Systems, Nov. 1996, Osaka, Japan.

[PAPPAS97]   Pappas I., Krähenbühl B., "Adaptive visual control of a micro-robot", SGA Bulletin No. 17, May. 1997, ETH Zürich, Switzerland.

[PERNETTE96]   Pernette E., Clavel R., "Parallel robots and microrobotics", ISRAM int. Symp. on Robotics and Manufacturing, Mai 1996, Montpellier.

[POHL87]   Pohl D.W., "Dynamic piezoelectric translation device", Rev. Sci. Instr. 58:54, 1987.

[RENNER90]   Renner Ch., Niedermann Ph., et.al., "A vertical piezoelectric inertial sliding device", Rev. Sci. Instrum., vol 61 (3), March 1990.

[RODRIGUEZ96]   Rodriguez M., Pappas I., Codourey A., "Semi autonomous tele-manipulation in the microworld", SPIE Int. Symp. on Intell. Systems and Adv. Manufact., Microrobotics, Nov. 18-22, Boston, 1996.

[RONG94]   Rong Y., Zhu Y., Luo Z., Liu X., "Design and analysis of flexure-hinge mechanism used in micro-positioning stages", ASME Manufacturing Science and Engineering, vol 68(2):979-986, 1994.

[SCHWEITZER94] Schweitzer G., Bleuler H., Traxler A., "Active magnetic bearings", ETH Zürich, vdf, 1994.

[SCIRE78]   Scire F.E., Teague E.C., "Piezodriven 50-mm range stage with sub-nanometer resolution", Rev. Sci. Instrum., vol 49 (12), Dec 1978.

[SAKMANN95]   Sakmann B., Neher E, "Single-Channel Recording", 2nd edition, Plenum Press, New York-London, 1995.

[SATO93]   Sato T., Koyano k., Nakao M., Hatamura Y., "Novel manipulator for micro object handling as interface between micro and human worlds", IEEE/RSJ Int. Conf. on Intelligent Robots and Systems '93, p 1674-1681, July 1993, Yokohama, Japan.

[SATO94]   Sato T., Ichikawa J., Mitsuishi M., Hatamura Y., "A new micro-teleoperation system employing a hand-held force feedback pencil", IEEE Robotics and Automation '94, p 1728-1733, May 1994.

[SHARON84]   Sharon A., Hardt D., "Enhancement of Robot accuracy using endpoint feedback and a macro-micro manipulator system", Amer. Control Conf. Proc., p 1836-1842, June 1984, San Diego, USA.

[SHINJI95]   Shinji A., Shinji K., et al., "Tube type micro manipulator using shape memory alloy", Proc. of the 6th Int. Symp. on Micro Machine and Human Science, p 115-120, 1995, Nagoya, Japan.

[SLOCUM92]   Slocum A.H., "Precision machine design: Macromachine design philosophy and its applicability to the design of micromachines", IEEE Micro Mechanical Systems, p 37-42, Feb. 1992, Travemünde.

[SMITH92]   Smith T.S., Chetwynd D.G., "Foundations of Ultraprecision Mechanisms Design", Gordon and Breach Science Publishers, Montreux, 1992.

[STEWART65]   Stewart D.," A platform with six degrees of freedom", Proc. of the Inst. of Mech. Engineering, vol 180(5): 371-378, 1965.

[SULZMANN95]   Sulzmann A., Breguet J.M., Jacot, "Microvision system (MVS): A 3D computer graphic-based microrobot telemanipulation and position feedback by vision", SPIE Conf. on Microrobots and Micromechanical Systems., p 38-49, Oct. 1995, Philadelphia, USA.

[THORNLEY92]   Thornley J.K., King T.G., Preston M.E., "A piezoelectrically-controlled rotary micropositioner for applications in surface finish metrology", IFToMM Int. Symp. on Theory of Machines and Mechanisms, p 792-795, Sep. 1992, Nagoya.

[TRUMPER94]   Trumper D.L., Holmes M., et al., "Magnetic/fluid-bearings stage for atomic-scale motion control", 4th Int. Symp. on Magnetic Bearings, p 151-155, Aug. 1994, Zürich.

[VOEGELI97]   Vögeli B., von Känel H., "The Influence of Surface Topography on Adhesion and its Application to Micro Parts Handling", accepted for publication in ECASIA, 1997, Goteborg, Sweden.

[YAMAGATA90]   Yamagata Y., Higuchi T., "Ultra vacuum precise positioning device utilizing rapid deformations of piezoelectric elements", Journal of Vacuum Science & Techn., vol 8(6):4098-4100, Nov. 1990.

[YAMAGATA94]   Yamagata Y., Higuchi T., et.al., "A micro mobile mechanism using thermal expansion and its theoretical analysis", IEEE Micro Electro Mechanical Systems, p 142-147, Jan. 1994, Oiso

[YAMAGATA95]   Yamagata Y., Mihara S., Higuchi T., "Micro parts fabrication by ultra precise cutting technique", Proc. of 72nd Annual Spring Meeting, p242-253, 1995.

[YANG94]   Yang Y.-N., Chieng W.-H., Lee C.-A., "Design for manufacturing the elastic pivots with special reference to manufacturing error", Int. J. of Machine Tools and Manufacture, vol. 34(8):1103-1118, 1994.

[ZESCH95]   Zesch W., Büchi R., Siegwart R., "Inertial mechanisms for positioning microobjects: Two novel mechanisms", SPIE Conf. on Microrobots and Micromechanical Systems, p 80-88, Oct. 1995, Philadelphia, USA.

[ZESCH97]   Zesch W., Brunner M., Weber A., "Vacuum tool for handling microobjects with a nanorobot", IEEE Int. Conf. on Robotics & Automation, April 1997, Albuquerque, NM, USA.

Internal reports and Student Projects

[ANQUETIL97]   Anquetil P., "Elastische Struktur zur Mikropositionierung", Student Project, Inst. of Robotics, ETH Zürich, Feb. 1997.

[KELLER96]   Keller M., "Armmechanismus für den Nanoroboter", Student Project, Inst. of Robotics, ETH Zürich, Feb. 1996.

[ROMI97]   Romi M., "Strukturmechanische Analyse eines Mikropositioniermechanismus", Student Project, Inst. of Robotics, ETH Zürich, Feb. 1997.

[SHIMIZU97]   Shimizu Y., Tsuchiya K, "Micropositioning using inchworm principle", Student Project, Inst. of Robotics, ETH Zürich, Jan. 1997.

[ZESCH93]   Zesch W., Varadi P., "Design und Bau eines Nanoroboterantriebes", Studentproject, 1993, Inst. of Robotics, ETH Zürich, Switzerland.

Appendix

A Model of the Friction

A central issue in high resolution positioning is friction, more specifically, static friction or *stiction*. In contrast to the atomic scale [ISRAELACH95], at macroscopic contacts, the friction is almost independent of the size of the contact surface and approximately proportional to the normal force F_N (perpendicular to the surface). As illustrated in fig. A.1, the friction-velocity characteristic basically consists of four regions.
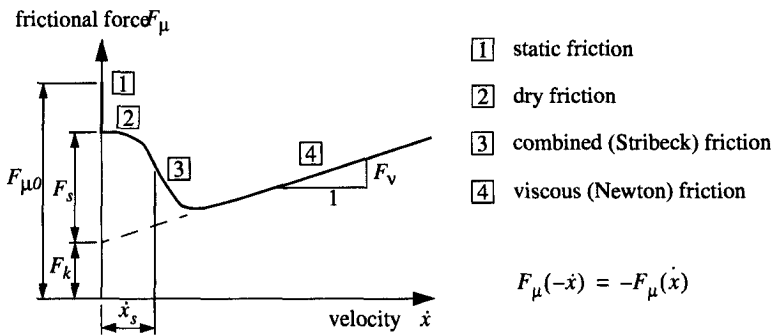

frictional force F_μ

velocity $\dot{x}$

[1] static friction
[2] dry friction
[3] combined (Stribeck) friction
[4] viscous (Newton) friction

$$F_\mu(-\dot{x}) = -F_\mu(\dot{x})$$

Fig. A.1: *Different regimes of friction* [ARMSTRONG91]

It can be approximated as:

$$F_\mu = \text{sgn}(\dot{x}) \cdot (F_K + F_S \cdot e^{-|\dot{x}/\dot{x}_S|}) + F_v \cdot \dot{x} \quad \Leftarrow \quad \dot{x} \neq 0$$
$$|F_\mu| \leq F_{\mu 0} \qquad\qquad\qquad\qquad\qquad\quad \Leftarrow \quad \dot{x} = 0$$

(A.1)

with $\dot{x}_S$ the limit velocity between dry and viscous friction.

Lubricated bearings normally work in the viscous domain (4) or – during the start-up phase and at reduced speed – in the Stribeck section (3). Conversely, in micropositioning systems, the velocities are very small and/or there is hardly any lubricant involved. Therefore, precision displacements normally take place in the static (1) and dry (2) friction regime. $F_{\mu 0}$, F_k and F_S are approximately proportional to the normal force F_N [ARMSTRONG91]. Thus, for small velocities, eq. A.1 can be simplified to the well known *Coulomb* relation. It is basically divided into two sections, i.e., static friction ($\dot{x} = 0$) and kinetic friction ($\dot{x} \neq 0$) as expressed in eq. A.2.
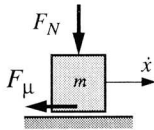
$$F_\mu = F_{\mu k} = \text{sgn}(\dot{x}) \cdot F_N \cdot \mu_k \big|_{\dot{x} \neq 0}$$
$$|F_\mu| = k_\mu \cdot \Delta x \leq F_{\mu 0} = F_N \cdot \mu_0 \big|_{\dot{x} = 0}$$

(A.2)

Herein, μ_0 denotes the static and μ_k the kinetic coefficient of friction. At zero velocity the frictional contact behaves as a spring with an elasticity k_μ originating from local material deformation Δx.

Together with a compliant drive train friction causes the stick-slip effect. This phenomenon is characterized by a chaotic switching between static and kinetic friction at low velocities. It is responsible for the limitation in resolution and accuracy in many technical instruments and can even lead to control instabilities [ARMSTRONG91].

B   Piezoelectric Actuation

B.1   Piezoelectricity

The piezoelectric effect provides a direct method of converting mechanical energy into electrical energy or vice versa. It occurs in special anisotropic, polarized ceramics and certain polymers (cf. table B.1). The effect is reversible and is therefore suited for both sensors and actuators.
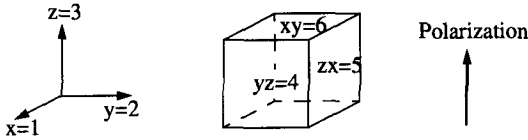

Fig. B.1: *Definition of indices of a polarized ceramic crystal*

In order to model the mechanical-electrical characteristics of a piezoelectric material a standard indexing for the translational (1...3) and the shear (4...6) directions is used, as shown in fig. B.1. The actuator can roughly be modeled as a linear transformer between an applied electric field E_i and the deformation S_j:

$$S_j = d_{ji} \cdot E_i. \qquad (B.1)$$

Notice that in practice, effects such as hysteresis, creep and ageing cause deviations from the ideal linear behavior (cf. eq. B.3) of up to 10%.
Further, the piezo can be treated as an elastic spring. For a constant electric field the relationship between deformation S_j and mechanical stress T_i is given by

$$S_j = s_{ji} \cdot T_j. \qquad (B.2)$$

Typical values of charge constants d_{ji} and elastic constants s_{ji} for some typical piezoelectric materials are shown in table B.1. For discrete actuators of length l the relation between the voltage V_i acting along the direction i and the displacement Δl_j parallel to the direction j is given by

$$\frac{\Delta l_j}{V_i} = \frac{l \cdot S_j}{l \cdot E_i} = \frac{S_j}{E_i} = d_{ji}, \tag{B.3}$$

which is independent of the length l. If it is clear from the context, we abbreviate d_{ji} by d. The piezo constant d can be increased with a stack design, i.e., the active material is divided into n layers of a thickness of $\lambda = l/n$. The single slices are operated electrically in parallel but mechanically in series [BAUER94]. The result is a piezo constant d_{stack} increased by a factor of n compared to d of the bulk design.

The characteristics of some commonly used piezo-electric materials are outlined in table B.1. Both PXE52 and PXE71 are sintered lead-zirconate-titanate ceramics generating longitudinal/transversal and shear displacements, respectively, whereas PVDF is a representative of the less effective piezoelectric polymers.

mode	parameter	unit	ceramics		polymer
			PXE52	PXE71	PVDF
longitudinal	d_{33}	10^{-12} m/V	580	~0	17.5
transversal	d_{31}	10^{-12} m/V	-270	-147	6.5
shear	d_{15}	10^{-12} m/V	0	500	~0
longitudinal	s_{33}	10^{-12} m^2/N	16.0	15.0	400
transversal	s_{31}	10^{-12} m^2/N	20.0	~0	400
shear	s_{15}	10^{-12} m^2/N	~0	38.0	~0

Tab. B.1: Charge constants d_{ji} and elastic constants s_{ji} for different materials. The shaded boxes indicate the corresponding mode of operation.

B.2   Dynamical Model of the Piezoelectric Actuator

The dynamical behavior of a piezoelectric actuator can be modeled with a mass-spring system and an articulated joint controlled by a voltage V, as shown in fig. B.2. Notice that we do not model the characteristic of the electrical circuit,

which is coupled the mechanic system. This is permissible if we assume a voltage supply with a low output resistance, e.g., a power amplifier.
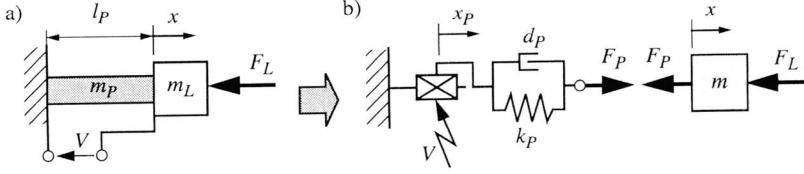

Fig. B.2: (a) Piezo-electric actuator loaded with a mass m_L and a load force F_L,(b) its mathematical model.

To obtain a discrete model, we virtually distribute the piezo mass m_P to its ends. This yields a mass m in the modell according to

$$m = m_L + \frac{m_P}{2} \tag{B.4}$$

The actuator can be considered as a serial arrangement of an ideal actuator with a displacement (cf. eq. B.3)

$$x_P = d \cdot V \tag{B.5}$$

and a spring-damper system which can be modeled by

$$F_P = k_P \cdot x_{el} + d_P \cdot \dot{x}_{el}. \tag{B.6}$$

Herein, F_P is the force in the actuator, k_P and d_P its stiffness and coefficient of damping, respectively, and $x_{el} = x - x_P$ the elastic deformation.

Inserting eq. B.5 and eq. B.6 into the equation of motion $m\ddot{x} = -F_L - F_P$, we can finally write the dynamic equation for the position of the mass x:

$$m \cdot \ddot{x} + d_P \cdot \dot{x} + k_P \cdot x = -F_L + d(k_P \cdot V + d_P \cdot \dot{V}). \tag{B.7}$$

This model has been used to derive the equations for the stepping drives discussed in chapter 3.

C FEM Model of Abalone

This section presents an FEM model of Abalone [ROMI97] implemented in ANSYS© [ANSYS95]. Its shape and data are shown in fig. C.1 and table C.1, respectively. The numerical results obtained in both static and dynamic analysis are verified with measurements using speckle interferometry (SpI) and scanning laser interferometry (SLI).

element type	SOLID95 (Quad, 20 nodes)
number of elements nodes DOFs	4044 23903 71709
wave front	3167

Tab. C.1: *Model type & size*
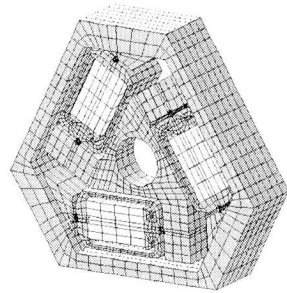
Fig. C.1: *3D-modell of Abalone*

C.1 Static Analysis

The static analysis aimed at investigating Abalone's local kinematics, its stiffness and the stress distribution.

Kinematics

Fig. C.2 shows a comparison of FEM and SpI-measurement for a voltage of 100 V at all three piezo actuators, i.e., pure rotation of Abalone. In both pictures Abalone's inner platform stays at its position. On the outer platform we observe parallel, equally distributed stripes, which indicate a z-rotation without any deformation of the frame. In agreement with the mechanical model, the maximum displacement (bottom of the picture) results in about 10 μm. In the resulting images one stripe indicates a displacement difference of $s_x = 2.207 / 1.003$ μm in x-direction.
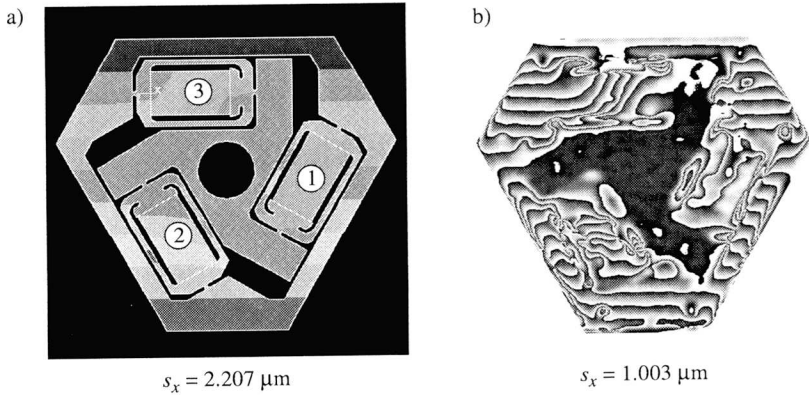
$s_x = 2.207\ \mu m$ $s_x = 1.003\ \mu m$

Fig. C.2: *Rotation about the z-axis (bottom view), x-displacements calculated with FEM (a) and measured with SpI (b).*

As with the rotational case, experiments with translational displacements showed that almost all deformation takes place in the three actuation structures and the elastic pivots. This justifies our static model which relies on two rigid frames.

Fig. C.3 presents a close up view of such a region. Notice the large strain, i.e., the high line density, in the vertical section of the preloading structure.

stack piezo
elastic pivot
electrical wire

$s_x = 1.07\ \mu m$ $s_x = 0.585\ \mu m$
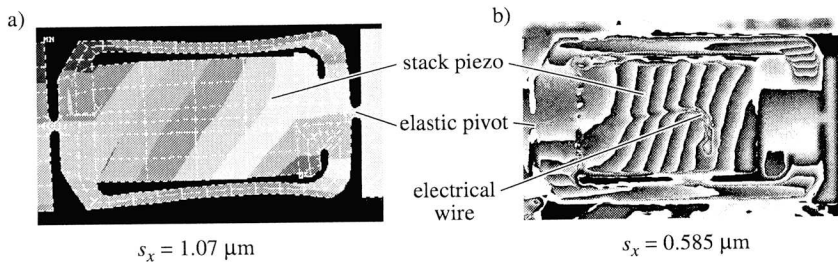
Fig. C.3: *Deformation (x-displacement) of the preloaded actuator during pure rotation, (a) FEM, displacement scaling 75 × , (b) SpI.*

Stress analysis

In fig. C.4, the (von Mises) stress is drawn for the piezo's maximum elongation (~ 5 μm at $V = 100$ V). As expected, the maximum stress occurs at the inside of the of the preloading beam's junction into the bulk structure. Compared to the titanium's static and dynamic strength, of 890 and 560 N/mm^2, respectively, this value is uncritical and therefore, should not cause problems of fatigue.
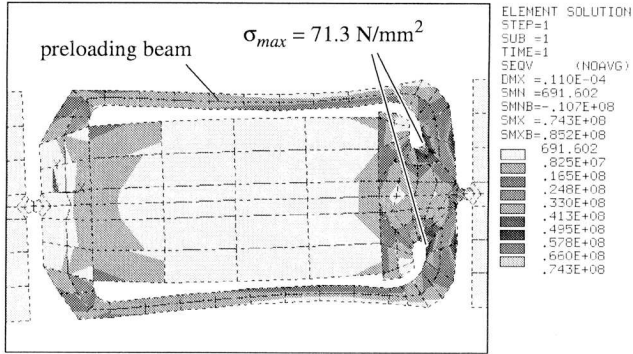

Fig. C.4: *Von-Mises stress in the preloaded actuator at* $\Delta q = 5$ *μm*

C.2 Dynamic Analysis

Due to their physical principle, inertial drives cause vibrations. With the following dynamic analysis we evaluated Abalone's principal vibration modes and the corresponding frequencies, exhibited in fig. C.5.

It is important to see, that the first three eigen modes (fig. C.5, 1-3) are out-of-plane vibrations. In these modes, both platforms remain more or less undeformed, as with the static case. Thus, a simplified mechanical model, i.e., a two-mass system consisting of two rigid frames connected by three 3D-springs (actuators) could be used to investigate Abalone's low frequency behavior. Subsequent to these rigid frame modes, Abalone is subject to planar bending vibrations of the outer platform (fig. C.5, 4 & 5).

A comparison with LI measurements (cf. fig. 4.16) yielded a maximum frequency deviation between simulation and reality of less than 13%. The deformation shape itself was explored by SLI. As an example for the good qualitative

agreement, fig. C.6 shows the analysis of 4th mode at $f = 2980$ Hz (3104 Hz in simulation).

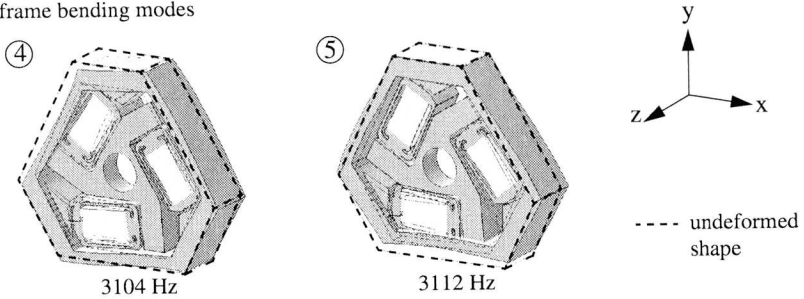"rigid-frame" modes
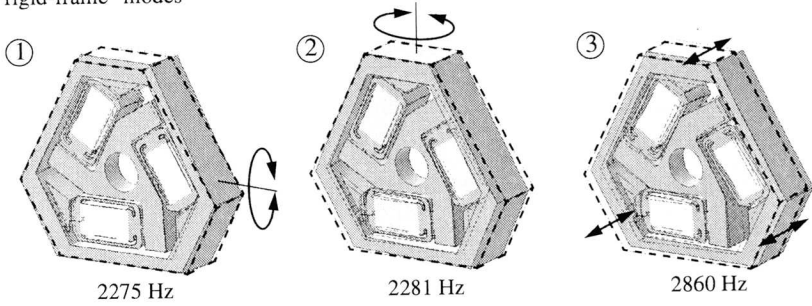
frame bending modes
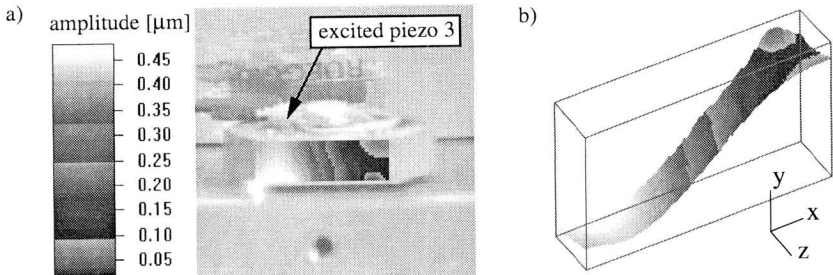
Fig. C.5: *Abalone's five principal vibration modes*

Fig. C.6: *SLI measurement of Abalone's 4th mode (2980 Hz), a) contour image, b) 3D amplitude plot*

Curriculum Vitae

Born on November 3rd, 1968 in Hard, I grew up in Fussach, Austria. I finished the Höhere Technische Lehranstalt in Bregenz in 1988 as an Electrical Engineer. After one year of military service, I entered the Swiss Federal Institute of Technology in Zürich (ETHZ). During my studies I worked as a teaching assistant for courses in mechanics as well as design and construction methodology. In January 1994 I graduated with a diploma in Mechanical Engineering in "Forming of Superconductor Wires". In April of the same year I registered as a PhD student under supervision of Professor G. Schweitzer at the Institute of Robotics. Since then I have been working as a research assistant, involved in industrial projects (Minast 6.0), whilst pursuing my research objectives. During this time, I have supervised several student projects in the field of micro- and nanorobotics. I was also responsible for tutorials in robotics as well as in computer-aided kinematics of multi body systems.
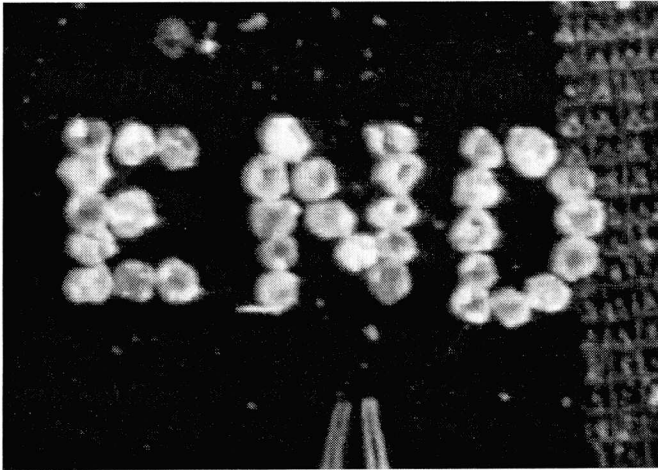
Fig. E.1: *Diamond crystals precisely arranged with the nanorobot indicating the END of this thesis.*